

# COMPUTATIONAL STUDIES OF ATOMIC, IONIC, AND MOLECULAR SCATTERING

by

JEFF NOLTE

(Under the direction of Phillip C. Stancil)

## ABSTRACT

Collisions between atoms, ions, and molecules play a fundamental role in a number of astrophysical contexts. In this work, we perform quantum mechanical close-coupling scattering calculations for a variety of collision systems and discuss their implications for our understanding of various astrophysical processes.

We begin with a study of rovibrational de-excitation of HD in collisions with He. Along with H<sub>2</sub>, HD has been found to play an important role in the cooling of the primordial gas in the formation of the first stars and galaxies, and the rate of this cooling requires a knowledge of collision rate coefficients with common neutrals such as H and He. In this study we perform cross section calculations for the He-HD collision system over a range of collision energies and for initial rovibrational states of  $j = 0$  and  $1$  for  $v = 0$  to  $17$ . We report rate coefficients for all  $\Delta v = 0, -1,$  and  $-2$  transitions and compare them to previous calculations.

Next we examine the effect of theoretically varying the collision-system reduced mass in collisions of He with vibrationally excited molecular hydrogen. Complex scattering lengths and vibrational quenching cross sections, and a low-energy scattering resonance are studied as a function of the collision system reduced mass. Experimental observations of these phenomena in the ultracold regimes for collisions of He with H<sub>2</sub>, HD, HT, and DT should be feasible in the near future.

Finally, we perform electron-capture cross section calculations for the collision systems  $O^{7+} + H$  and  $C^{5+} + H$  using the quantum mechanical molecular orbital close-coupling method. Charge exchange between highly-charged solar wind ions and neutral interstellar hydrogen has been found to be a significant contributor to the heliospheric component of the soft x-ray background, as the highly excited resultant ions emit x-rays in the electron's cascade to the ground state. Calculations are performed over a range of collision energies for all important  $n$ -,  $l$ -, and  $S$ -resolved states. We compare our results to new atomic orbital close-coupling, classical trajectory Monte Carlo, and experimental merged-beam results.

INDEX WORDS: Atom-molecule collisions, Atom-ion collisions, Ultracold collisions, Charge exchange, Rovibrational excitation

COMPUTATIONAL STUDIES OF ATOMIC, IONIC, AND MOLECULAR SCATTERING

by

JEFF NOLTE

B.S., The University of Georgia, 2004

A Dissertation Submitted to the Graduate Faculty  
of The University of Georgia in Partial Fulfillment  
of the  
Requirements for the Degree  
DOCTOR OF PHILOSOPHY

ATHENS, GEORGIA

2011

© 2011

Jeff Nolte

All Rights Reserved

COMPUTATIONAL STUDIES OF ATOMIC, IONIC, AND MOLECULAR SCATTERING

by

JEFF NOLTE

Approved:

Major Professor: Phillip C. Stancil

Committee: Chad Fertig  
Robin Shelton

Electronic Version Approved:

Maureen Grasso  
Dean of the Graduate School  
The University of Georgia  
August 2011

## ACKNOWLEDGMENTS

The central chapters of this dissertation comprise papers which have been published or are in preparation for submission to various journals. I would like to thank my many collaborators and coauthors for their support and contributions to the research forming the basis of this dissertation, namely: Robert J. Buenker, Alexander Dalgarno, Ilija N. Draganić, Robert C. Forrey, Charles C. Havener, Yawei Hui, Teck-Ghee Lee, Heinz-Peter Liebermann, Balakrishnan Naduvalath, Milun J. Raković, David R. Schultz, Phillip C. Stancil, Yong Wu, and Benhui Yang. I also wish to acknowledge Mineo Kimura (deceased), Lukaš Pichl, and Ayako Watanabe for their contributions to an early phase of the work presented in Chapter 4.

Most of all I wish to thank my advisor, Phillip C. Stancil, for his tremendous support and encouragement throughout my graduate studies.

This work was partially supported by NASA grant NNX09AV46G and NSF grants AST-0607733 and OISE-0813064. A portion of the calculations reported here were performed at the University of Georgia Research Computing Center, a partnership between the UGA Office of the Vice President for Research and the Office of the Chief Information Officer.

## TABLE OF CONTENTS

	Page
ACKNOWLEDGMENTS . . . . .	iv
LIST OF FIGURES . . . . .	vii
LIST OF TABLES . . . . .	xi
 CHAPTER	
1 INTRODUCTION AND LITERATURE REVIEW . . . . .	1
2 ROVIBRATIONAL QUENCHING OF HD IN COLLISIONS WITH HE . . . . .	5
2.1 INTRODUCTION . . . . .	6
2.2 COMPUTATIONAL DETAILS . . . . .	9
2.3 RESULTS . . . . .	10
2.4 ASTROPHYSICAL IMPLICATIONS . . . . .	17
2.5 CONCLUSIONS . . . . .	19
3 ISOTOPE EFFECTS IN COMPLEX SCATTERING LENGTHS FOR HE COLLISIONS WITH MOLECULAR HYDROGEN . . . . .	21
3.1 INTRODUCTION . . . . .	22
23	
3.3 METHODOLOGY . . . . .	26
3.4 COMPUTATIONAL METHOD . . . . .	27
3.5 RESULTS . . . . .	27
3.6 CONCLUSIONS . . . . .	33

4	FINAL-STATE RESOLVED CHARGE EXCHANGE BETWEEN $O^{7+}$ AND H: APPLI- CATIONS TO X-RAY EMISSION IN THE SOLAR SYSTEM . . . . .	35
4.1	INTRODUCTION . . . . .	36
4.2	MOCC METHOD . . . . .	39
4.3	RESULTS . . . . .	50
4.4	CONCLUSIONS . . . . .	57
5	FINAL-STATE RESOLVED CHARGE EXCHANGE BETWEEN $C^{5+}$ AND H . . . .	61
5.1	INTRODUCTION . . . . .	62
5.2	COMPUTATIONAL DETAILS . . . . .	62
5.3	RESULTS . . . . .	63
5.4	CONCLUSIONS . . . . .	74
6	CONCLUSIONS . . . . .	81
	BIBLIOGRAPHY . . . . .	84
	APPENDIX	
A	$n, l$ -RESOLVED CROSS SECTIONS FOR $O^{7+}+H$ . . . . .	94
B	$n, l$ -RESOLVED CROSS SECTIONS FOR $C^{5+}+H$ . . . . .	104

## LIST OF FIGURES

2.1	He-HD inelastic cross sections for $\{v, j = 1\} \rightarrow \{v' = v, j' = 0\}$ . . . . .	11
2.2	He-HD inelastic rate coefficients for $\{v, j = 1\} \rightarrow \{v' = v, j' = 0\}$ . . . . .	12
2.3	He-HD inelastic rate coefficients for (a) $\{v, j = 0\} \rightarrow \{v - 1, j' = 8\}$ and (b) $\{v, j = 0\} \rightarrow \{v - 1, j' = 0\}$ . . . . .	13
2.4	Comparison of He-HD inelastic rate coefficients for $\{v = 1, j = 1\} \rightarrow \{v' = 0, j'\}$ : current results, solid lines; Roueff & Zeippen [4], dotted lines. . . . .	15
2.5	Comparison of He-HD inelastic rate coefficients for $\{v = 3, j = 1\} \rightarrow \{v' = 2, j'\}$ : current results, solid lines; Roueff & Zeippen [4], dotted lines. . . . .	16
2.6	Comparison of interaction potential matrix elements $y_\lambda(vj, v'j' R)$ ( $10^{-4}$ a.u.) as given by Equation 2.3 using numerical rovibrational wavefunctions and harmonic oscillator (HO) wavefunctions. All HO results are given by thin solid black lines. (a) Diagonal elements for $v, j = 3, 1$ . (b) Same as (a), but for $v, j = 10, 0$ . (c) and (d) off-diagonal elements for $\lambda = 1$ and $\lambda = 5$ , respectively, compared to isotropic diagonal elements. All matrix elements are taken as positive values for plotting convenience. . . . .	20
3.1	Real part $\alpha_{10}$ of the scattering length for $^3\text{He}$ and $^4\text{He}$ collisions with HX, DX and TX as a function of the ratio of the reduced masses of the hydrogen isotopomer and $\text{H}_2$ . Inset, $\alpha_{10}$ for a variation of the He mass for He-HD collisions. 28	28
3.2	Same as in Figure 3.1, but for the imaginary part $\beta_{10}$ of the scattering length. 29	29
3.3	Ratio of $\beta_{10}/\alpha_{10}^2$ as a function of reduced mass ratio for $^{3,4}\text{He}$ -HX. . . . .	30
3.4	State-to-state quenching cross sections for $^3\text{He}$ -DX( $v = 1, j = 0$ ) $\rightarrow$ $^3\text{He}$ -DX( $v = 0, j'$ ) as a function of the DX/ $\text{H}_2$ reduced-mass ratio. . . . .	31
3.5	Rovibrational energy levels for first three values of $v$ for He- $\text{H}_2$ . . . . .	32

3.6	Low-energy elastic cross sections for $^4\text{He}$ collisions with molecular hydrogen isotopomers with $v = 1, j = 0$ . (a) Total cross sections for $\text{H}_2$ , HD, HT, and DT. (b) Partial cross sections for the dominant partial waves for $^4\text{He}$ -DT. . . . .	34
4.1	Singlet adiabatic potentials for $\text{O}^{7+} + \text{H}$ . . . . .	40
4.2	Singlet adiabatic potentials for $\text{O}^{7+} + \text{H}$ (detail; $^1\Sigma^+$ states only). . . . .	42
4.3	Triplet adiabatic potentials for $\text{O}^{7+} + \text{H}$ . . . . .	43
4.4	Triplet adiabatic potentials for $\text{O}^{7+} + \text{H}$ (detail; $^3\Sigma^+$ states only). . . . .	44
4.5	Family of $(5\ ^3\Sigma^+ - N\ ^3\Sigma^+)$ nonadiabatic radial couplings for $\text{O}^{7+} + \text{H}$ . . . . .	45
4.6	Family of $(N\ ^3\Sigma^+ - 1\ ^3\Pi)$ nonadiabatic rotational couplings for $\text{O}^{7+} + \text{H}$ . . . . .	46
4.7	Nonadiabatic radial couplings with avoided crossings for adjacent $n = 5$ singlet channels for $\text{O}^{7+} + \text{H}$ . . . . .	47
4.8	Nonadiabatic radial couplings with avoided crossings for adjacent $n = 5$ triplet channels for $\text{O}^{7+} + \text{H}$ . . . . .	48
4.9	Total $n, l$ -resolved MOCC cross sections for $\text{O}^{7+} + \text{H}$ . . . . .	51
4.10	Singlet $n, l$ -resolved MOCC cross sections for $\text{O}^{7+} + \text{H}$ . . . . .	52
4.11	Triplet $n, l$ -resolved MOCC cross sections for $\text{O}^{7+} + \text{H}$ . . . . .	53
4.12	Triplet-singlet ratios for $n, l$ -resolved cross sections for $\text{O}^{7+} + \text{H}$ . . . . .	54
4.13	Comparison of total cross sections for $\text{O}^{7+} + \text{H}$ using MOCC, as well as AOCC and CTMC [123] methods. Also included are fits by Janev et al. (1995) [124] and Phaneuf et al. (1987) [125], as well as experimental results of Havener et al. (2011) [22], Meyer et al. (1985) [23], and Panov et al. (1983)[24]. . . . .	55
4.14	Comparison of $n$ -resolved cross sections for $\text{O}^{7+} + \text{H}$ for MOCC, AOCC, CTMC calculations and experimental results of Kearns et al. (2003) [25]. . . . .	56
4.15	Comparison of $n = 5$ $l$ -distributions for $\text{O}^{7+} + \text{H}$ for MOCC, AOCC and CTMC, along with statistical and low-energy distributions at $E = 300$ eV/u. . . . .	58
4.16	Comparison of $n = 5$ $l$ -distributions for $\text{O}^{7+} + \text{H}$ for MOCC, AOCC and CTMC, along with statistical and low-energy distributions at $E = 1000$ eV/u. . . . .	59

4.17	Comparison of MOCC $n = 5$ $l$ -distributions for $O^{7+}+H$ to low-energy distribution at different energies. . . . .	60
5.1	Singlet adiabatic potentials for $C^{5+}+H$ . . . . .	65
5.2	Singlet adiabatic potentials for $C^{5+}+H$ (detail; $^1\Sigma^+$ states only). . . . .	66
5.3	Triplet adiabatic potentials for $C^{5+}+H$ . . . . .	67
5.4	Triplet adiabatic potentials for $C^{5+}+H$ (detail; $^3\Sigma^+$ states only). . . . .	68
5.5	Family of $(4 \ ^1\Sigma^+ - N \ ^1\Sigma^+)$ nonadiabatic radial couplings for $C^{5+}+H$ . . . . .	69
5.6	Family of $(N \ ^1\Sigma^+ - 1 \ ^1\Pi)$ nonadiabatic rotational couplings for $C^{5+}+H$ . . . . .	70
5.7	Nonadiabatic radial couplings with avoided crossings for adjacent $n = 4$ singlet channels for $C^{5+}+H$ . . . . .	71
5.8	Nonadiabatic radial couplings with avoided crossings for adjacent $n = 4$ triplet channels for $C^{5+}+H$ . . . . .	72
5.9	Total $n, l$ -resolved MOCC cross sections for $C^{5+}+H$ . . . . .	73
5.10	Singlet $n, l$ -resolved MOCC cross sections for $C^{5+}+H$ . . . . .	74
5.11	Triplet $n, l$ -resolved MOCC cross sections for $C^{5+}+H$ . . . . .	75
5.12	Triplet-singlet ratios for $n, l$ -resolved cross sections for $C^{5+}+H$ . . . . .	76
5.13	Comparison of total cross sections for $C^{5+}+H$ using MOCC, as well as AOCC and CTMC [123] methods. Also included are previous MOCC results by Bottcher and Heil (1982) [131], a fit by Suno and Kato (2005) based on previous theoretical and experimental results [132], and experimental results of Draganić et al. (2011) [27], Panov et al. (1983) [24], Phaneuf et al. (1982) [28], Crandall et al. (1979) [29], and Goffe et al. (1979) [30]. . . . .	77
5.14	Comparison of $n$ -resolved cross sections for $C^{5+}+H$ for MOCC, AOCC, CTMC calculations and experimental results of Kearns et al. [25]. (Error bars estimated from their $O^{7+}+H$ data). . . . .	78
5.15	Comparison of $n = 4$ $l$ -distributions $C^{5+}+H$ for MOCC, AOCC and CTMC, along with statistical and low-energy distributions at $E = 300$ eV/u. . . . .	79

5.16	Comparison of $n = 5$ $l$ -distributions for $C^{5+}+H$ for MOCC, AOCC and CTMC, along with statistical and low-energy distributions at $E = 1000$ eV/u.	80
6.1	Combined spectra of $O^{7+}+H$ , $O^{8+}+H$ , $O^{7+}+He$ .	82
A.1	Cross sections for capture into $4s$ for $O^{7+}+H$ ; MOCC, AOCC, CTMC results.	95
A.2	Cross sections for capture into $4p$ for $O^{7+}+H$ ; MOCC, AOCC, CTMC results.	96
A.3	Cross sections for capture into $4d$ for $O^{7+}+H$ ; MOCC, AOCC, CTMC results.	97
A.4	Cross sections for capture into $4f$ for $O^{7+}+H$ ; MOCC, AOCC, CTMC results.	98
A.5	Cross sections for capture into $5s$ for $O^{7+}+H$ ; MOCC, AOCC, CTMC results.	99
A.6	Cross sections for capture into $5p$ for $O^{7+}+H$ ; MOCC, AOCC, CTMC results.	100
A.7	Cross sections for capture into $5d$ for $O^{7+}+H$ ; MOCC, AOCC, CTMC results.	101
A.8	Cross sections for capture into $5f$ for $O^{7+}+H$ ; MOCC, AOCC, CTMC results.	102
A.9	Cross sections for capture into $5g$ for $O^{7+}+H$ ; MOCC, AOCC, CTMC results.	103
B.1	Cross sections for capture into $3s$ for $C^{5+}+H$ ; MOCC, AOCC, CTMC results.	105
B.2	Cross sections for capture into $3p$ for $C^{5+}+H$ ; MOCC, AOCC, CTMC results.	106
B.3	Cross sections for capture into $3d$ for $C^{5+}+H$ ; MOCC, AOCC, CTMC results.	107
B.4	Cross sections for capture into $4s$ for $C^{5+}+H$ ; MOCC, AOCC, CTMC results.	108
B.5	Cross sections for capture into $4p$ for $C^{5+}+H$ ; MOCC, AOCC, CTMC results.	109
B.6	Cross sections for capture into $4d$ for $C^{5+}+H$ ; MOCC, AOCC, CTMC results.	110
B.7	Cross sections for capture into $4f$ for $C^{5+}+H$ ; MOCC, AOCC, CTMC results.	111
B.8	Cross sections for capture into $n = 5$ for $C^{5+}+H$ ; MOCC ( $5s$ only), AOCC, CTMC results.	112

## LIST OF TABLES

- 4.1 Comparison of asymptotic separated-atom energies (in a.u., where 1 a.u. = 1 hartree) between MRDCI calculations and experimental NIST data [118] for  $O^{7+} + H$ .  $\Delta E_{calc}$  is the energy separation of the asymptotic atomic state from the initial state  $O^{7+}(1s) + H(1s)$  in the MRDCI calculations.  $\Delta E_{exp}$  is the same quantity for the experimental values.  $\Delta E = |\Delta E_{exp} - \Delta E_{calc}|$ . The value marked \* has been calculated from the  $5\ ^1P_1 - 5\ ^1S_0$  transition wavelength in Johnson et al. [119]. Experimental energies marked N/A are not available. . . . . 41
- 5.1 Comparison of asymptotic separated-atom energies in Hartree atomic units (a.u.) between MRDCI calculations and experimental NIST data [118] for  $C^{5+} + H$ .  $\Delta E_{calc}$  is the energy separation of the asymptotic atomic state from the initial state  $C^{5+}(1s) + H(1s)$  in the MRDCI calculations.  $\Delta E_{exp}$  is the same quantity for the experimental values.  $\Delta E = |\Delta E_{exp} - \Delta E_{calc}|$ . . . . . 64

## CHAPTER 1

### INTRODUCTION AND LITERATURE REVIEW

Inelastic collisions of atoms, ions, and molecules underly a variety of astrophysical process, the accurate modeling of which requires a detailed knowledge of the cross sections and rate coefficients for the relevant collision systems. Such processes which are considered in this work include the radiative cooling of gas clouds during collapse to form the first stars, and the emission of x-rays from planets, comets, and diffuse gas within the Solar System. Given the breadth of relevant collision systems and the often limited range of collision energies and lack of final state resolution in laboratory measurements, the need for theoretical methods as a supplement to experimental data is evident.

Such methods vary in sophistication from semiclassical to fully quantum mechanical, the choice of which is determined by considerations of practicality and applicability. In general, while less taxing on computational resources, semiclassical treatments are valid only for the highest energies. For the most accurate results, particularly at low to intermediate energies, we must turn to fully quantal methods, and it is this approach that we adopt in the present work. In particular, we employ variations of a quantum mechanical close-coupling treatment wherein the wavefunction of the system is expanded in terms of an appropriate set of basis functions. In general, these are functions of the electronic energy and internuclear separation  $R$  of the species in question, and form solutions to the Schrödinger equation for fixed values of  $R$ . This yields a set of coupled differential equations which may be solved numerically to obtain scattering matrix elements and cross sections.

The first system we investigate in Chapter 2 is that of rovibrational de-excitation of HD by He. This collision system is of interest for its role in determining the thermal balance

of collapsing protoclouds to form the first stars. In particular, every instance of excitation through photon absorption followed by collisional rovibrational de-excitation results in a net heating of the gas, while the opposite process results in cooling. Although  $\text{H}_2$  is the dominant and more abundant coolant, many studies (see, e.g., Ref. [1]) suggest that, due to its permanent dipole moment and smaller rotational constant, HD may rival  $\text{H}_2$  in certain circumstances as a coolant of primordial clouds. As far as we know, there have been no experimental studies of this system, although calculations for purely rotational transitions for  $v = 0$  have been performed by Schaefer [2] and Roueff and Zeppen [3], who also did calculations for rovibrational transitions [4], though limited to the first four vibrational states. We extend these calculations to include all bound initial vibrational states ( $v=0 - 17$ ) and improve on existing calculations by adopting a much larger basis set, and using numerically determined wavefunctions for the HD interaction potential matrix elements, as opposed to the harmonic oscillator approximation for the HD vibrational functions employed by Roueff and Zeppen.

A vital ingredient in scattering calculations is the interaction potential, and cross sections are generally sensitive to the details of the potential energy surface employed, particularly at low energies. In Chapter 3, we study the effects of artificially varying the reduced mass of the He- $\text{H}_2$  collision system by varying the mass of one of the hydrogen atoms or the helium atom. It has been shown by Jamieson and Zygelman [5] that this is equivalent to adjusting the interaction potential. This technique allows us to probe the sensitivity of cross sections to small changes in the interaction potential and bound state energy levels at low collision energies. A number of studies have focused on mass effects in collision dynamics, including Kreutz et al. for He-HD [6], Jamieson and Zygelman for H-H [5], and Bodo et al. for  $\text{F} + \text{H}_2$  [7], the last two of which revealed a sensitive dependence of the scattering length to the presence of weakly bound or virtual states. This finding is confirmed in the presence of zero energy resonances corresponding to bound states in the present work. In this chapter we also discuss the complex scattering length, introduced by Balakrishnan et al. [8],

a concept of great utility in describing the elastic and inelastic cross sections and quenching rate coefficients in the ultracold limit.

In Chapter 4 we examine charge exchange between  $O^{7+}$  and H, an important contributor to x-ray emission within the solar system. Over the last two decades, diffuse soft x-ray (0.1 - 1.5 keV) emission has been observed through the Wisconsin [9] and ROSAT [10] all-sky surveys, as well as observations by, for instance, a sounding rocket equipped with microcalorimeters [11], the *Chandra X-ray Observatory* [12], *XMM-Newton* [13], and the Japanese satellite *Suzaku* [14, 15]. It was proposed by Cox [16] that this emission may be due in part to charge exchange between heavy solar wind ions and interstellar neutrals such as H and He which have penetrated the heliosphere, similar to the process originally proposed by Cravens [17, 18] to explain x-ray emission from comets. After electron capture by the highly charged ion into an excited state, the electron de-excites in a radiative cascade to the ground state, emitting at least one x-ray photon in the process. It has since been suggested that as much as 25-50% of the soft x-ray background at 1/4 keV may be heliospheric in origin [19, 20], while Koutroumpa et al. found the local 3/4 keV emission detected in front of shadowing clouds to be almost entirely due to O VII and O VIII emission [21]. Of course, the accurate modeling of this emission requires detailed knowledge of state-specific charge exchange cross sections. To achieve this end, we use a fully quantum mechanical molecular orbital close-coupling (MOCC) treatment to calculate  $n, l, S$ -resolved charge exchange cross sections for the  $O^{7+}+H$  system. This level of resolution is completely lacking in the literature. Experimental studies of the system such as those by Havener et al. [22], Meyer et al. [23], and Panov et al. [24] have generally been limited to total cross sections, while  $n$ -resolved relative cross sections have been obtained by Kearns et al. [25], though these are also restricted to a narrow band of collision energies, 350-875 eV/u. We compare our results with these and theoretical atomic orbital close-coupling (AOCC) and classical trajectory Monte Carlo (CTMC) results, and discuss astrophysical implications.

In Chapter 5 we report  $n, l, S$ -resolved cross sections for a similar charge exchange system,  $C^{5+} + H$ , again using an MOCC treatment.  $l, S$ -resolved cross sections for this system are similarly lacking in the literature, with the exception of a semiclassical MOCC treatment for energies  $> 15$  eV/u and a two-channel fully quantal treatment for lower energies performed by Shimakura et al. [26]. Meanwhile, experimental studies by Draganić et al. [27], Panov et al. [24], Phaneuf et al. [28], Crandall et al. [29], and Goffe et al. [30] have been limited to total cross sections.  $n$ -resolved cross sections appear again only in Kearns et al. [25], though in this case only for an energy of 833 eV/u. We again compare our results to experimental and theoretical AOCC and CTMC results.

We summarize our results and briefly discuss avenues of future research in Chapter 6.

## CHAPTER 2

### ROVIBRATIONAL QUENCHING OF HD IN COLLISIONS WITH HE<sup>1</sup>

---

<sup>1</sup>Based on J. L. Nolte, P. C. Stancil, T.-G. Lee, N. Balakrishnan, and R. C. Forrey. Submitted to *Astrophys. J.*, 8/4/11.

## ABSTRACT

Along with  $\text{H}_2$ , HD has been found to play an important role in the cooling of the primordial gas in the formation of the first stars and galaxies. It has also been observed in a variety of cool molecular astrophysical environments. The rate of cooling by HD molecules requires a knowledge of collisional rate coefficients with the primary impactors, H, He, and  $\text{H}_2$ . To improve knowledge of the collisional properties of HD, we present rate coefficients for the He-HD collision system over a range of collision energies from  $10^{-5}$  to  $5 \times 10^3 \text{ cm}^{-1}$ . Fully quantum mechanical scattering calculations were performed for initial HD rovibrational states of  $j = 0$  and 1 for  $v = 0$  to 17 which utilized accurate diatom rovibrational wavefunctions. Rate coefficients of all  $\Delta v = 0, -1,$  and  $-2$  transitions are reported. Significant discrepancies with previous calculations, which used a smaller basis set and adopted harmonic HD wavefunctions for excited vibrational levels, were found. Applications of the He-HD rate coefficients in various astrophysical environments are briefly discussed.

## 2.1 INTRODUCTION

While  $\text{H}_2$  has long been acknowledged as the main coolant in the primordial gas during the formation of the first baryonic objects, nevertheless the other primary coolant, HD, while less plentiful, may in certain circumstances play a comparable or even greater role in the cooling of molecular clouds to form the first stars. Although the HD/ $\text{H}_2$  abundance ratio after freeze-out is about  $10^{-3}$  [1, 31, 32, 33], HD may contribute significantly relative to  $\text{H}_2$  in cooling the astrophysical media due to its permanent dipole moment — which allows transitions of  $\Delta j = \pm 1$  — and smaller rotational constant. The smaller spacing between energy levels and larger collisional rate coefficients allow for enhanced excited state populations and greater rates of energy transfer between the radiation field and matter [1].

The relative importance of  $\text{H}_2$  and HD in determining the thermal balance has been the subject of many studies. The question is important, as stellar masses ultimately depend

on the cooling properties of the dominant coolant in cloud collapse. Puy and Signore [34] found that, for a  $10^9 M_{\odot}$  protocloud, HD cooling would dominate at a matter temperature  $T \sim 200$  K (close to the HD  $j = 1 \rightarrow 0$  transition energy of 128 K), leading to a decrease in the matter temperature and possibly to cloud fragmentation. Similarly, it was shown by Flower and Pineau des Fôrets [35] that HD would contribute as much as 20 percent of the radiative cooling in the post-shock gas. The contribution of HD to the heating of the gas when the radiation temperature exceeds the kinetic temperature was addressed by Flower [1], who showed that the HD contribution could become comparable to  $H_2$  at a redshift of  $z \sim 25$ . Likewise, Galli and Palla [32] showed that HD dominates the heating of primordial gas at temperatures 150 K in the low-density limit. More recently, Lipovka et al. [36] used an updated HD cooling function to show that the HD cooling efficiency was significant even at high gas densities and temperatures, with the HD contribution comparable to that for  $H_2$  at temperatures  $\geq 3000$  K.

However, there is a question of whether the primordial gas can reach sufficiently cool temperatures for HD cooling to dominate, and many early studies indicating an enhanced role of HD focused only on the beginning stages of cloud collapse. Nakamura and Umemura [37, 38] examined the conditions under which gas temperature becomes sufficiently cool ( $\sim 100 - 200$  K) for HD to become the primary regulator of thermal evolution. They concluded that, under the conditions at which the first pregalactic objects are expected to collapse (namely, at  $z \sim 10 - 10^2$  and masses of  $10^5 - 10^8 M_{\odot}$  in a cold dark matter cosmology), there will be an insufficient amount of  $H_2$  to lower the temperature to the requisite values (contrary to the findings of Galli and Palla [39]), although HD cooling will sufficiently lower the gas temperature to produce fragment masses a few times smaller than without HD cooling. Moreover, they point out that HD may still play a dominant role in star formation in metal-deficient early galaxies, where gas photoionized by ultraviolet (UV) radiation favors

the formation of sufficient amounts of  $\text{H}_2$  to cool the gas below the threshold temperature, beyond which HD cooling controls the cloud fragmentation.

There may be other star formation scenarios in which the gas can become sufficiently cool for HD cooling to dominate. Uehara and Inutsuka [40] investigated the role of HD cooling in the evolution of a post-shock fragmentation and concluded that HD cooling dominates for a shock velocity of  $300 \text{ km s}^{-1}$  and leads to the formation of low-mass stars and possibly brown dwarfs. Fossil H II regions have also been identified as an environment in which HD may play a significant role. Nagakura and Omukai [41] found that within initially ionized massive ( $10^6 M_\odot$ ) halos, HD cooling could lead to the formation of low-mass stars. The possibility of HD moderated formation of low-mass stars was also investigated by Machida et al. [42] within the remnants of primordial supernovae. Simulations by McGreer and Bryan [43] cast doubt on whether HD cooling in ionized halos would lead to formation of significantly lower mass stars, but showed that in low-mass ( $\sim 10^5 M_\odot$ ) unperturbed halos in which HD surpassed  $\text{H}_2$  cooling, relatively low mass stars ( $\sim 6$  times lower than without HD cooling) could form.

Of course, the accuracy of any model of star collapse depends on the chemical data employed. Collisional rate coefficients are one fundamental ingredient in determining the thermal balance of the molecular gas and in this work we consider the quenching of HD excitation due to He collisions. For the He-HD system, the most recent calculation of rate coefficients for collisional rovibrational excitation were performed by Roueff and Zeippen [4] in a fully quantal close-coupling approach using the He- $\text{H}_2$  potential surface of Muchnick and Russek [44], hereafter referred to as the MR potential. Roueff and Zeippen reported rate coefficients for rovibrational transitions between the first 45 rovibrational levels of HD, with a maximum initial vibrational quantum number of 3. In this work, we extend their earlier calculations by computing all  $\Delta v = 0, -1$  and  $-2$  transitions for initial states  $v = 0 - 17$ ,  $j = 0 - 1$ , for temperatures  $10^{-4} \text{ K} \leq T \leq 10^3 \text{ K}$ . Further, Roueff and Zeippen adopted the harmonic approximation for the HD vibrational wavefunctions, while the current compu-

tations utilize explicit, numerical nuclear wavefunctions obtained on an accurate molecular hydrogen interaction potential.

## 2.2 COMPUTATIONAL DETAILS

Inelastic cross sections were obtained using the nonreactive scattering program MOLSCAT developed by Hutson and Green [45]. In the close-coupling method employed here, the total wavefunction of the scattering system is expanded in terms of a basis set of Hermite polynomials. The resulting set of coupled differential equations in the expansion coefficients may then be solved and fit to the appropriate form in the asymptotic region. The MR potential surface for He-H<sub>2</sub> was used, but with bond lengths scaled and the H-D center of mass along  $r$  shifted to account for the change in the D mass. This potential was the subject of a study by Lee et al. [46], in which calculations of total He-H<sub>2</sub> quenching rate coefficients showed it to give better agreement with experimental data than the more recent potential of Boothroyd et al. [47].

It is convenient to expand the atom-diatom interaction potential,  $V(r, R, \theta)$ , in terms of Legendre polynomials:

$$V(r, R, \theta) = \sum_{\lambda} v_{\lambda}(r, R) P_{\lambda}(\cos \theta), \quad (2.1)$$

where  $r$  is the internuclear distance of HD,  $R$  the distance of He from the diatom's center of mass, and  $\theta$  the angle between  $\mathbf{r}$  and  $\mathbf{R}$ . The scattering equations then take the form [48]

$$\left[ \frac{d^2}{dR^2} - \frac{l(l+1)}{R^2} + k_{vj}^2 \right] F(vjlpJ|R) = 2\mu \sum_{v'j'l'J} \{ f_{\lambda}(jl, j'l'J) y_{\lambda}(vj, v'j'|R) F(v'j'l'pJ|R) \}, \quad (2.2)$$

where  $k_{vj}^2 = 2\mu(E - \epsilon_{vj})$ ,  $E$  being the total energy,  $\epsilon_{vj}$  the energy of the rovibrational state, and  $v, j, l, p$ , and  $J$  being the vibrational, rotational angular momentum, orbital angular momentum, parity, and total angular momentum quantum numbers, respectively;  $f_{\lambda}(jl, j'l', J)$  is a Percival-Seaton coefficient, and

$$y_{\lambda}(vj, v'j'|R) = \int_0^{\infty} \chi^*(vj|r) v_{\lambda}(r, R) \chi(v'j'|r) dr, \quad (2.3)$$

$\chi(vj|r)$  being the vibrational wavefunctions of HD.  $\epsilon_{vj}$  and  $\chi(vj|r)$  are obtained by solving the diatom nuclear Schrödinger equation with the H<sub>2</sub> potential of Schwenke [49] and a basis of Hermite polynomials.

The cross sections are obtained from the scattering matrix  $S_l$  via

$$\sigma_{vj \rightarrow v'j'} = \frac{\pi}{k_{vj}^2(2j+1)} \sum_{J=0}^{J_{\max}} \sum_{l=|J-j|}^{|J+j|} \sum_{l'=|J-j'|}^{|J+j'|} (2J+1) |\delta_{vv'} \delta_{jj'} \delta_{ll'} - S_J(vjl, v'j'l')|^2. \quad (2.4)$$

Collision rate coefficients are obtained by averaging the cross sections over a Boltzmann distribution of energies at a given temperature  $T$ :

$$k_{vj \rightarrow v'j'}(T) = \left( \frac{8}{\pi \mu k_b^3 T^3} \right)^{1/2} \int_0^\infty \sigma_{vj \rightarrow v'j'}(E_{vj}) E_{vj} e^{-E_{vj}/(k_b T)} dE_{vj}, \quad (2.5)$$

where  $E_{vj} = E - \epsilon_{vj}$  is the kinetic energy in the  $vj$  initial state.

The calculations employed a sizable basis set of at least 90 states for each collision energy and initial rovibrational state. The basis states ranged over vibrational levels from at least  $v-3$  to  $v+1$ . The expansion of the interaction potential in each case included  $\lambda_{\max} \geq 29$ . Convergence was tested for all parameters, including number of partial waves  $l_{\max}$ , number of integration points, matching radius, basis set size, etc.

## 2.3 RESULTS

Figures 2.1 - 2.3 show cross sections and rate coefficients for different families of  $\Delta v$ ,  $\Delta j$  transitions over a large energy and temperature range. The data include the ultracold regime to demonstrate the effect of resonances near  $0.1 \text{ cm}^{-1}$  and the threshold behavior of the cross sections and rate coefficients as they approach the Wigner limit. The illustrated data are a small, but representative sampling of the entire set of calculations.<sup>2</sup>

In Figures 2.1 and 2.2, cross sections and rate coefficients for the dominant rotational quenching  $\{v, j = 1\} \rightarrow \{v' = v, j' = 0\}$  family of transitions are plotted, respectively. In general, we see an increase in the cross section and rate coefficient with vibrational state  $v$

---

<sup>2</sup>All computed cross section and rate coefficient data can be obtained from the UGA Molecular Opacity Project database website, <http://www.physast.uga.edu/ugamop/>.

up to about  $v = 13$ , reflecting the decreasing energy gap between the first two rotational states of a given vibrational level. An orbiting resonance, which appears near  $0.2 \text{ cm}^{-1}$  in the cross section for  $v = 0$ , is seen to migrate to  $0.03 \text{ cm}^{-1}$  by  $v = 13$  as shown in Figure 2-1. The resonance is responsible for the peak in the rate coefficients near  $0.5 \text{ K}$ , but also causes the increase in the rate coefficients for decreasing temperatures below  $\sim 10 \text{ K}$ . For higher vibrational levels, however, the vibrational ordering breaks down as additional resonances at higher energies appear. This behavior is likely related to the increasing anharmonic nature of the diatom potential for large values of  $r$  which significantly affects the  $y_\lambda$  term given by Equation (2.3).

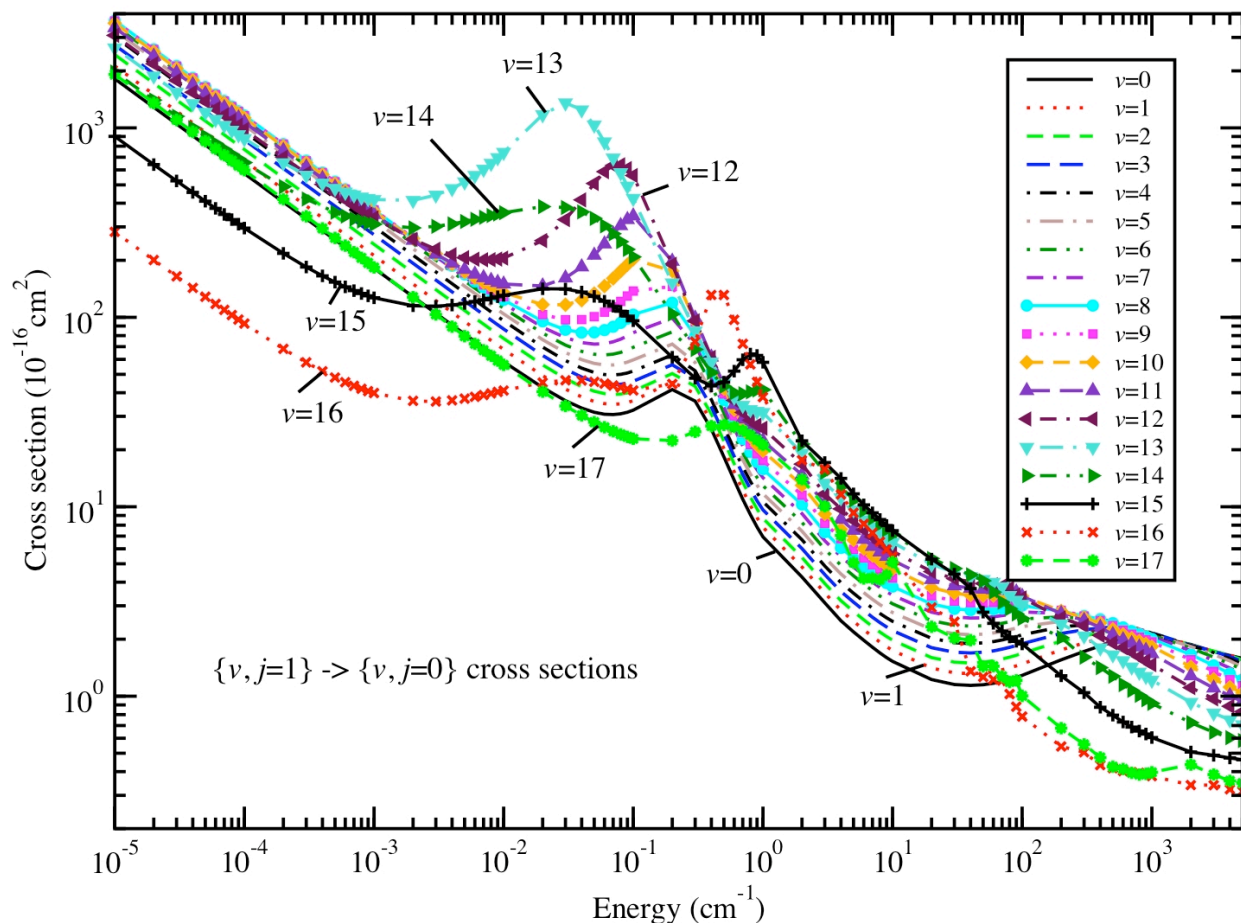


Figure 2.1: He-HD inelastic cross sections for  $\{v, j = 1\} \rightarrow \{v' = v, j' = 0\}$ .

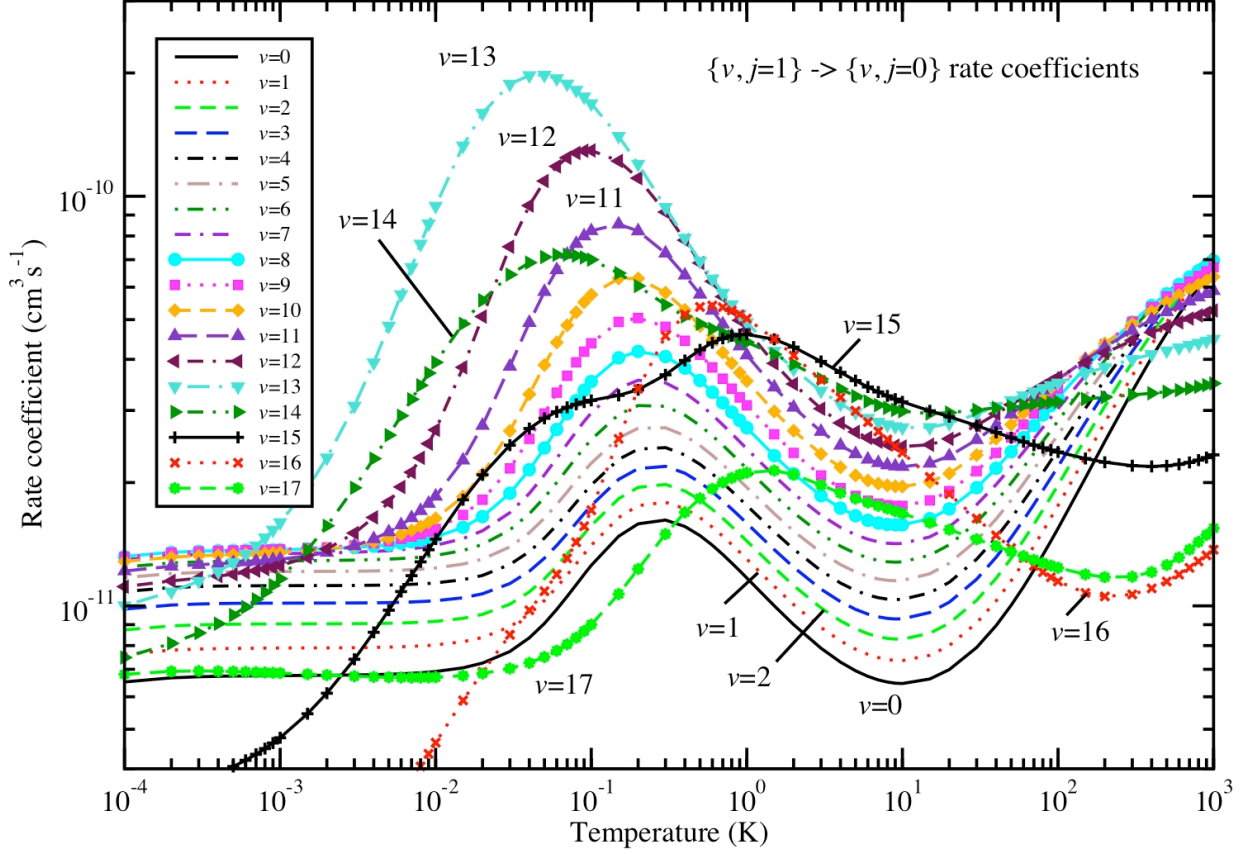


Figure 2.2: He-HD inelastic rate coefficients for  $\{v, j = 1\} \rightarrow \{v' = v, j' = 0\}$ .

Figure 2.3 shows two families of vibrational quenching rate coefficients, those of  $\{v, j = 0\} \rightarrow \{v - 1, j' = 8\}$  and  $\{v, j = 0\} \rightarrow \{v - 1, j' = 0\}$  transitions. Here again a general trend of increasing rate coefficients with increasing  $v$  is evident. However, the regular ordering is modified for higher vibrational states as the resonance near 0.5 K migrates to lower temperatures, vanishes, and is replaced by a higher temperature resonance. We note also that the rate coefficients are spread over a much wider range covering several orders of magnitude, with transitions from the higher vibrational states becoming comparable to the pure rotational transitions of Figure 2.2.

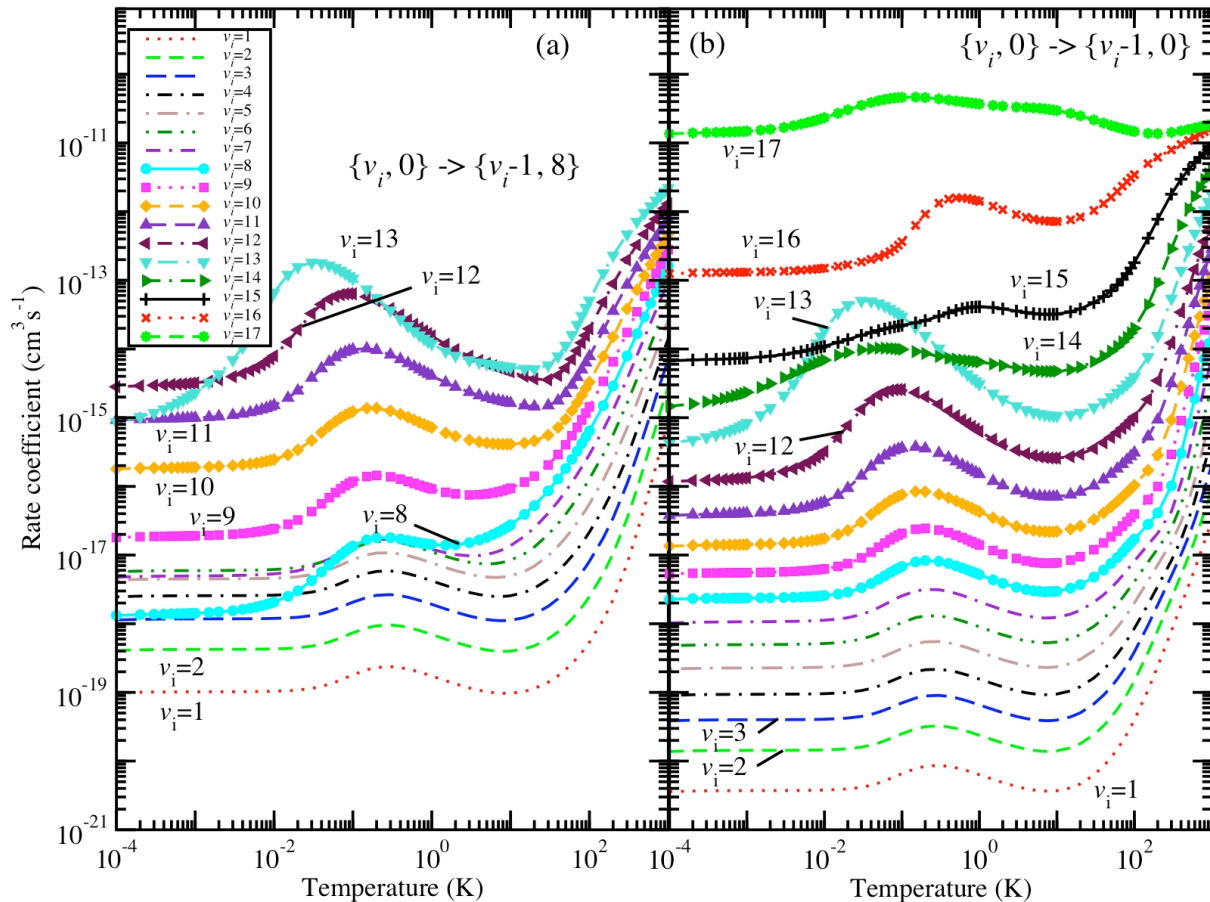


Figure 2.3: He-HD inelastic rate coefficients for (a)  $\{v, j = 0\} \rightarrow \{v - 1, j' = 8\}$  and (b)  $\{v, j = 0\} \rightarrow \{v - 1, j' = 0\}$ .

While we are unaware of any existing experimental data for He-HD inelastic collisions, the current results can be assessed by comparing to the limited previous calculations. Rotational transitions for  $v = 0$  have been computed by Schaefer [2] and Roueff and Zeppen [3] which were found to be in good agreement. Our rotational transitions are also found to agree with the previous work. As mentioned above, Roueff and Zeppen extended their earlier work to include rovibrational transitions, though limited to  $v \leq 3$  and  $T = 300\text{-}1000$  K. Therefore, focusing on vibrational transitions, Figure 2.4 compares the present results for

$\{v = 1, j = 1\} \rightarrow \{v' = 0, j'\}$  with those of Roueff and Zeippen. The agreement is fair, with a maximum discrepancy of about a factor of 2 for the case of  $j' = 8$ . When we compare results for the highest common initial vibrational level,  $v = 3$ , the agreement is less satisfactory. Comparing the results in Figure 2.5 for  $\{v = 3, j = 1\} \rightarrow \{v' = 2, j'\}$ , we find an order of magnitude difference. It is likely that the main source of this discrepancy lies in the difference in the respective basis set sizes, as our calculations utilize a basis set of at least a factor of two larger for all energies. As Roueff and Zeippen included no basis states with  $v > 3$ , we should expect the accuracy of their results to diminish at higher initial vibrational numbers. Moreover, in addition to our use of at least twice as many potential expansion terms in our calculation, we suspect another source of the discrepancy to lie in the fact that Roueff and Zeippen used the harmonic oscillator approximation for the HD vibrational wavefunctions in determining the potential matrix element  $y_\lambda(vj, v'j'|R)$ , whereas in the current work, as mentioned above, numerically determined wavefunctions for the actual HD interaction potential are adopted. It is expected that agreement should deteriorate for higher  $v$ , as the harmonic approximation becomes increasingly invalid. It has been pointed out by Forrey et al. [50] and Balakrishnan et al. [51] that, for transitions involving  $v \geq 2$ , the two methods may yield widely discrepant values.

To test this hypothesis and to further explore the discrepancy with the earlier work of Roueff and Zeippen, we plot in Figure 2.6 a selection of  $y_\lambda(vj, v'j'|R)$  for a range of  $\lambda$  using the MR potential and for both numerical and HO wavefunctions. Figure 2.6(a) displays matrix elements for  $v = v' = 3, j = j' = 1$  where it is seen that those based on HO wavefunctions are shifted to smaller  $R$  compared to matrix elements utilizing wavefunctions obtained on an anharmonic potential. The difference is more dramatic for  $v = v' = 10, j = j' = 0$  as displayed in Figure 2.6(b). Figures 2.6(c) and 2.6(d) display off-diagonal matrix elements corresponding to the initial and final states of Figure 2.5. Significant differences are again evident between matrix elements obtained with HO and anharmonic wavefunctions which may partially explain the discrepancies in the rate coefficients given in Figure 2.5. Further,

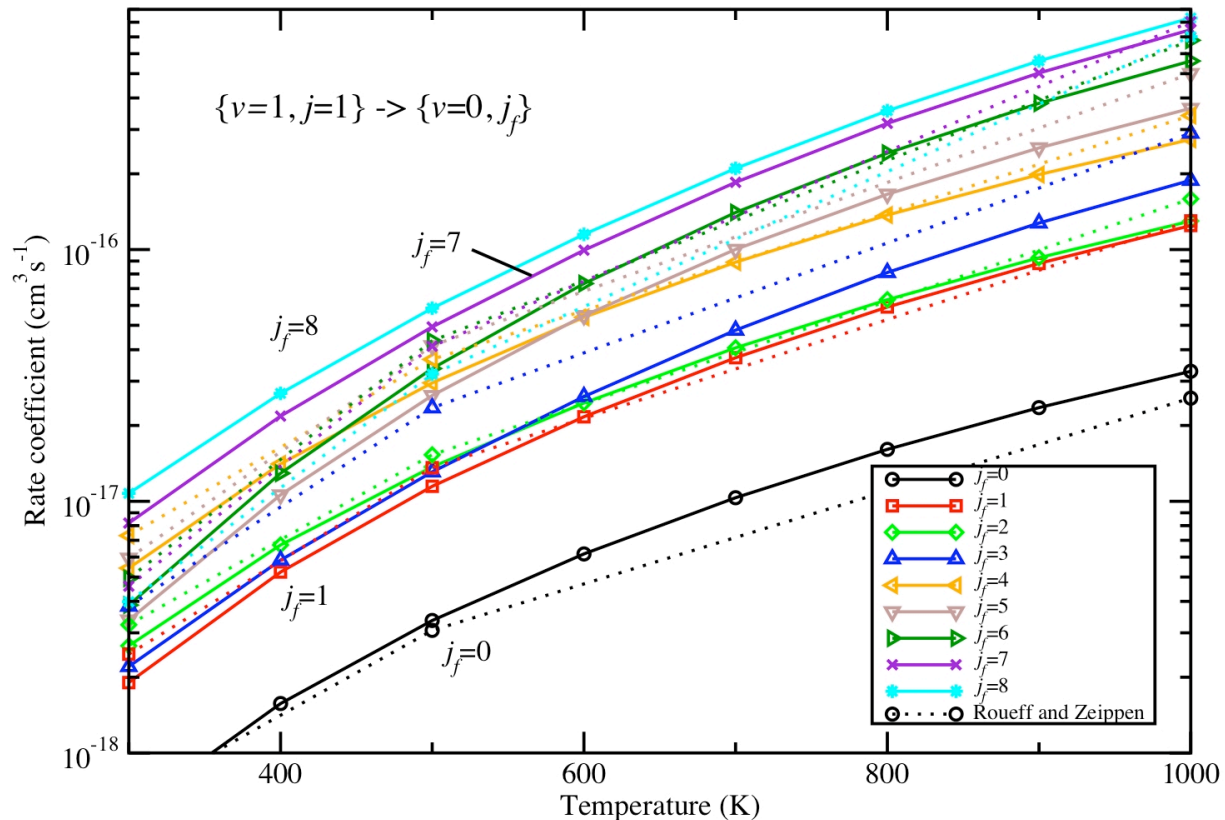


Figure 2.4: Comparison of He-HD inelastic rate coefficients for  $\{v = 1, j = 1\} \rightarrow \{v' = 0, j'\}$ : current results, solid lines; Roueff & Zeippen [4], dotted lines.

we note that the matrix elements displayed here are similar to those given for He-H<sub>2</sub> in Lee et al. [46].

Finally, the accuracy of inelastic rate coefficients are sensitive to the details of the PES. Lee et al. found that the MR potential gives total quenching rate coefficients for  $v, j = 1, 0$  in excellent agreement with experiment for He-H<sub>2</sub>. However, we are unaware of any measurements for  $v \geq 2$ . Unfortunately, the MR PES is only constrained by explicit ab initio energy data for H-H stretching distances of  $r = 1.2 - 1.6$  a.u. For larger  $r$ , MR adopt a physically reasonable extrapolation function, but which may lead to some uncertainty in

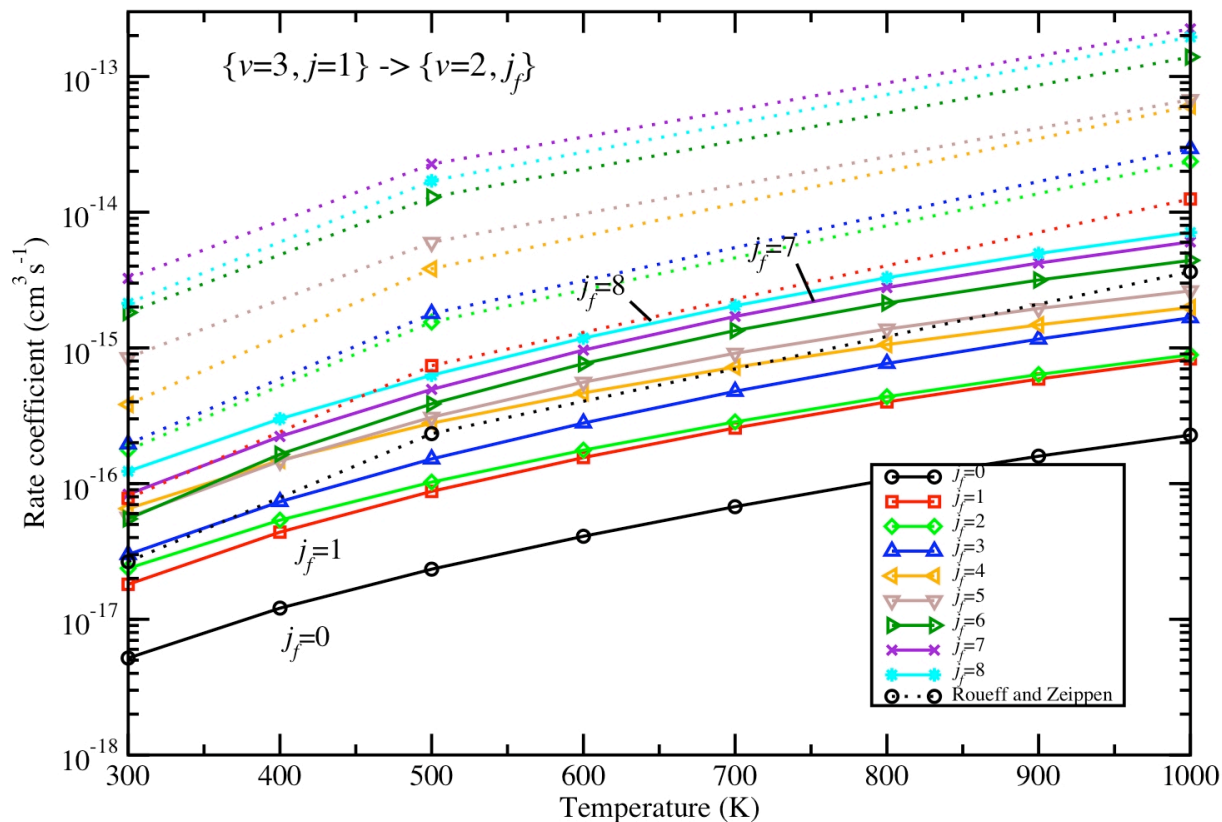


Figure 2.5: Comparison of He-HD inelastic rate coefficients for  $\{v = 3, j = 1\} \rightarrow \{v' = 2, j'\}$ : current results, solid lines; Roueff & Zeippen [4], dotted lines.

resulting collisional parameters for highly excited  $v$  or  $j$  levels. Mack et al. [52] explored variations in the large- $r$  extrapolation of the MR surface for He-H<sub>2</sub> inelastic rate coefficients for highly-excited rovibrational levels near dissociation, but found only small differences. More recently, Paolini et al. [53] computed the total three-body recombination rate coefficient for H-H-He collisions with the MR surface and found a 25% difference with experiment below 300 K. Agreement with experiment could be obtained with some modification to the large- $r$  part of the MR potential. As the three-body recombination rate is dominated by transitions to highly-excited H<sub>2</sub> bound and quasi-bound levels, this is a particularly sensitive, though

not unique, test of the large- $r$  behavior. Taken together, these observations suggests that the current inelastic rate coefficients for He-HD are uncertain by about 25% for the dominant transitions, while uncertainties for transitions with small rate coefficients are likely larger.

## 2.4 ASTROPHYSICAL IMPLICATIONS

A major motivation for this work as outlined in Section 2.1 is the possible importance of HD as a coolant during the formation of the first stars, so called Population III stars, from the primordial gas. Here we have focused on collisions due to He, but H and H<sub>2</sub> are also important impactors. In fact, most modeling studies of primordial gas collapse, have adopted the H-HD cooling function of Galli and Palla [32], which was actually obtained by mass-scaling the He-HD  $v = 0, j = 0 \rightarrow v' = 0, j' = 1$  rotational excitation rate coefficients of Schaefer [2]. More elaborate cooling functions have been constructed by Flower et al. [54] and Lipovka et al. [36] with the former considering H, He, and H<sub>2</sub> colliders, but the latter limited to H (see the summary in Ref. [55]).

While it is beyond the scope of this work to create an HD cooling function, the new rotational transition rate coefficients will likely have only a minor impact if included in new cooling function computations for  $T$  between  $\sim 100$  and  $\sim 1000$  K (100 K being the lowest temperature considered by [4]). However, for  $T < 100$  K, Flower et al. [54] used an extrapolated fit which could now be replaced by our explicit calculations which we note display an upturn in the rate coefficients near 10-50 K. This is potentially significant as HD is expected to be the dominant coolant below  $\sim 150$  K. On the other hand, the higher temperature portion of the HD cooling function will be modified and improved given our larger range of  $v$  and our use of larger basis sets and numerical HD rovibrational wavefunctions which result in a reduction in the rate coefficient magnitudes compared to the earlier calculations of Roueff and Zeppen, as shown in Figure 2.4. Lipovka [36] found that inclusion of rovibrational quenching rates for  $v = 1 - 3$  had a significant impact on the cooling function for  $T > 1000$  K and for all densities.

While the possible importance of HD in collapsing primordial clouds may have been first suggested by Varshalovich and Khersonskii [56], its significance as a coolant is still being debated today (see for example Ref. [55, 57]). Nevertheless, knowledge of collisional excitation rates are vital to the interpretation of observational data and for the application to other environments. In fact, Dalgarno and Wright [58] proposed that the pure rotational lines of HD and H<sub>2</sub> could be used to infer the deuterium abundance if the lines could be measured in nearby molecular clouds. They even hinted at the role of HD as a coolant in the “prestellar era.” Subsequently, pure HD rotational transitions have been observed with the *Infrared Space Observatory* by Bertoldi et al. [59] and Wright et al. [60], who detected the  $v = 0, j = 6 \rightarrow 5$  (or  $R(5)$ ) line and the  $v = 0, j = 1 \rightarrow 0$  ( $R(0)$ ) line, respectively, toward Orion Peak 1. Neufeld et al. [61] detected the pure rotational  $R(3)$  and  $R(4)$  transitions with *Spitzer* toward supernova remnant IC 443. They also obtained tentative detections toward the star-forming region GGD 37 and Herbig-Haro objects HH 54 and HH 7 which they use to estimate the interstellar deuterium abundance. Further, the  $R(0)$  line was detected in absorption toward the far-IR continuum sources Sgr B2 [62] and W49 [63].

Regarding rovibrational transitions, there appears to be a single detection, the  $v = 1 \rightarrow 0, j = 6 \rightarrow 5$  line was observed by Ramsay Howat et al. [64] toward Orion Peak 1 with the United Kingdom Infrared Telescope. However, as H<sub>2</sub> rovibrational emission lines have been observed from numerous photodissociation regions (PDRs), more HD rovibrational detections are likely given improvements in IR detector technology. In fact, HD chemistry and collisional excitation models have been incorporated into the Meudon PDR code, but so far limited to just rotational transitions [65, 66]. The availability of a comprehensive set of rovibrational collisional rate coefficients, such as begun here, should motivate enhancements in such modeling capabilities.

## 2.5 CONCLUSIONS

Collisional rate coefficients of HD are an important ingredient in the simulations of early star formation and interpretations of IR observational data. We have extended the calculations of Roueff and Zeppen for the He-HD system to include transitions with  $j=0$  and 1 for  $v=0$  to 17, and for which  $\Delta v = 0, -1$ , and  $-2$ . The energy and temperature range of the calculations have been expanded into the ultracold limit to resolve resonant features near 0.5 K. While our results generally agree with those of Roueff and Zeppen for  $v \leq 2$ , we find significant discrepancies for higher vibrational levels. We believe this is due primarily to differences in the sizes of our basis sets, and possibly also to the use of accurate HD numerical wavefunctions, as opposed to the harmonic approximation adopted in the previous work. The new He-HD rovibrational collisional rate coefficients should allow for a more accurate treatment of the thermal balance and emission spectra due to HD in a variety of molecular environments.

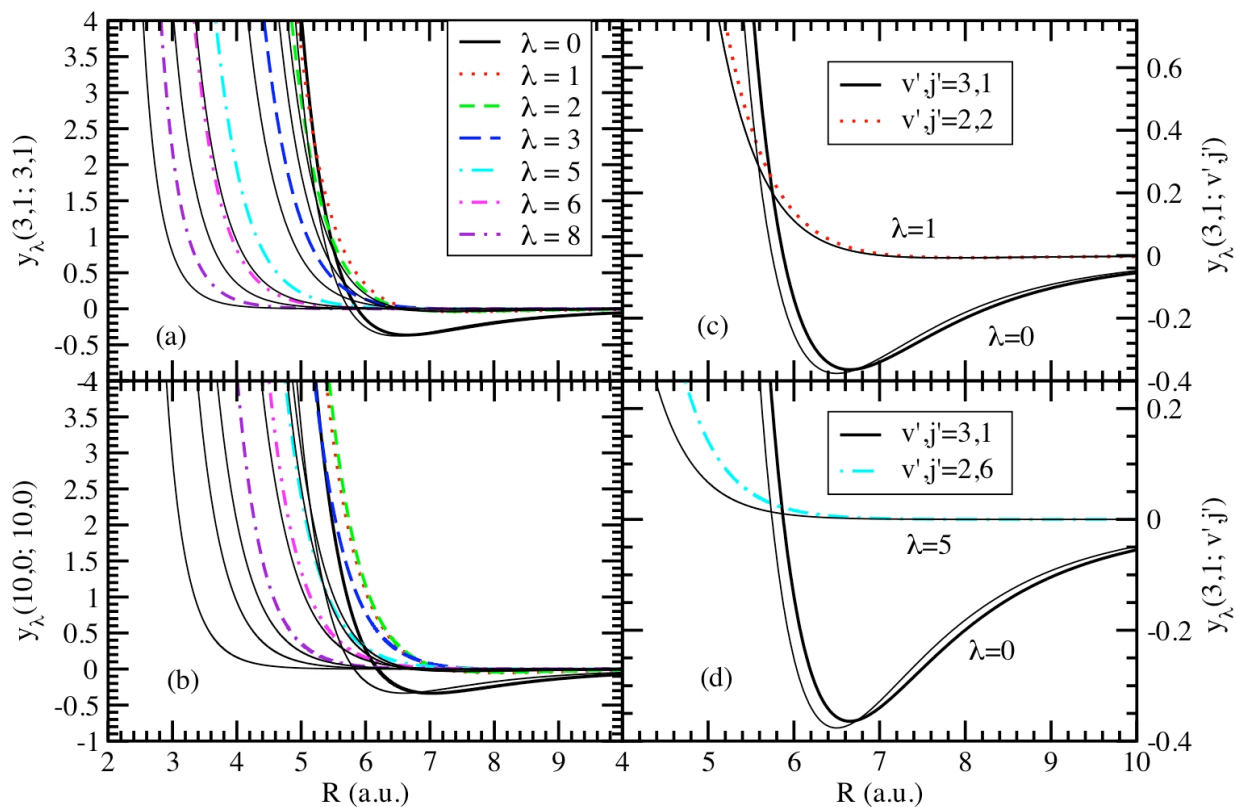


Figure 2.6: Comparison of interaction potential matrix elements  $y_\lambda(vj, v'j'|R)$  ( $10^{-4}$  a.u.) as given by Equation 2.3 using numerical rovibrational wavefunctions and harmonic oscillator (HO) wavefunctions. All HO results are given by thin solid black lines. (a) Diagonal elements for  $v, j = 3, 1$ . (b) Same as (a), but for  $v, j = 10, 0$ . (c) and (d) off-diagonal elements for  $\lambda = 1$  and  $\lambda = 5$ , respectively, compared to isotropic diagonal elements. All matrix elements are taken as positive values for plotting convenience.

## CHAPTER 3

### ISOTOPE EFFECTS IN COMPLEX SCATTERING LENGTHS FOR HE COLLISIONS WITH MOLECULAR HYDROGEN<sup>1</sup>

---

<sup>1</sup>Based on J. L. Nolte, B. H. Yang, P. C. Stancil, T.-G. Lee, N. Balakrishnan, R. C. Forrey, and A. Dalgarno, Phys. Rev. A **81**, 014701 (2010). Copyright (2010) by the American Physical Society. Reprinted with permission of publisher.

## ABSTRACT

We examine the effects of theoretically varying the collision-system reduced mass in collisions of He with vibrationally excited molecular hydrogen and observe zero-energy resonances for select atomic “hydrogen” masses less than 1 u or a “helium” mass of 1.95 u. Complex scattering lengths, state-to-state vibrational quenching cross sections, and a low-energy elastic scattering resonance are all studied as a function of collision-system reduced mass. Experimental observations of these phenomena in the cold and ultracold regimes for collisions of  $^3\text{He}$  and  $^4\text{He}$  with  $\text{H}_2$ , HD, HT, and DT should be feasible in the near future.

## 3.1 INTRODUCTION

Recent advances in creating dense samples of translationally cold molecules have generated much interest in understanding atomic and molecular interactions at temperatures close to absolute zero. Concurrently, collisions of rotationally and vibrationally excited molecules with cold atoms and diatomic molecules have received considerable theoretical and experimental attention [67, 68, 69, 70]. Investigation of chemical reactivity in cold and ultracold atom-molecule collisions and how the reactivity could be influenced by external electric and magnetic fields are topics of ongoing research in this area [68, 69, 70].

A key aspect of ultracold collisions is that the collisional outcomes are generally sensitive to details of the interaction potentials. At temperatures lower than 1.0 K, perturbations introduced by external electric and magnetic fields are comparable to the incident kinetic energy and external fields may strongly influence resulting collisional parameters. This is especially the case if the bound state energy levels of the molecule are modified by the presence of the external field inducing new resonances or eliminating existing ones [71]. There is also extensive literature on isotope effects in chemical reactions [72, 6] and recent studies indicated that these effects are more pronounced in ultracold collisions, especially when tunneling or threshold resonances are present [73, 7, 69]. Indeed, it has been shown that varying the reduced mass of the collision complex in a scattering calculation is equivalent to

adjusting the interaction potential [5]. Bodo *et al.* [7] demonstrated this for the F+H<sub>2</sub> reaction by artificially varying the mass of the hydrogen atom from 0.5 to 2.0 u. They found that for a fictitious “hydrogen” mass of 1.12 u, a zero-energy resonance is formed in this collision system yielding a zero-temperature rate coefficient that is about three orders of magnitude larger than the corresponding value for the F+H<sub>2</sub> reaction. This effect is somewhat akin to the Feshbach resonance method in which the scattering length is varied by sweeping a magnetic field across a Feshbach resonance that couples a bound state of the molecule to the energy of two colliding atoms [74, 75, 76].

Further, reduced mass tuning of the complex scattering length near zero-energy resonances may be useful in constructing complex optical potentials for each rovibrational level. The resulting 1-D potentials would be easier to use in subsequent applications (e.g. molecules in an external field) than the corresponding coupled-channel potentials. In this approach, the zero-energy resonances would play a similar role to that of magnetic Feshbach resonances when an asymptotic bound state model [77, 78, 79] is used to construct model potentials.

Here, we show the effect of artificially varying the mass of the hydrogen atom or the He atom in He collisions with H<sub>2</sub>, with an aim of understanding the sensitivity of the cross sections to small changes in the interaction potential as well as energies of quasibound triatomic complexes formed during the collision.

### 3.2 THE COMPLEX SCATTERING LENGTH<sup>2</sup>

In purely elastic scattering, the cross section at very low energies is determined solely by the scattering length  $a$ , defined as the real quantity

$$a \equiv - \lim_{k \rightarrow 0} \frac{\tan \eta^{(0)}(k)}{k}, \quad (3.1)$$

where  $\eta^{(0)}(k)$  is the  $s$ -wave phase shift. For inelastic scattering, however, we may redefine the phase shift as a complex quantity  $\eta_i^{(l)} = \lambda_i^{(l)} + i\mu_i^{(l)}$ , where  $l$  is the orbital angular momentum

---

<sup>2</sup>This section does not appear in Nolte *et al.* (2010) [80], but is added here to outline the relevant theory.

quantum number for the system, in which case the scattering length for the incoming channel becomes

$$a_i = - \lim_{k_i \rightarrow 0} \frac{\tan(\lambda_i^{(0)}(k_i) + i\mu_i^{(0)}(k_i))}{k_i}. \quad (3.2)$$

As we shall see, introducing a complex phase shift and scattering length will conveniently enable us to express several inelastic scattering observables in terms of the real and imaginary parts of these complex quantities.

It is well known that in the case of elastic scattering,  $\tan\eta^{(0)}(k)$  goes as  $k$  in the zero-energy limit [81]; i.e., for small  $k$ ,  $\eta^{(0)}(k) \sim k$ . For similar behavior in  $\lambda_i^{(0)}$  and  $\mu_i^{(0)}$ , we have [82]

$$\begin{aligned} a_i &= - \lim_{k_i \rightarrow 0} \frac{\sinh(2\lambda_i^{(0)}(k_i)) + i \sin(2\mu_i^{(0)}(k_i))}{k_i(\cosh(2\lambda_i^{(0)}(k_i)) + \cos(2\mu_i^{(0)}(k_i)))} \\ &\approx - \lim_{k_i \rightarrow 0} \left[ \frac{\lambda_i^{(0)}(k_i)}{k_i} + i \frac{\mu_i^{(0)}(k_i)}{k_i} \right]. \end{aligned} \quad (3.3)$$

Defining the real and imaginary parts of the scattering length

$$\alpha_i \equiv - \lim_{k_i \rightarrow 0} \frac{\lambda_i^{(0)}(k_i)}{k_i}, \quad (3.4)$$

$$\beta_i \equiv \lim_{k_i \rightarrow 0} \frac{\mu_i^{(0)}(k_i)}{k_i}, \quad (3.5)$$

we have

$$a_i = \alpha_i - i\beta_i. \quad (3.6)$$

In order for the absolute value of the elastic scattering matrix element  $S_{ii}^{(l)} = e^{2in_i^{(l)}}$  to be less than or equal to one, the imaginary part of the phase shift  $\mu_i^{(l)}$  – and therefore  $\beta_i$  – must be positive.

At very low energies, the inelastic  $s$ -wave cross section may be simply expressed in terms of the imaginary parts of either the phase shift or the scattering length. To see this, we note that the total inelastic cross section is given by

$$\begin{aligned} \sigma_{in} &= \frac{\pi}{k_i^2} \sum_{l=0}^{\infty} (2l+1) [1 - |S_{ii}^{(l)}|^2] \\ &= \frac{\pi}{k_i^2} \sum_{l=0}^{\infty} (2l+1) [1 - e^{-4\mu_i^{(l)}}]. \end{aligned} \quad (3.7)$$

Keeping only the  $l = 0$  term and Taylor expanding the exponential, we have

$$\sigma_{in}^{(0)} \approx \frac{4\pi\mu_i^{(0)}}{k_i^2}, \quad (3.8)$$

and using Equation (3.5) gives

$$\sigma_{in}^{(0)} \approx \frac{4\pi\beta_i^{(0)}}{k_i}. \quad (3.9)$$

As the  $s$ -wave is the only significant contributor in the ultracold limit, we may omit the superscript, and simply write, for the low-energy regime,

$$\begin{aligned} \sigma_{in} &= \frac{4\pi\mu_i^{(0)}}{k_i^2} \\ &= \frac{4\pi\beta_i}{k_i}. \end{aligned} \quad (3.10)$$

Moreover, since in the limit of  $k_i \rightarrow 0$  we have

$$\begin{aligned} S_{ii}^{(0)} &= e^{2in_i^{(0)}} \\ &\approx 1 + 2i\eta_i^{(0)} \\ &= 1 - 2ik_i(\alpha_i - i\beta_i), \end{aligned} \quad (3.11)$$

we can write, for the elastic scattering cross section (assuming only an  $s$ -wave contribution)

$$\begin{aligned} \sigma_{el} &= \frac{\pi}{k_i^2} |1 - S_{ii}^{(0)}|^2 \\ &= \frac{\pi}{k_i^2} |2ik_i(\alpha_i - i\beta_i)|^2, \\ &= 4\pi|a_i|^2, \end{aligned} \quad (3.12)$$

just as in the case of pure elastic scattering.

The inelastic rate coefficient also has a simple expression in terms of the imaginary part of the scattering length. The rate coefficient is given by

$$q_{in} = \langle v_i \sigma_{in} \rangle_{v_i}, \quad (3.13)$$

where  $\langle \rangle_{v_i}$  denotes an average over the collision velocity  $v_i$ , which is given by

$$v_i = \frac{\hbar k_i}{\mu}. \quad (3.14)$$

In the zero-energy limit, we have

$$\begin{aligned} q_{in} &= \frac{\hbar k_i}{\mu} \sigma_{in} \\ &= \frac{4\pi\hbar}{\mu} \beta_i. \end{aligned} \quad (3.15)$$

In the low energy limit, therefore, the two parameters  $\alpha_i$  and  $\beta_i$  go to constants which determine the elastic and inelastic cross sections and quenching rate coefficients, and are therefore of importance to the study of ultracold gases. In particular, for cold atom or molecule trapping experiments,  $\alpha_i$  and  $\beta_i$  give a measure of the efficiency of evaporative cooling. For large  $\beta_i$  ( $\sim q_{in}$ ), quenching collisions lead to a gain in kinetic energy and trap loss, while the cross sections of elastic collisions which thermalize the relative velocity of the particles are determined by the square of the magnitude of the scattering length,  $\alpha_i^2 + \beta_i^2$ .

### 3.3 METHODOLOGY

Our analysis is primarily based on the behavior of cross sections in the Wigner threshold regime [83] where the scattering length approximation can be conveniently used to characterize elastic and inelastic scattering [8, 84]. A number of previous studies have obtained the complex components of the scattering length including calculations of H-H<sub>2</sub> [8] and He-H<sub>2</sub> [84, 85, 86] scattering. Here we extend this analysis to scattering between He and a range of real and artificial isotopes of H<sub>2</sub>. Specifically, we consider the three cases in which we set one atom in the diatom to be H, D, or T and vary the mass of the other atom giving collisions of the form <sup>3,4</sup>He-HX, <sup>3,4</sup>He-DX, and <sup>3,4</sup>He-TX, where X is varied over a large range of masses, excluding homonuclear cases. Thus the limit for the HX reduced mass as X approaches infinity is  $\mu = m_{\text{H}} = 1.00794$  u, that for DX is  $\mu = m_{\text{D}} = 2.0135532127$  u, and for TX it is  $\mu = m_{\text{T}} = 3.0160492$  u. The entrance channel in each case is selected to be  $v = 1$ ,  $j = 0$ , and we consider only collisions in the ultracold limit (we adopt a collision energy of  $10^{-6}$  cm<sup>-1</sup>, except in the case of the elastic  $p$ -wave scattering resonance). Artificially varying the helium mass is also considered for collisions with HD.

### 3.4 COMPUTATIONAL METHOD

Elastic and inelastic cross sections were obtained by performing close-coupling calculations using the non-reactive scattering program MOLSCAT [87]. The potential energy surface (PES) adopted here was that of Muchnick and Russek (MR, [88]); this surface, along with that of Boothroyd *et al.* (BMP, [89]), was discussed previously by Lee *et al.* [90] who performed state-to-state rovibrational scattering calculations for He-H<sub>2</sub> and found that the MR surface gave the best agreement with available experimental data at thermal energies. (See also Chapter 2, where the MR potential was adopted for <sup>4</sup>He-HD inelastic scattering.)

Here, the isotope dependencies are included by adjusting the collision system reduced mass, the mass of the diatom in determining the rovibrational energies, and the location of the diatom center of mass for specifying the Jacobi coordinates. We do not consider mass-dependent adiabatic or nonadiabatic corrections to the PES [91]. The scattering calculations are performed using the close-coupling method (see Section 2.2) with appropriate convergence tests performed for the basis set size, asymptotic matching distance, and number of quadrature points for evaluating the matrix elements of the interaction potential. Three partial waves were found to be adequate for convergence for the ultracold calculations while a larger number of partial waves was used for the elastic resonance studies.

### 3.5 RESULTS

It was previously predicted by Balakrishnan *et al.* [84] in their study of collisions of H<sub>2</sub> with <sup>3</sup>He and <sup>4</sup>He that for each vibrational level of H<sub>2</sub> one should find an associated bound state of He-H<sub>2</sub> lying below the dissociation limit of the He-H<sub>2</sub> complex. In what amounts to an adjustment of the well depth of the interaction potential between the atom and molecule, we here varied the reduced mass of H<sub>2</sub>. In Figure 3.1 we show the real (elastic) part of the scattering length as a function of  $\mu/\mu_{\text{H}_2}$ , where  $\mu_{\text{H}_2}$  is the reduced mass of H<sub>2</sub>. Zero-energy resonances are identified for the case of HX with <sup>3</sup>He and <sup>4</sup>He at mass ratios of 0.94 and

0.78. The former value is smaller than, but very close to, the physical reduced mass limit of  $\text{H}_2$ , i.e. of two H atoms. Possible resonances corresponding to bound states for the other isotopomer-He combinations may occur at much lower mass ratios than considered here. The effect of varying the helium mass for the He-HD case is shown in the inset of Figure 3.1. It is seen that a zero energy resonance occurs for a “helium mass” of  $\sim 1.95$  u.

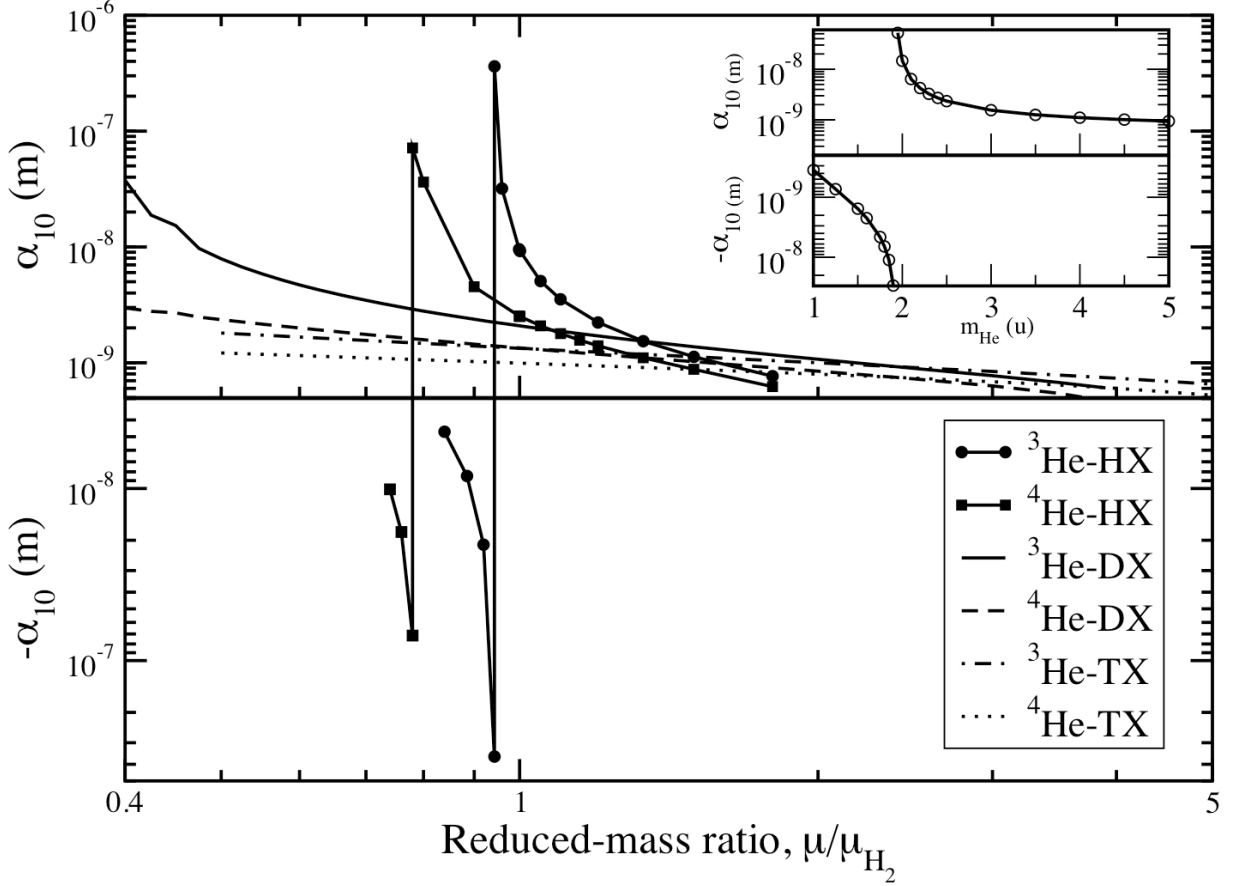


Figure 3.1: Real part  $\alpha_{10}$  of the scattering length for  $^3\text{He}$  and  $^4\text{He}$  collisions with HX, DX and TX as a function of the ratio of the reduced masses of the hydrogen isotopomer and  $\text{H}_2$ . Inset,  $\alpha_{10}$  for a variation of the He mass for He-HD collisions.

The imaginary part of the scattering length  $\beta_{10}$  is displayed in Figure 3.2 for  $^3\text{He}$  and  $^4\text{He}$  where it is seen to generally increase with decreasing mass ratio below a value of  $\sim 2$ . Some oscillatory behavior is also evident below  $\mu/\mu_{\text{H}_2} = 1$  for DX. For instance, a large resonance occurs near a mass ratio 0.58 for both  $^3\text{He-DX}$  and  $^4\text{He-DX}$ , and then another

peak at  $\sim 0.75$  followed by a much smaller one at 0.98. The inset shows the variation of  $\beta_{10}$  with the mass of the helium atom for He-HD collisions. For a “helium mass” of  $\sim 1.95$  u which corresponds to the zero-energy resonance in Figure 3.1,  $\beta_{10}$  increases by about three orders of magnitude compared to the  $^3\text{He}$  case and four-orders of magnitude compared to the  $^4\text{He}$  case. As discussed by Flasher and Forrey [92], the ratio  $\beta_{10}/\alpha_{10}^2$  is found to vary smoothly as the reduced mass is decreased through the zero-energy resonance, as shown for  $^3\text{He}$ - and  $^4\text{He}$ -HX in Figure 3.3.

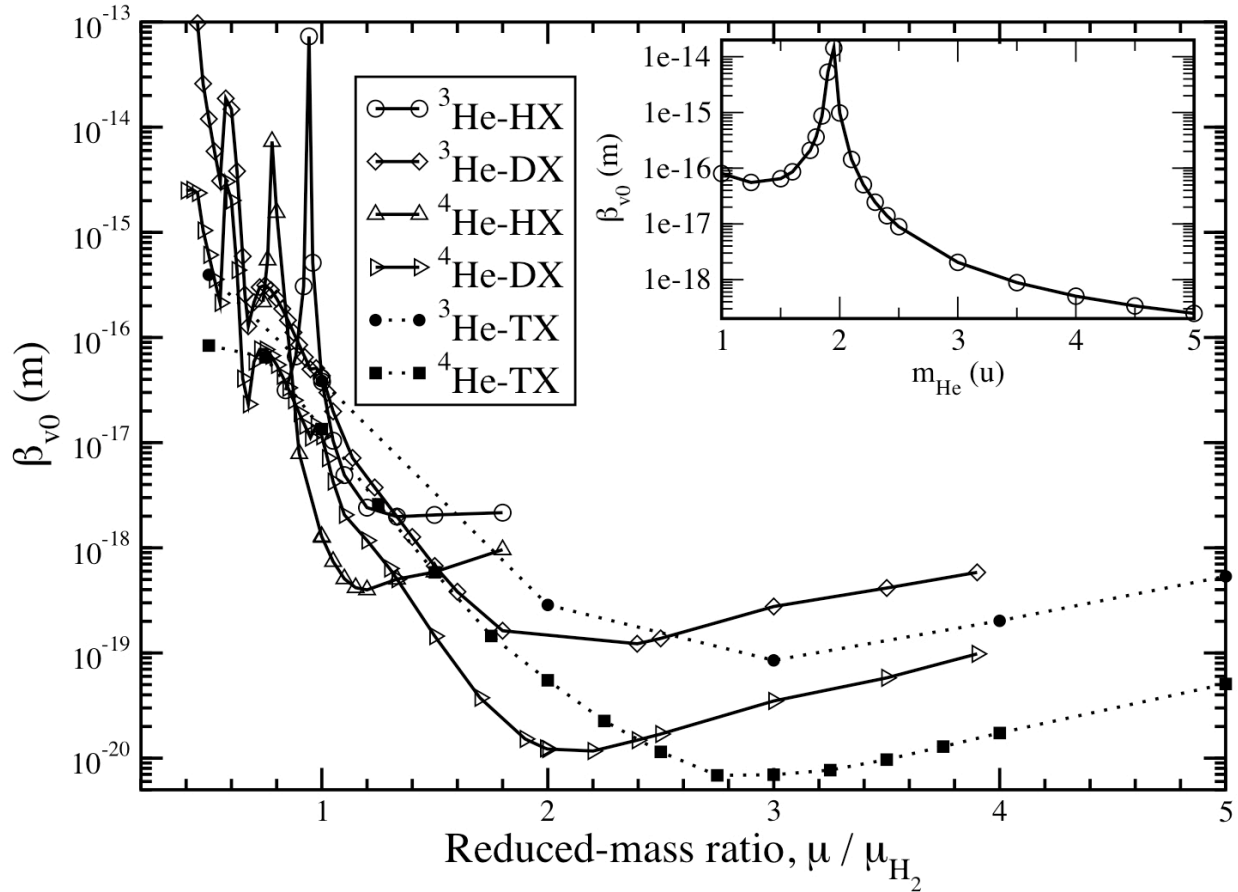


Figure 3.2: Same as in Figure 3.1, but for the imaginary part  $\beta_{10}$  of the scattering length.

The oscillatory behavior in  $\beta_{10}$  can be understood by considering the state-to-state cross sections for  $^3\text{He}$ -DX, for example, given in Figure 3.4. For  $\text{H}_2$ , rotational levels up to  $j' = 8$  are open in the ultracold limit, as shown by the energy level diagram in Figure 3.5. As the

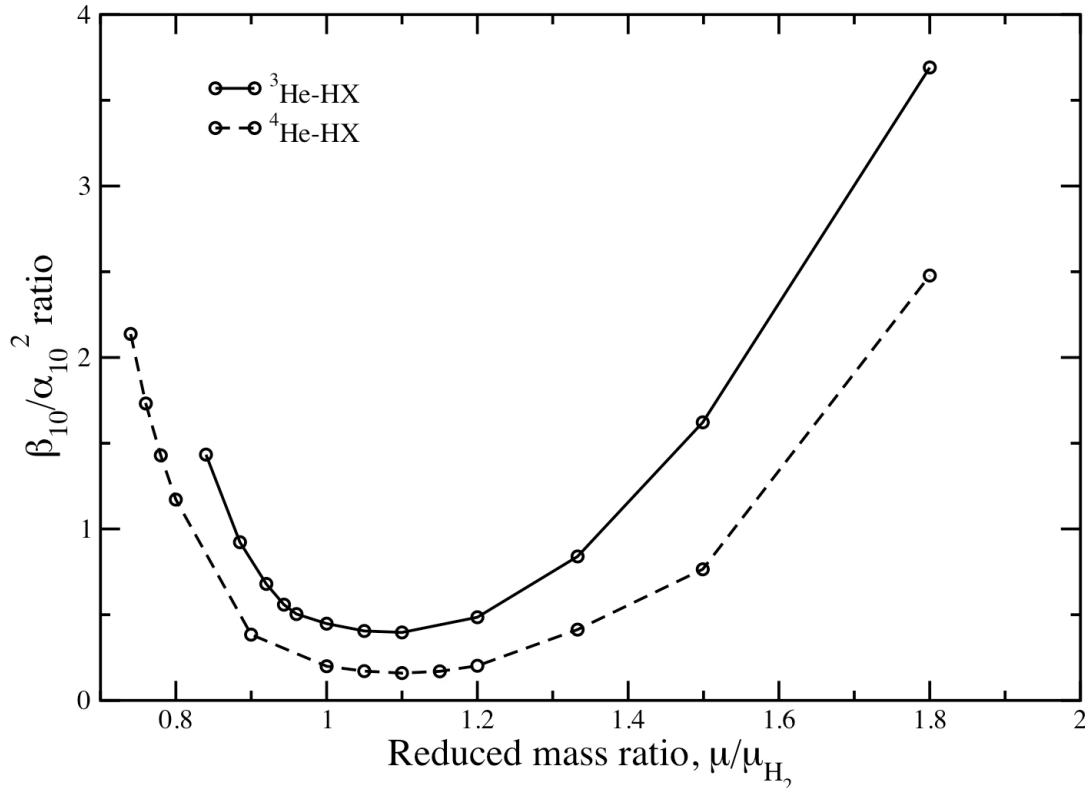


Figure 3.3: Ratio of  $\beta_{10}/\alpha_{10}^2$  as a function of reduced mass ratio for  $^{3,4}\text{He-HX}$ .

mass is decreased, the highest rotational state is not energetically accessible at the collision energy considered here. For example, the  $j' = 7$  state is only accessible for mass ratios greater than about 0.58, which is the location of a resonance in  $\beta_{10}$ . However, before this rotational state disappears into the continuum, its cross section decreases sharply to a minimum at a mass ratio of 0.68. Further, the state-to-state cross section for  $j' = 7$  has a maximum at 0.75, which corresponds to a maximum in  $\beta_{10}$ . The maximum for the mass ratio of 0.98 is then caused by the appearance of the  $j' = 8$  state as it becomes energetically open.

In their study of He-H<sub>2</sub> transitions with initial state ( $v = 1, j = 0$ ) using the BMP surface, Lee *et al.* [90] observed a similarly acute dependence of particular state-to-state rate coefficients on reduced mass. In increasing the molecular reduced mass, the  $j' = 8$  rate

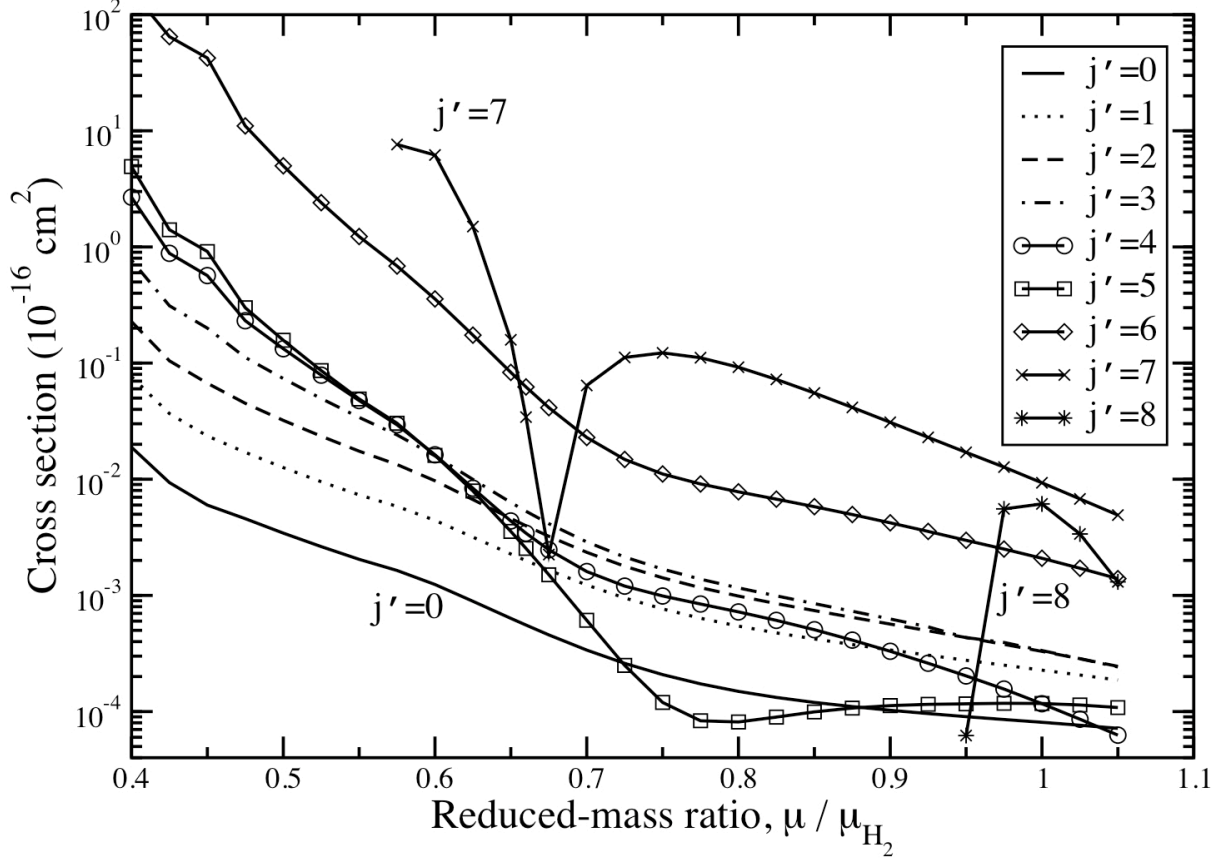


Figure 3.4: State-to-state quenching cross sections for  ${}^3\text{He-DX}(v = 1, j = 0) \rightarrow {}^3\text{He-DX}(v = 0, j')$  as a function of the DX/H<sub>2</sub> reduced-mass ratio.

coefficient was seen to decrease exponentially while other rotational states showed a much less sensitive dependence, with the  $j' = 10$  channel only becoming exoergic and contributing at a relatively high reduced mass. A somewhat similar situation can be seen in Figure 3.4, though using the MR PES.

In Figure 3.6(a), we present the elastic cross section in the cold to ultracold regimes for  ${}^4\text{He}$  collisions with H<sub>2</sub> and three physical isotopes. At ultracold energies, the elastic cross section decreases with increasing target mass. Also, a  $J = 1$ ,  $p$ -wave resonance occurs near  $\sim 1 \text{ cm}^{-1}$  for H<sub>2</sub>. Figure 3.6(a) shows that this resonance shifts to lower energies with increasing

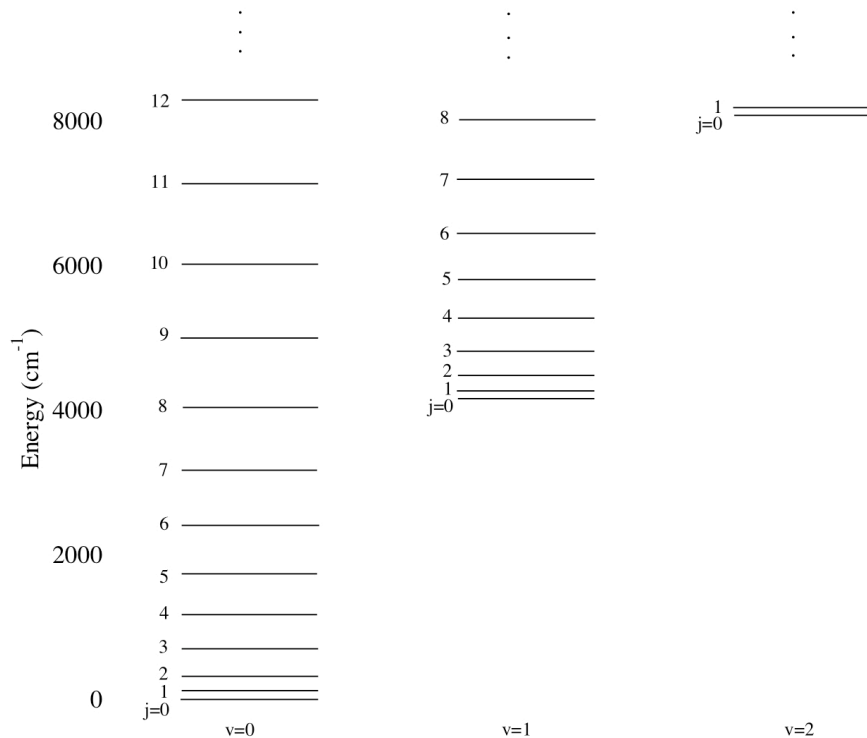


Figure 3.5: Rovibrational energy levels for first three values of  $v$  for He-H<sub>2</sub>.

molecular target mass with the peak becoming broader and having a maximum at a value of  $\sim 0.07$  cm<sup>-1</sup> for DT, but the magnitude of the resonance is largest for HT. Resonances for larger values of  $J$  are also present, but difficult to discern from the background cross section. However, as illustrated in Figure 3.6(b), the  $J = 2$  resonance for DT is prominent near  $\sim 1.5$  cm<sup>-1</sup>. The experimental detection of this low-energy resonance in the cold regime for the physical isotopomers would provide critical tests of the spherical component of the He-H<sub>2</sub> interaction potential.

An avenue for the measurement of low-energy He-H<sub>2</sub> cross sections is suggested by recent studies of Barletta *et al.* [93] who proposed the possibility of creating ultracold H<sub>2</sub> through collisions with ultracold rare gas atoms. In their method, cold molecules created by optical

Stark deceleration [94] are subjected to sympathetic cooling by thermal contact with laser-cooled rare gas atoms. Compared to other rare gas atoms, the inelastic cross sections for He with para-H<sub>2</sub> are largest, making it a favorable case for such an experimental study [93].

### 3.6 CONCLUSIONS

We have explored the sensitivity of elastic and inelastic scattering in ultracold He-H<sub>2</sub> collisions for a range of physical and artificial isotopes of H<sub>2</sub> and He. The purpose of these calculations was to explore how changes in bound state energy levels of H<sub>2</sub> and that of the triatomic He-H<sub>2</sub> van der Waals complexes influence scattering at low energies. We have shown that by varying the molecular (or helium) mass, a zero-energy resonance appears for the <sup>4</sup>He-H<sub>2</sub> and <sup>3</sup>He-H<sub>2</sub> collision systems with  $v = 1, j = 0$ , but for reduced-masses corresponding to nuclear masses less than that of the proton (or <sup>3</sup>He). For reduced mass ratios  $\mu/\mu_{\text{H}_2} < 1$ , the imaginary part of the scattering length for collisions with <sup>3,4</sup>He displays a number of oscillations and resonances which are attributable to energetically open rotational levels as the reduced mass is increased. An elastic resonance in the cold regime due to  $p$ -wave scattering is seen to shift to lower energies as the target mass is increased. For He-HD, a zero-energy resonance is found to occur for a “helium mass” of  $\sim 1.95$  u.

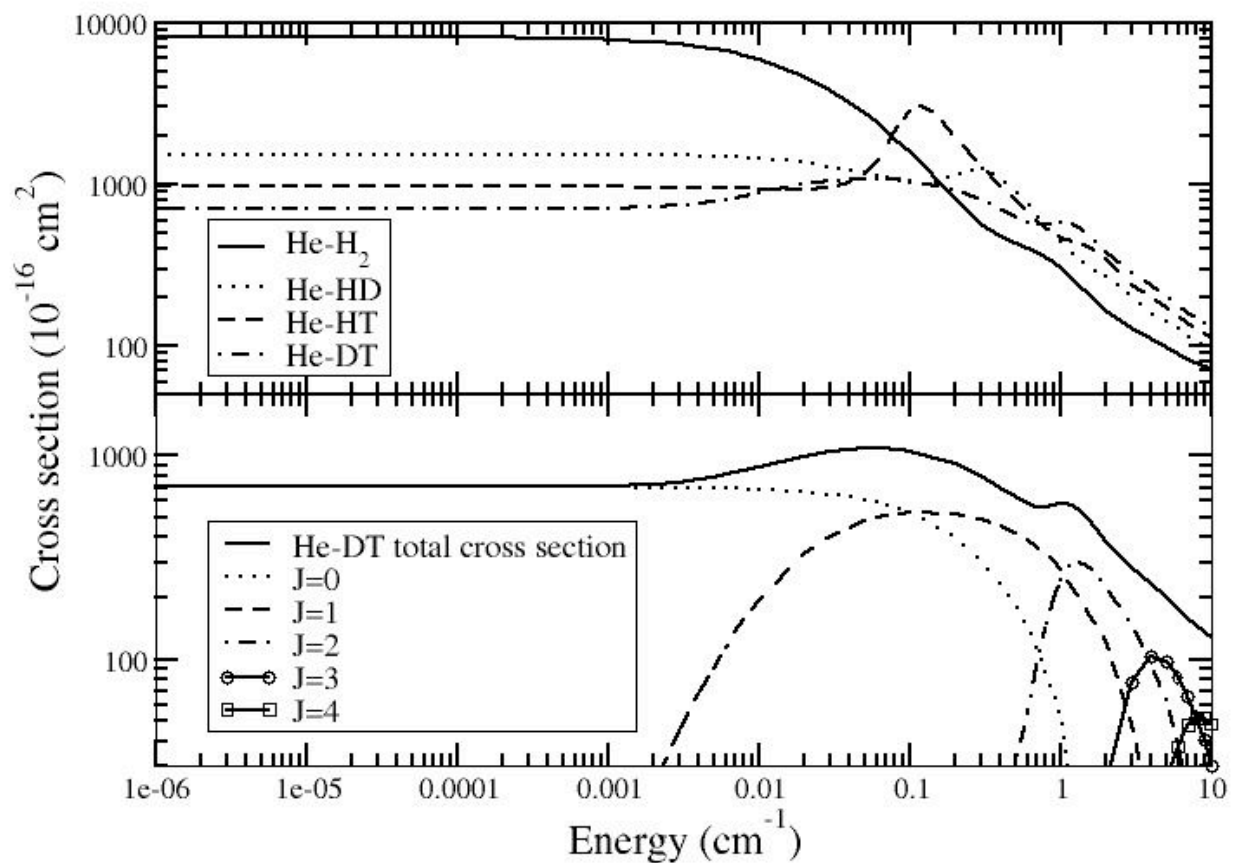


Figure 3.6: Low-energy elastic cross sections for  $^4\text{He}$  collisions with molecular hydrogen isotopomers with  $v = 1, j = 0$ . (a) Total cross sections for  $\text{H}_2$ , HD, HT, and DT. (b) Partial cross sections for the dominant partial waves for  $^4\text{He}$ -DT.

## CHAPTER 4

### FINAL-STATE RESOLVED CHARGE EXCHANGE BETWEEN $O^{7+}$ AND H: APPLICATIONS TO X-RAY EMISSION IN THE SOLAR SYSTEM<sup>1</sup>

---

<sup>1</sup>Based on J. L. Nolte, Y. Wu, P. C. Stancil, R. J. Buenker, D. R. Schultz, Y. Hui, I. N. Draganić, C. C. Havener, and M. J. Radović. To be submitted to Phys. Rev. A.

## ABSTRACT

Charge exchange cross sections are calculated for the collision system  $O^{7+} + H$  using the quantal molecular orbital close-coupling method. Calculations are performed over a range of collision energies from 0.01 eV/u to 1 keV/u for all important  $n$ ,  $l$ , and  $S$ -resolved states. In particular, we focus on the distribution of electron capture into the  $n=4$  and 5 manifolds, for both singlet and triplet states. We compare our results to new atomic orbital close-coupling, classical trajectory Monte Carlo, and experimental merged-beams results, and briefly discuss their relevance to solar system x-ray emission.

## 4.1 INTRODUCTION

Charge exchange between highly charged solar wind ions and neutral atomic species such as H and He has over the past two decades been found to be the underlying mechanism in x-ray emission from several sources within the solar system, as well as the dominant local contributor to the diffuse soft x-ray background (SXRb) seen in all directions. These discrete sources include comets, the exosphere of Mars, the x-ray aurora of Jupiter, and the geocorona, while the local contribution to the SXRb is thought to arise from diffuse interstellar neutrals which have entered the heliopause and undergo charge exchange with solar wind species. In this work, we present charge exchange cross sections obtained through a fully quantal treatment of one of the most important such ion-neutral pairs,  $O^{7+}$  and H, and discuss the implications of these results in understanding astrophysical x-ray emission within the solar system.

Consider as a simple example the SXRb, which has been revealed in recent decades through observations in the soft x-ray band (0.1-1.5 keV). These include the Wisconsin [9] and *ROSAT* [10] all-sky surveys, as well as observations by a sounding rocket equipped with microcalorimeters [11], the *Chandra X-ray observatory* [12], *XMM-Newton* [13], and the Japanese satellite *Suzaku* [14, 15]. While many of the sources of this emission are galactic or extragalactic, it was proposed by Cox [16] that observed temporal variations, or “long-term

enhancements” (LTE’s), in the diffuse x-ray emission below 1 keV may be due to a solar wind charge exchange (SWCX) mechanism, similar to that proposed by Cravens [17, 18] to account for cometary x-ray emission. (For a review of x-ray emission from comets, see Ref. [95].) In the SWCX mechanism, an x-ray is produced as a heavy solar wind ion de-excites after capturing an electron from a neutral H or He atom which has penetrated the heliosphere. It has since been suggested that, at lower energies (0.1-0.5 keV), as much as half of the SXRb may be due to heliospheric SWCX [19, 20]. Apart from its role as a foreground contaminant in observations of the galactic and extragalactic SXRb (see, e.g., Ref. [96]), heliospheric SWCX is worthy of study in its own right, as it allows us to remotely probe the composition, velocity, temporal variation, and spatial anisotropy of the solar wind [97, 98, 99].

The dominant contributing solar wind ions are most likely highly charged (bare or hydrogenic) C and O, due to their relatively high abundance. In the case of  $O^{7+}$ , the O VII  $K\alpha$  triplet around 570 eV (from the resultant  $O^{6+}$  ion after charge exchange), has been found to be a ubiquitous presence in repeated observations of the x-ray background [11, 12, 13, 14, 15], and in observations of the dark side of the moon by *Chandra*, where its presence has been attributed to charge exchange within Earth’s geocorona [100]. The forbidden transition ( $1s2s\ ^3S_1 \rightarrow 1s^2\ ^1S_0$ ) provides a useful diagnostic for charge exchange, as the intensity of this line is predicted to be much in excess of the resonant ( $1s2p\ ^1P_1 \rightarrow 1s^2\ ^1S_0$ ) and intercombination ( $1s2p\ ^3P_1 \rightarrow 1s^2\ ^1S_0$ ) lines when arising from charge exchange, unlike the case of a thermal plasma where the ratio of intensities is nearly unity [100, 101].

Additionally, charge exchange is known to contribute to planetary x-ray emission, in particular from the Martian exosphere and the x-ray aurora of Jupiter. Oxygen emission features dominate the latter in the 0.6 to 0.9 keV range, although primarily resulting from collisions with  $H_2$  [102, 103, 104, 105]. In the case of Mars, the dominance of the  $O^{6+}$  forbidden line to the exclusion of the intercombination line has again proved a valuable diagnostic pointing to charge exchange as the origin of ionization in the exosphere [106].

More recently, observations of the Cygnus Loop with *Suzaku* and *XMM-Newton* have revealed excess emission at 0.7 keV, most likely arising from charge exchange between  $O^{7+}$  and neutrals, which may account for an apparent anomalous enhancement of metal abundances in the region [107].

The accurate modeling of x-ray emission arising in these environments requires detailed knowledge of state  $(n, l, S)$  resolved charge exchange cross sections. Experimental investigations of highly charged ions colliding with neutrals have shown that the  $l$ -distribution of capture states may not be assumed to follow that predicted by a statistical population at typical solar wind velocities [108], and triplet-singlet ratios are likewise velocity-dependent, and may approach 3:1 only at energies above 10 keV/u [109]. Moreover, while many laboratory measurements of the relevant ion-neutral systems have been performed over the past several decades, these studies have largely been constrained by poor energy resolution and limited detector wavelength ranges. Theoretical methods are therefore a necessary complement to laboratory data.

The available theoretical methods vary in sophistication from fully quantal close-coupling (CC) methods to those based on further approximation such as semiclassical and quasi-classical approaches. The latter include the classical over-the-barrier (COB) method (e.g., Ryufuku et al. [110]), the multichannel Landau-Zener (LZ) approximation [111], and the more sophisticated classical trajectory Monte Carlo (CTMC) technique [112]. It has been shown, however, that while quasi-classical (i.e., CTMC) methods may model certain experimental trends reasonably well, their accuracy in determining even the  $n$ -state distribution for the relevant energies can be severely limited [113], thus necessitating the use of a quantal treatment. The quantum mechanical molecular orbital close-coupling (MOCC) method which we adopt will be described in the following sections.

## 4.2 MOCC METHOD

### 4.2.1 MOLECULAR STRUCTURE CALCULATIONS

Adiabatic potentials and nonadiabatic couplings for the  $O^{7+} + H$  scattering system have been obtained with the multi-reference single- and double-excitation configuration interaction (MRDCI) approach [114, 115], described below.

In the collision of  $O^{7+}$  with atomic hydrogen, an electron is transferred from the hydrogen atom to the oxygen ion in a state with principal quantum number  $n$  most likely equal to 5 or 4. Because the electron originally bound in  $O^{7+}$  remains in the tightly-bound 1s shell, the captured electron's state is essentially hydrogen-like in character. However, the typical basis set adopted in molecular structure calculations in such cases is the standard set developed for the neutral O atom with the addition of diffuse orbitals. This is clearly an insufficient treatment. Therefore, in Wu et al. [116] we have developed a hybrid basis set consisting of two components: i) the standard Dunning neutral atom basis and ii) a one-electron basis of hydrogen-like orbitals. The latter basis was optimized to reproduce nearly exactly the hydrogen-like Rydberg ion energies, and includes a large Gaussian basis set (17s, 11p, 9d, 6f, 3g). A (6s, 3p, 2d, 1f) basis contracted to [4s, 3p, 2d, 1f] was employed for hydrogen [117]. Using the optimized Gaussian basis, the MRDCI approach has been applied and a full CI calculation was carried out to compute the adiabatic potentials and nonadiabatic coupling matrix elements of the  $[OH]^{7+}$  system for internuclear distances between 1.0 and 50 a.u. Ten  $^1\Sigma^+$  and ten  $^3\Sigma^+$  electronic states in  $A_1$  symmetry and seven  $^1\Pi$  and seven  $^3\Pi$  electronic states in  $B_1$  symmetry have been calculated.

The adiabatic potentials for the singlet and triplet manifolds are given in Figures 4.1 - 4.4. (The unit of energy is 1 a.u. = 1 hartree = 27.2114 eV.) Accurate relative asymptotic energies of the  $[OH]^{7+}$  system have been obtained and compared with the corresponding experimental atomic spectroscopic data [118] in Table 4.1. When experimental data are lacking for some  $O^{6+}$  Rydberg levels, energies deduced from the calculations of Johnson et al. [119] have

been utilized where available. As shown in Table 4.1, for the MRDCI calculation with the optimized Gaussian basis set functions, the largest error in the relative asymptotic energies of the  $[\text{OH}]^{7+}$  system is about 0.00872 a.u. for the important channels with  $n$  of 4 and 5.

Given the optimized basis, the molecular wavefunctions are computed and the nonadiabatic radial and rotational coupling elements are calculated by applying a finite-difference method [114]. Examples of the coupling elements are given in Figures 4.5 - 4.8.

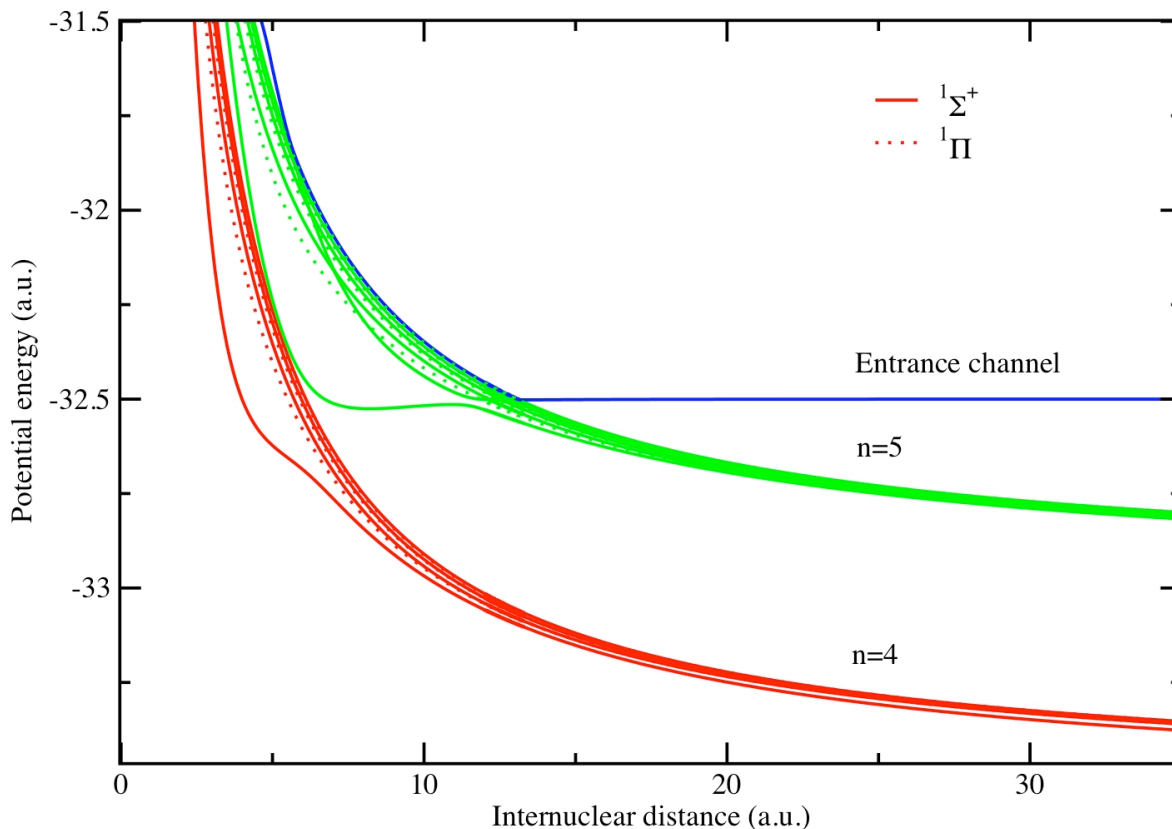


Figure 4.1: Singlet adiabatic potentials for  $\text{O}^{7+} + \text{H}$ .

#### 4.2.2 MOCC SCATTERING THEORY

For the calculation of charge exchange cross sections, we employed the fully quantal MOCC method. In this method, the coupled radial Schrödinger equations are solved for the coeffi-

Table 4.1: Comparison of asymptotic separated-atom energies (in a.u., where 1 a.u. = 1 hartree) between MRDCI calculations and experimental NIST data [118] for  $O^{7+} + H$ .  $\Delta E_{calc}$  is the energy separation of the asymptotic atomic state from the initial state  $O^{7+}(1s) + H(1s)$  in the MRDCI calculations.  $\Delta E_{exp}$  is the same quantity for the experimental values.  $\Delta E = |\Delta E_{exp} - \Delta E_{calc}|$ . The value marked \* has been calculated from the  $5\ ^1P_1 - 5\ ^1S_0$  transition wavelength in Johnson et al. [119]. Experimental energies marked N/A are not available.

Asymptotic atomic state	Mol. state	This work	Expt.[118]	$\Delta E_{calc}$	$\Delta E_{exp}$	$\Delta E$
Singlets						
$O^{6+}(1s4s\ ^1S) + H^+$	$1\ ^1\Sigma^+$	-33.54801	-33.57149	1.04801	1.04805	0.00004
$O^{6+}(1s4d\ ^1D) + H^+$	$2\ ^1\Sigma^+$	-33.53085	-33.55522	1.03085	1.03178	0.00093
	$1\ ^1\Pi$	-33.53081	-33.55522	1.03081	1.03178	0.00097
$O^{6+}(1s4f\ ^1F^o) + H^+$	$2\ ^1\Pi$	-33.52993	-33.55445	1.02993	1.03101	0.00108
	$3\ ^1\Sigma^+$	-33.52992	-33.55445	1.02992	1.03101	0.00109
$O^{6+}(1s4p\ ^1P^o) + H^+$	$4\ ^1\Sigma^+$	-33.52464	-33.54871	1.02464	1.02527	0.00063
	$3\ ^1\Pi$	-33.52462	-33.54871	1.02462	1.02527	0.00065
$O^{6+}(1s5s\ ^1S) + H^+$	$5\ ^1\Sigma^+$	-32.98837	*-33.01188	0.48837	0.48844	0.00007
$O^{6+}(1s5f\ ^1F^o) + H^+$	$6\ ^1\Sigma^+$	-32.98049	-33.00322	0.48049	0.47978	0.00071
	$4\ ^1\Pi$	-32.98041	-33.00322	0.48041	0.47978	0.00063
$O^{6+}(1s5g\ ^1G) + H^+$	$7\ ^1\Sigma^+$	-32.97918	N/A	0.47918	N/A	N/A
	$5\ ^1\Pi$	-32.97916	N/A	0.47916	N/A	N/A
$O^{6+}(1s5d\ ^1D) + H^+$	$6\ ^1\Pi$	-32.97831	-33.00136	0.47831	0.47792	0.00039
	$8\ ^1\Sigma^+$	-32.97829	-33.00136	0.47829	0.47792	0.00037
$O^{6+}(1s5p\ ^1P^o) + H^+$	$9\ ^1\Sigma^+$	-32.97173	-33.00035	0.47173	0.47691	0.00518
	$7\ ^1\Pi$	-32.97170	-33.00035	0.47170	0.47691	0.00521
$O^{7+}(1s) + H(1s)$	$10\ ^1\Sigma^+$	-32.50000	-32.52344	0	0	0
Triplets						
$O^{6+}(1s4s\ ^3S) + H^+$	$1\ ^3\Sigma^+$	-33.57893	-33.60229	1.07893	1.07885	0.00008
$O^{6+}(1s4p\ ^3P^o) + H^+$	$2\ ^3\Sigma^+$	-33.54756	-33.57377	1.04756	1.05033	0.00277
	$1\ ^3\Pi$	-33.54751	-33.57377	1.04751	1.05033	0.00282
$O^{6+}(1s4d\ ^3D) + H^+$	$3\ ^3\Sigma^+$	-33.53149	-33.55725	1.03149	1.03381	0.00232
	$2\ ^3\Pi$	-33.53146	-33.55725	1.03146	1.03381	0.00235
$O^{6+}(1s4f\ ^3F^o) + H^+$	$3\ ^3\Pi$	-33.53025	-33.55732	1.03025	1.03388	0.00363
	$4\ ^3\Sigma^+$	-33.53023	-33.55732	1.03023	1.03388	0.00365
$O^{6+}(1s5s\ ^3S) + H^+$	$5\ ^3\Sigma^+$	-33.00230	-33.02696	0.50230	0.50352	0.00122
$O^{6+}(1s5p\ ^3P^o) + H^+$	$6\ ^3\Sigma^+$	-32.98212	-33.01407	0.48212	0.49063	0.00851
	$4\ ^3\Pi$	-32.98191	-33.01407	0.48191	0.49063	0.00872
$O^{6+}(1s5f\ ^3F^o) + H^+$	$5\ ^3\Pi$	-32.98033	-33.00605	0.48033	0.48261	0.00228
	$7\ ^3\Sigma^+$	-32.98032	-33.00605	0.48032	0.48261	0.00229
$O^{6+}(1s5g\ ^3G) + H^+$	$6\ ^3\Pi$	-32.97922	N/A	0.47922	N/A	N/A
	$8\ ^3\Sigma^+$	-32.97914	N/A	0.47914	N/A	N/A
$O^{6+}(1s5d\ ^3D) + H^+$	$7\ ^3\Pi$	-32.97841	-33.00464	0.47841	0.48120	0.00279
	$9\ ^3\Sigma^+$	-32.97836	-33.00464	0.47836	0.48120	0.00284
$O^{7+}(1s) + H(1s)$	$10\ ^3\Sigma^+$	-32.50000	-32.52344	0	0	0

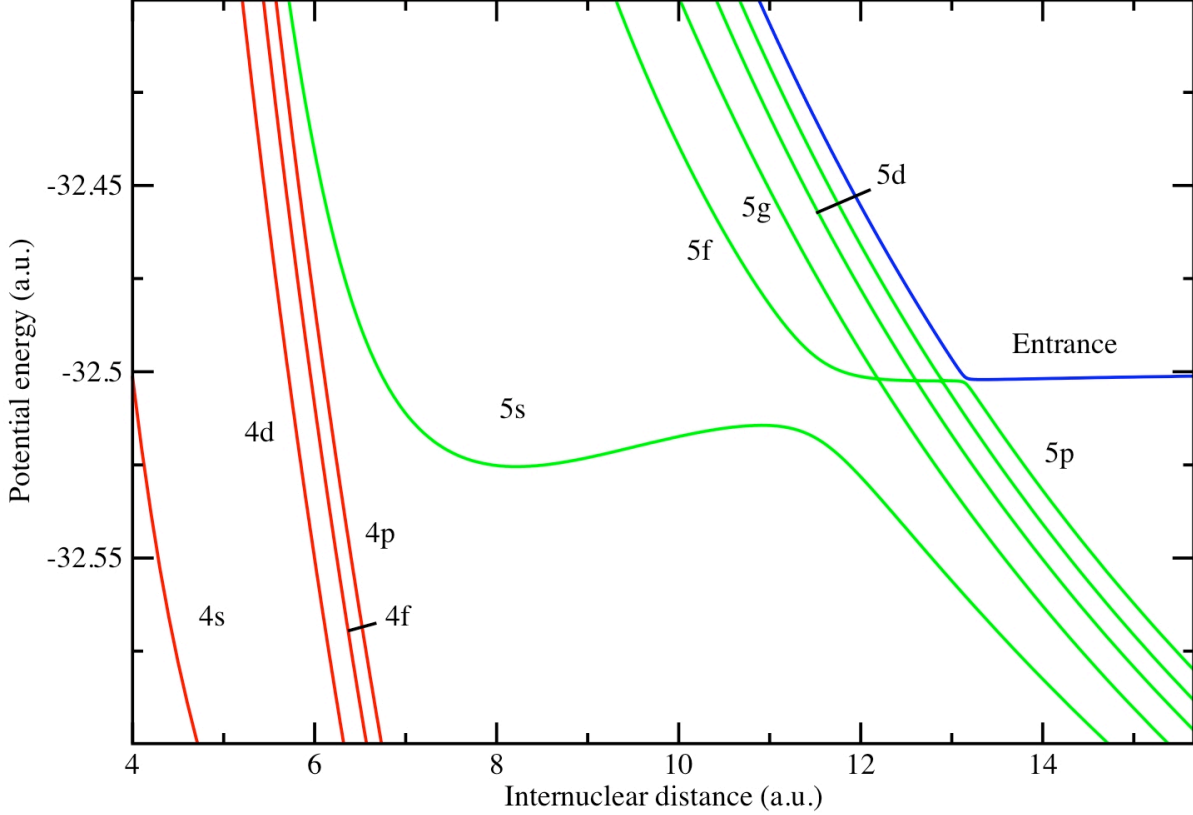


Figure 4.2: Singlet adiabatic potentials for  $O^{7+}+H$  (detail;  $^1\Sigma^+$  states only).

icients  $F_i(R)$  of the molecular orbitals  $\psi_i(\mathbf{s}, R)$  in the expansion of the total wavefunction

$$\Psi = \sum_j \psi_j(\mathbf{s}, R) F_j(\mathbf{R}), \quad (4.1)$$

where  $\mathbf{R}$  is the internuclear position vector and  $\mathbf{s}$  is the position of the electron in the body-fixed frame. The coupled radial equations are given by

$$\left[ \frac{\partial^2}{\partial R^2} - \frac{\mathbf{J}_i^2 - \Lambda_i^2}{R^2} + k_i^2(R) \right] R F_i(\mathbf{R}) = \sum_j [V_{ij}^R(R) + V_{ij}^C(R)] R F_j(\mathbf{R}), \quad (4.2)$$

in which  $\mathbf{J}_i$  is the total angular momentum operator and  $\Lambda_i$  the projection of the electronic angular momentum on the internuclear axis for state  $i$ , and  $k_i^2(R) = -2\mu(\epsilon_i(R) - E)$  where  $\epsilon_i(R)$  is the adiabatic potential energy curve for the  $i$ th molecular orbital,  $E$  is the collision

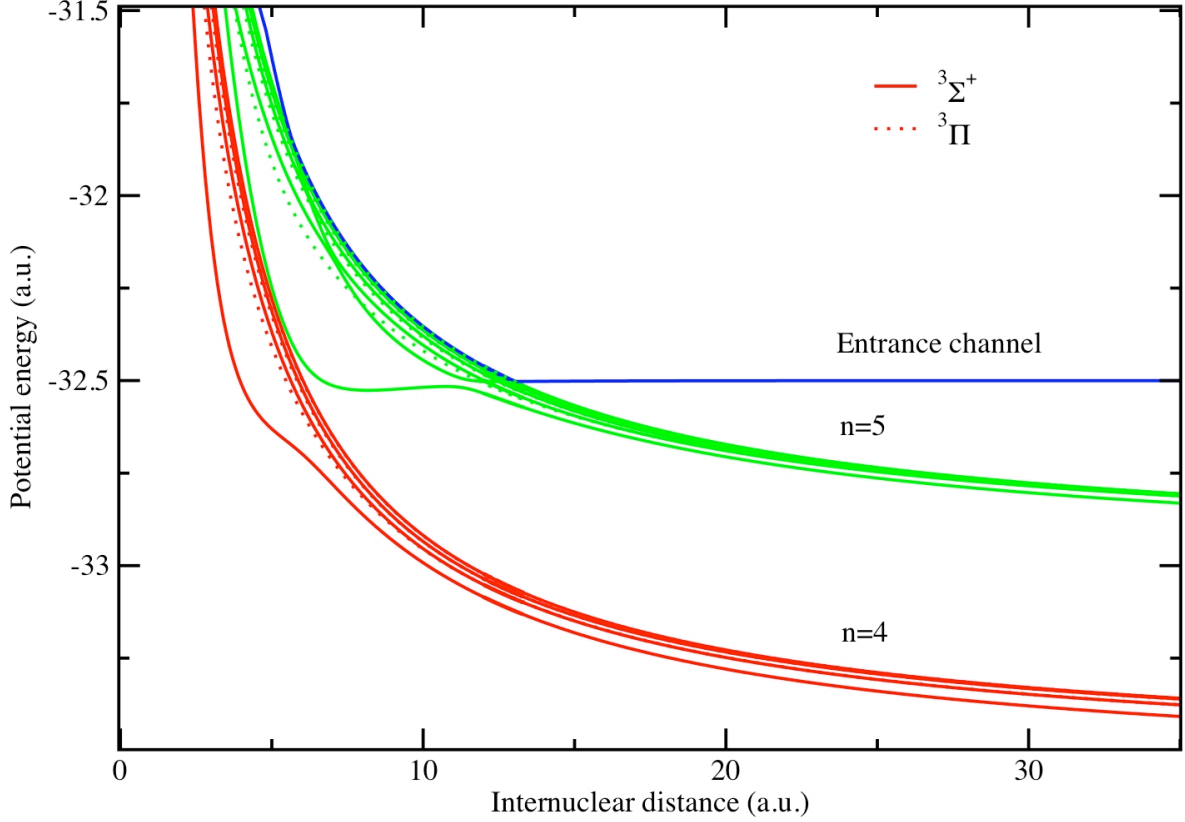


Figure 4.3: Triplet adiabatic potentials for  $O^{7+} + H$ .

energy, and  $\mu$  is the nuclear reduced mass. On the right side of the equation, the quantities  $V_{ij}^R(R)$  and  $V_{ij}^C(R)$  represent the radial and rotational couplings, respectively, and are given in terms of body-fixed electronic angular momentum operators  $L_x$  and  $L_y$  and polar coordinates  $R$ ,  $\Theta$ ,  $\Phi$  of  $\mathbf{R}$  in the space-fixed frame by

$$V_{ij}^R(R) = \left[ \langle i | -\frac{\partial^2}{\partial R^2} + \frac{L_x^2 + L_y^2}{R^2} | j \rangle - 2 \langle i | \frac{\partial}{\partial R} | j \rangle \frac{\partial}{\partial R} \right] \delta_{\Lambda_i, \Lambda_j} \quad (4.3)$$

and

$$V_{ij}^C(R) = \frac{2}{R^2} \left[ i \langle i | L_y | j \rangle \frac{\partial}{\partial \Theta} - \langle i | L_x | j \rangle \left( \frac{i}{\sin \Theta} \frac{\partial}{\partial \Phi} - \Lambda_j \cot \Theta \right) \right]. \quad (4.4)$$

In practical calculations, only the last and first terms of Equation (4.3) and Equation (4.4), respectively, are retained as the remaining terms are typically of smaller magnitude.

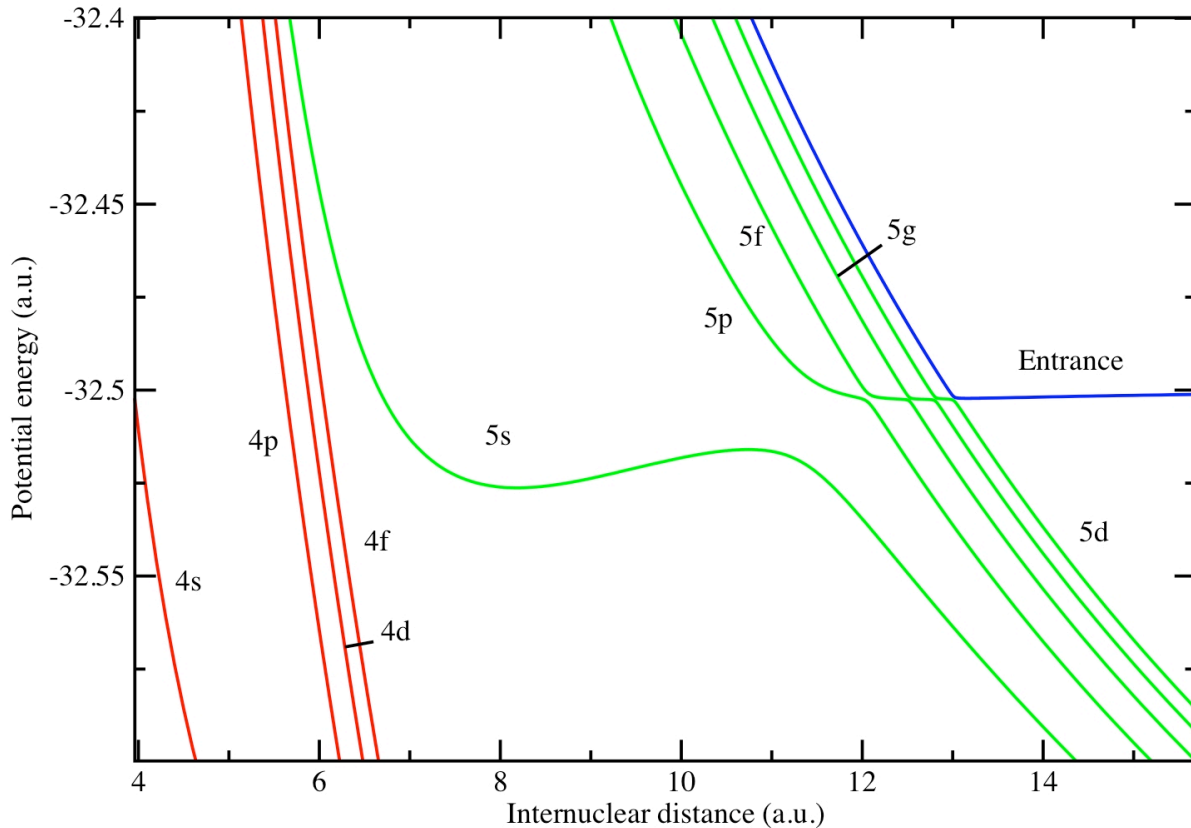


Figure 4.4: Triplet adiabatic potentials for  $O^{7+}+H$  (detail;  $^3\Sigma^+$  states only).

Transitions between states with the same symmetry  $^{2S+1}\Lambda$ , where  $S$  is the total electronic spin quantum number, are driven by the term  $A_{ij}(R) = \langle i | \frac{\partial}{\partial R} | j \rangle$  which appears in  $V_{ij}^R(R)$ . In the region of an avoided crossing between two adiabatic potential energy curves,  $A_{ij}$  can become nearly singular and create numerical difficulties (see Figures 4.7 and 4.8). For this reason, we make a unitary transformation of the molecular orbitals and channel functions to a diabatic basis in which  $A_{ij}(R)$  vanishes. The molecular orbitals in the diabatic representation are expanded in terms of adiabatic molecular orbitals:

$$\psi_i^d(\mathbf{s}, R) = \sum_j C_{ij}(R) \psi_j(\mathbf{s}, R), \quad (4.5)$$

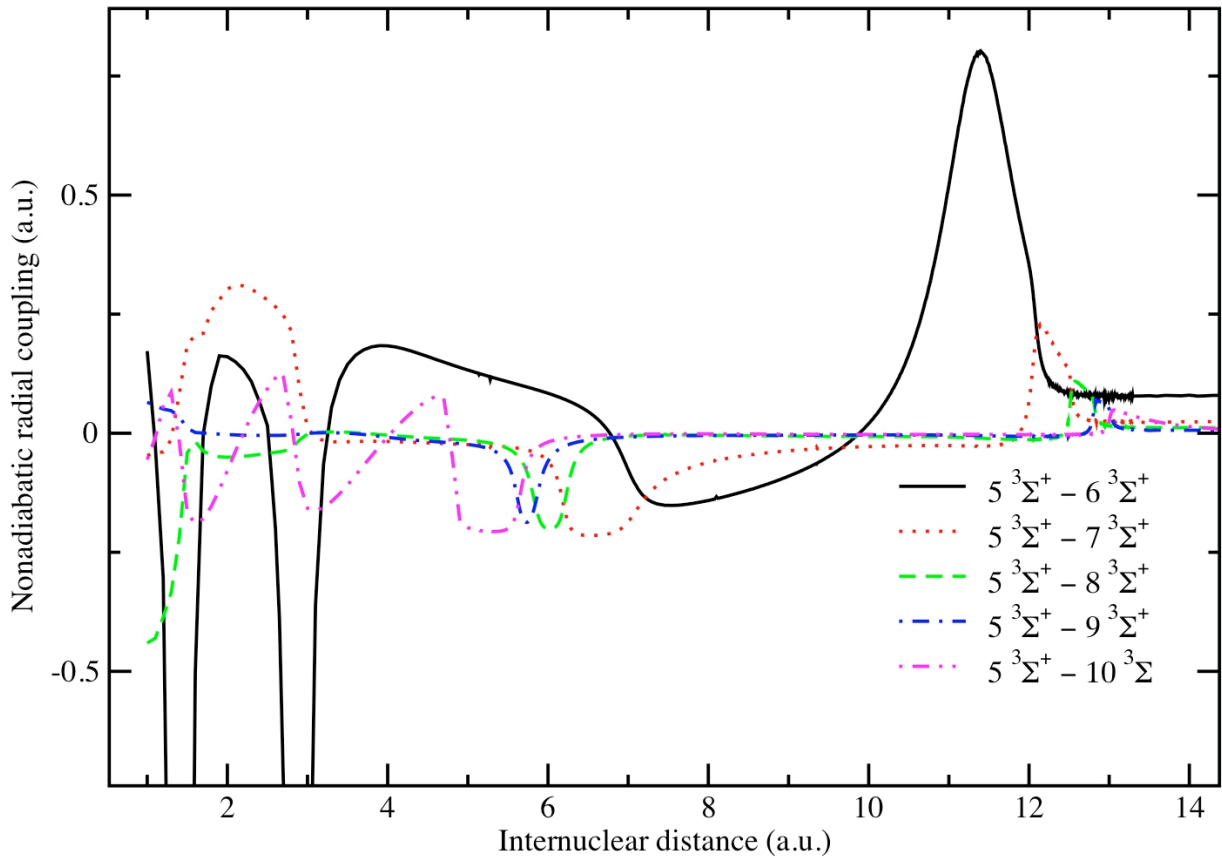


Figure 4.5: Family of ( $5 \ ^3\Sigma^+ - N \ ^3\Sigma^+$ ) nonadiabatic radial couplings for  $\text{O}^{7+} + \text{H}$ .

where the symmetry is preserved in the diabatic basis by only combining adiabatic molecular orbitals of the same symmetry. The adiabatic channel functions likewise transform according to

$$F_i(\mathbf{R}) = \sum_j C_{ij}(R)G_j(\mathbf{R}). \quad (4.6)$$

The expansion coefficients  $C_{ij}$  are elements of the unitary matrix  $\underline{C}(R)$  chosen such that [120]

$$\frac{d}{dR}\underline{C}(R) + \underline{A}(R)\underline{C}(R) = 0, \quad (4.7)$$

where  $\underline{A}(R)$  is the matrix of nonadiabatic radial coupling terms  $A_{ij}(R)$ .

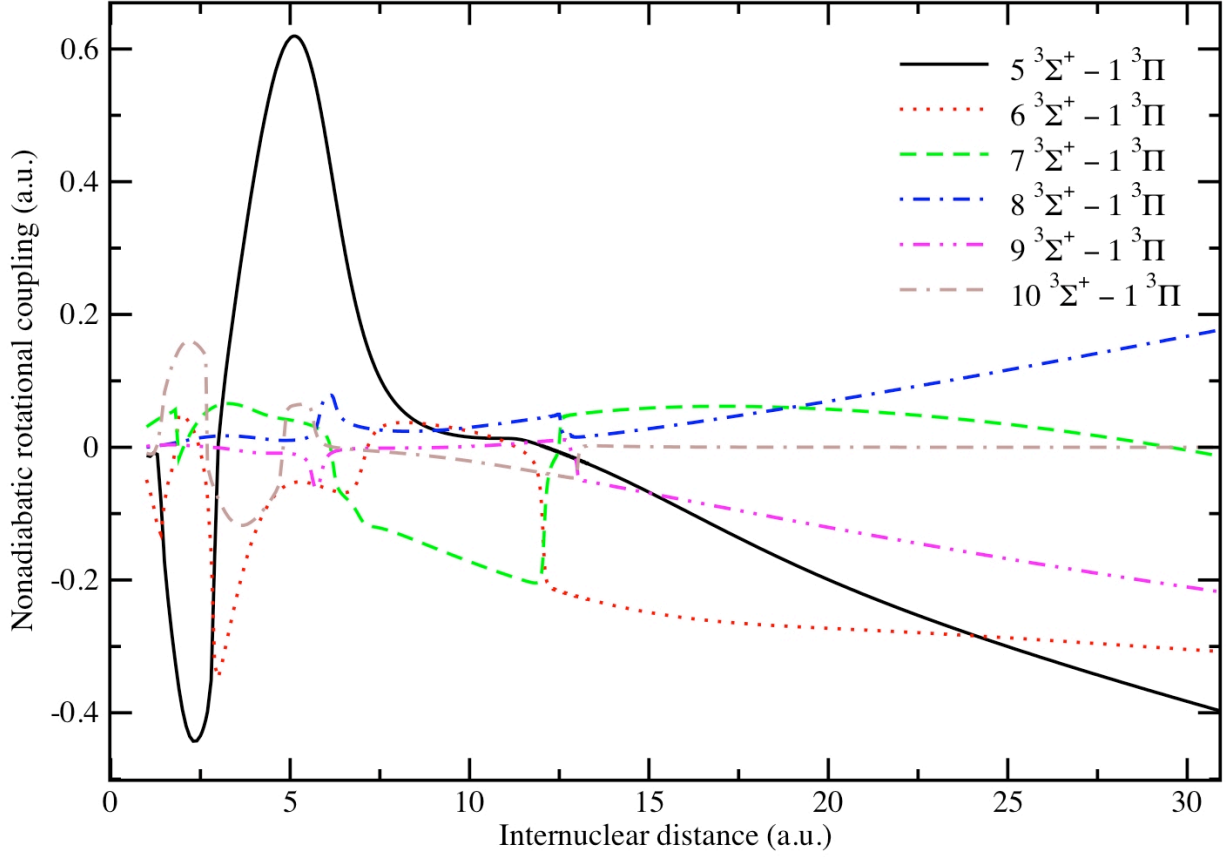


Figure 4.6: Family of ( $N \ ^3\Sigma^+ - 1 \ ^3\Pi$ ) nonadiabatic rotational couplings for  $\text{O}^{7+} + \text{H}$ .

If we introduce a partial wave decomposition of the amplitudes  $G_j(\mathbf{R})$

$$G_j(\mathbf{R}) = \frac{1}{R} \sum_{J,M} g_j^J(R) H_{M,\Lambda_j}^J(\Theta, \Phi), \quad (4.8)$$

where  $H_{M,\Lambda_j}^J$  (which reduces to a spherical harmonic function in the case of  $M = 0$ ) is a function of the polar angles  $\Phi$  and  $\Theta$  of  $\mathbf{R}$  in the space-fixed frame, then the coupled radial equations reduce to the form

$$\left[ \frac{\partial^2}{\partial R^2} + \frac{\Lambda_i^2 - J(J+1)}{R^2} + 2\mu E \right] g_i^J(R) = \sum_j [{}^d V_{ij}^R(R) + {}^d V_{ij}^C(R) + 2\mu U_{ij}(R)] g_j^J(R), \quad (4.9)$$

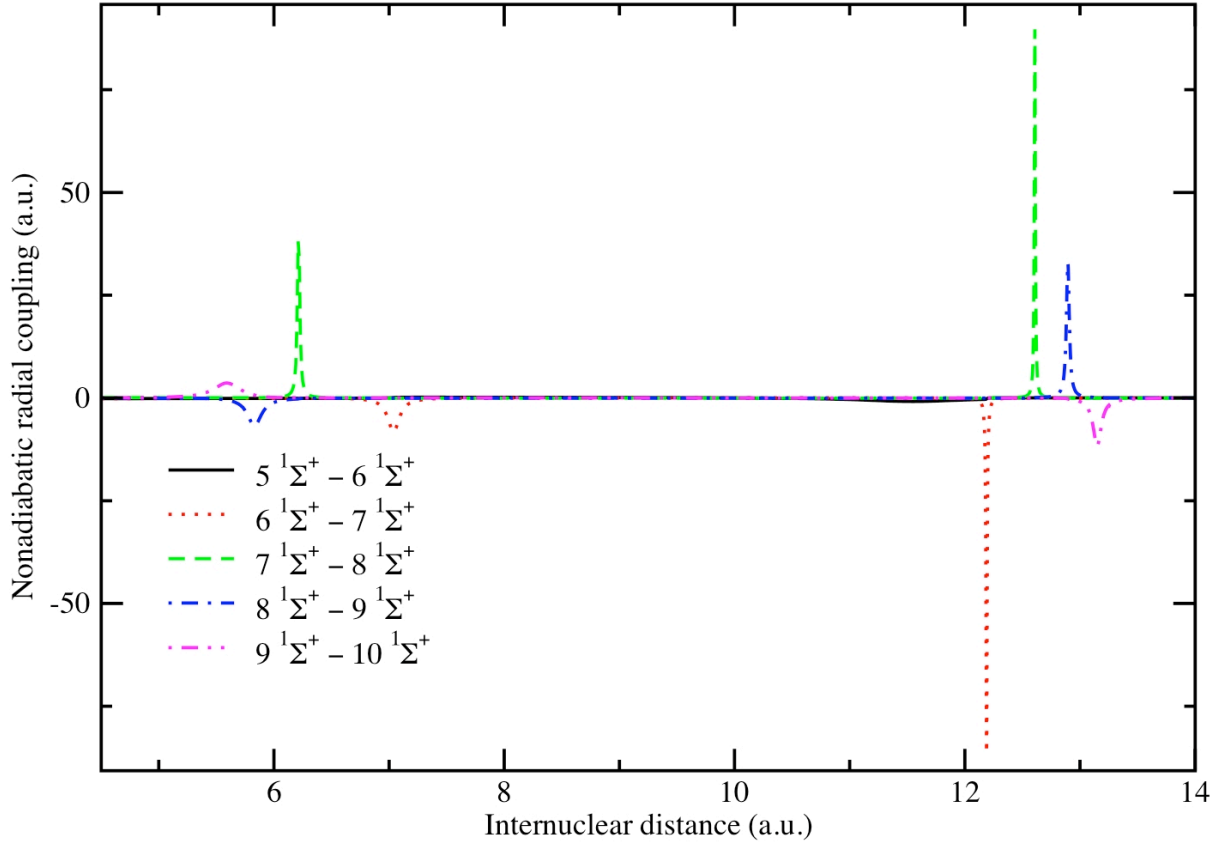


Figure 4.7: Nonadiabatic radial couplings with avoided crossings for adjacent  $n = 5$  singlet channels for  $O^{7+} + H$ .

where

$$U_{ij}(R) = \sum_k C_{ik}^\dagger(R) \epsilon_k(R) C_{kj}(R), \quad (4.10)$$

and  ${}^dV_{ij}^R(R)$  and  ${}^dV_{ij}^C(R)$  are the radial and rotational couplings with respect to the diabatic basis states. The radial coupling takes the same form as in the adiabatic basis, but the rotational coupling may be reduced to

$$\begin{aligned} {}^dV_{ij}^C(R) = & -2\delta_{\Lambda_i, \Lambda_{j+1}} [(J - \Lambda_j)(J + \Lambda_j + 1)]^{1/2} \frac{\langle i^d | iL_y | j^d \rangle}{R^2} \\ & + 2\delta_{\Lambda_i, \Lambda_{j-1}} [(J - \Lambda_j)(J - \Lambda_j + 1)]^{1/2} \frac{\langle i^d | iL_y | j^d \rangle}{R^2}. \end{aligned} \quad (4.11)$$

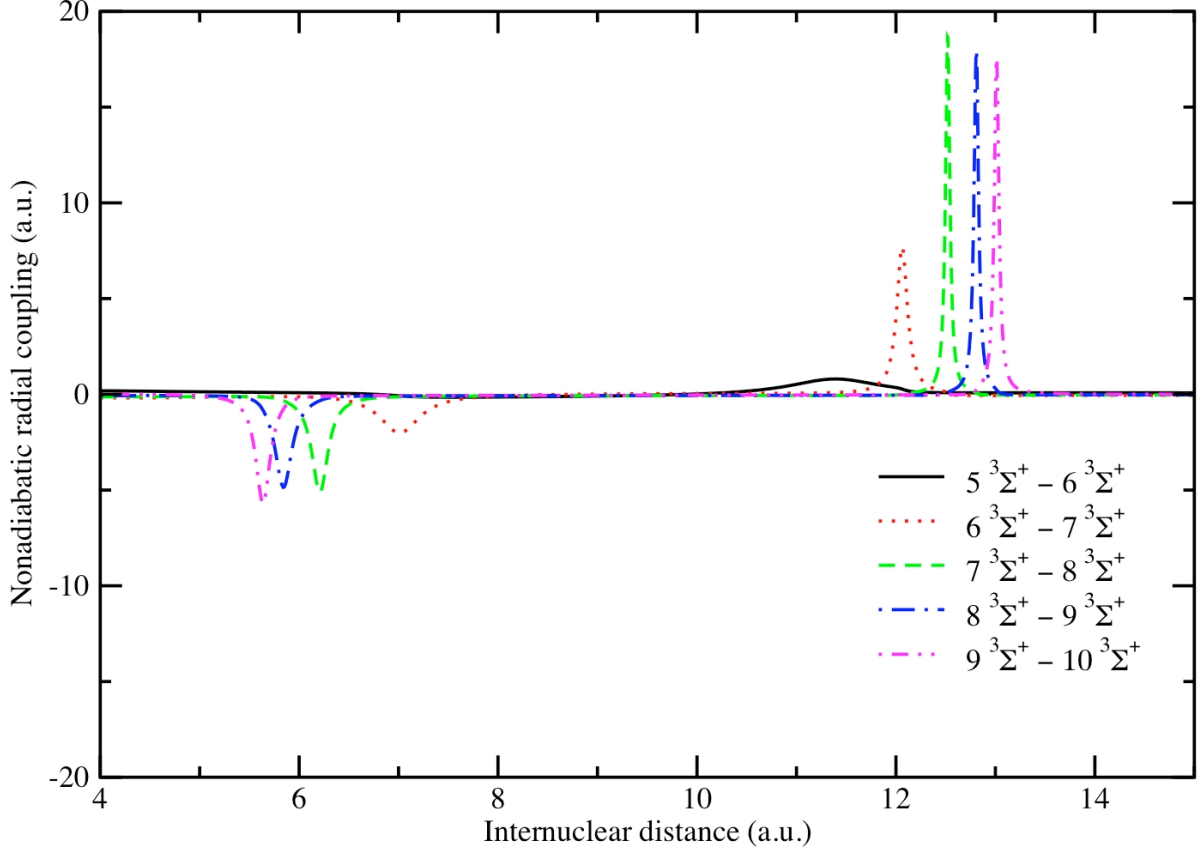


Figure 4.8: Nonadiabatic radial couplings with avoided crossings for adjacent  $n = 5$  triplet channels for  $\text{O}^{7+} + \text{H}$ .

Recasting the coupled equations into matrix form, we have

$$\left[ \frac{\partial^2}{\partial R^2} \underline{I} + \underline{\mathcal{V}}^J(R) \right] \underline{\mathcal{G}}^J(R) = \underline{0}, \quad (4.12)$$

in which the elements of the matrix  $\underline{\mathcal{V}}^J(R)$  are given by

$$\mathcal{V}_{ij}^J(R) = \frac{\Lambda_i^2 - J(J+1)}{R^2} \delta_{ij} + 2\mu(E\delta_{ij} - U_{ij}(R)) - {}^d V_{ij}^R(R) - {}^d V_{ij}^C(R), \quad (4.13)$$

and each column of the square matrix  $\underline{\mathcal{G}}^J(R)$  is a linearly independent solution of Equation (4.9),  $\mathcal{G}_{ij}^J(R)$  being the  $i$ th channel component of the  $j$ th independent solution. The solutions of these equations are obtained using the multichannel log-derivative method of Johnson

[121]. The solutions are subject to the boundary conditions

$$\underline{\mathcal{G}}^J(R) = \underline{\mathcal{J}}^J(R) + \underline{\mathcal{N}}^J(R)\underline{\mathcal{K}}^J, \quad (4.14)$$

in which  $\underline{\mathcal{K}}^J$  is the reaction matrix and

$$\begin{aligned} \mathcal{J}_{ij}^J(R) &= \delta_{ij} k_i^{1/2} R j_J(k_i R) \\ \mathcal{N}_{ij}^J(R) &= \delta_{ij} k_i^{1/2} R n_J(k_i R), \end{aligned} \quad (4.15)$$

where  $j_J(k_i R)$  and  $n_J(k_i R)$  are spherical Bessel functions of the first and second kind for ion-neutral channels, or Coulomb functions of the first and second kind for Coulomb channels. After solving for  $\underline{\mathcal{K}}^J$ , the scattering matrix  $\underline{\mathcal{S}}^J$  is obtained by

$$\underline{\mathcal{S}}^J = [\underline{I} + i\underline{\mathcal{K}}^J][\underline{I} - i\underline{\mathcal{K}}^J]^{-1}, \quad (4.16)$$

and the cross section for an inelastic transition from state  $i$  to  $j$  is

$$\sigma_{ij} = \frac{\pi p_0}{k_i^2} \sum_J (2J+1) |\mathcal{S}_{ij}^J|^2. \quad (4.17)$$

The probability of approach  $p_0$  is related to the total number of molecular states  $g_{ab}$  which can be formed by a target  $a$  and projectile  $b$  with electron spin angular momenta  $S_a$  and  $S_b$ , and electron orbital angular momenta  $L_a$  and  $L_b$ , by

$$p_0 = (2S+1)(2-\delta_{0,\Lambda})/g_{ab}, \quad (4.18)$$

where

$$g_{ab} = (2S_a+1)(2L_a+1)(2S_b+1)(2L_b+1), \quad (4.19)$$

and  $S$  and  $\Lambda$  are the spin and orbital angular momentum projection quantum numbers of the molecular state of approach. For colliding hydrogen-like particles, then, we have  $p_0 = 1/4$  for the initial singlet channel and  $p_0 = 3/4$  for the initial triplet channel.

### 4.3 RESULTS

Cross sections were obtained using the MOCC methods outlined in the previous section. For the MOCC calculations, the number of partial waves and asymptotic matching distance were tested for convergence, and state-to-state cross sections were obtained by summing over partial cross sections as in Equation (4.17).

In Figure 4.9 we show the  $n, l$ -resolved cross sections of the MOCC calculations. It is clear that the  $n = 5$  manifold is the dominant path for charge exchange over the entire energy range, with  $5p$  dominating at collision energies below about 2 eV/u, and  $5s$  dominating above. This is consistent with the prediction of the COB model, in which the dominant  $n$ -channel is approximated as the largest value satisfying the inequality [122]

$$n_{max} \leq q \left[ 2|I_Y| \left( 1 + \frac{q-1}{2\sqrt{q}+1} \right) \right]^{-1/2}, \quad (4.20)$$

where  $q$  is the charge of the incident ion and  $I_Y$  (in a.u.) is the ionization potential of the target. The rather sharp drop-off of the  $n = 4$  channels below about 10 eV/u occurs as the collision energy falls below that of the nearest approach of the  $5s$  singlet and triplet channels to the  $n = 4$  channels at around  $R = 5$  a.u. The  $4s$  channel unsurprisingly makes the smallest contribution to the total cross section over almost the entire energy range; in both the singlet and triplet manifolds, the  $4s$  potential curve does not approach the other curves of the  $n = 4$  manifold for energies  $< 1 - 2$  a.u. higher than the asymptotic energy of the entrance channel (see Figures 4.1 - 4.4).

These trends are reflected in the  $n, l, S$ -resolved cross sections shown in Figures 4.10 and 4.11. At energies greater than 40 eV/u, the  $5f$  becomes the dominant singlet capture state, but due to the relative magnitude of singlet and triplet cross sections this dominance is not reflected in the total cross section. The dominance of  $5s$  for both singlets and triplets at intermediate to large collision energies seems reasonable; as the collision energy increases, a greater portion of the avoided crossing between the  $5s$  and adjacent  $n = 5$  state becomes classically accessible, allowing for increased flux into this channel.

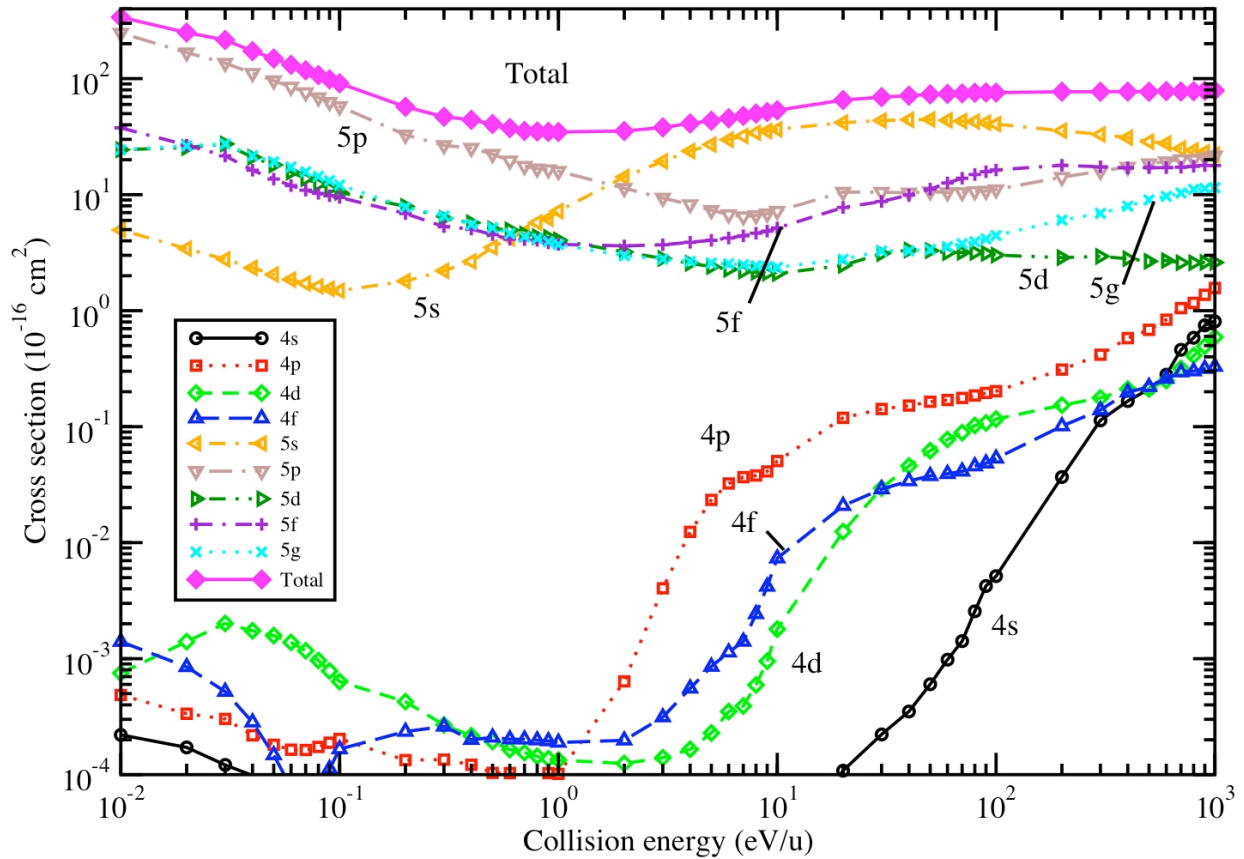


Figure 4.9: Total  $n, l$ -resolved MOCC cross sections for  $O^{7+} + H$ .

Triplet-singlet ratios for each of the  $n, l$  capture states are displayed in Figure 4.12. As mentioned in Section 4.1, the triplet-singlet ratio is expected to exhibit velocity dependence at low collision energies, approaching a statistical distribution only around 10 keV/u. The triplet-singlet distribution for each  $n, l$ -state is seen to vary widely over the range of collision energies, with only a few seeming to approach 3:1 at higher energies. The large drop in the  $4p$  ratio over the 1-100 eV/u range may arise from the avoided crossing between the singlet  $4p$  and  $5s$  states which becomes accessible at higher collision energies, while in the triplet

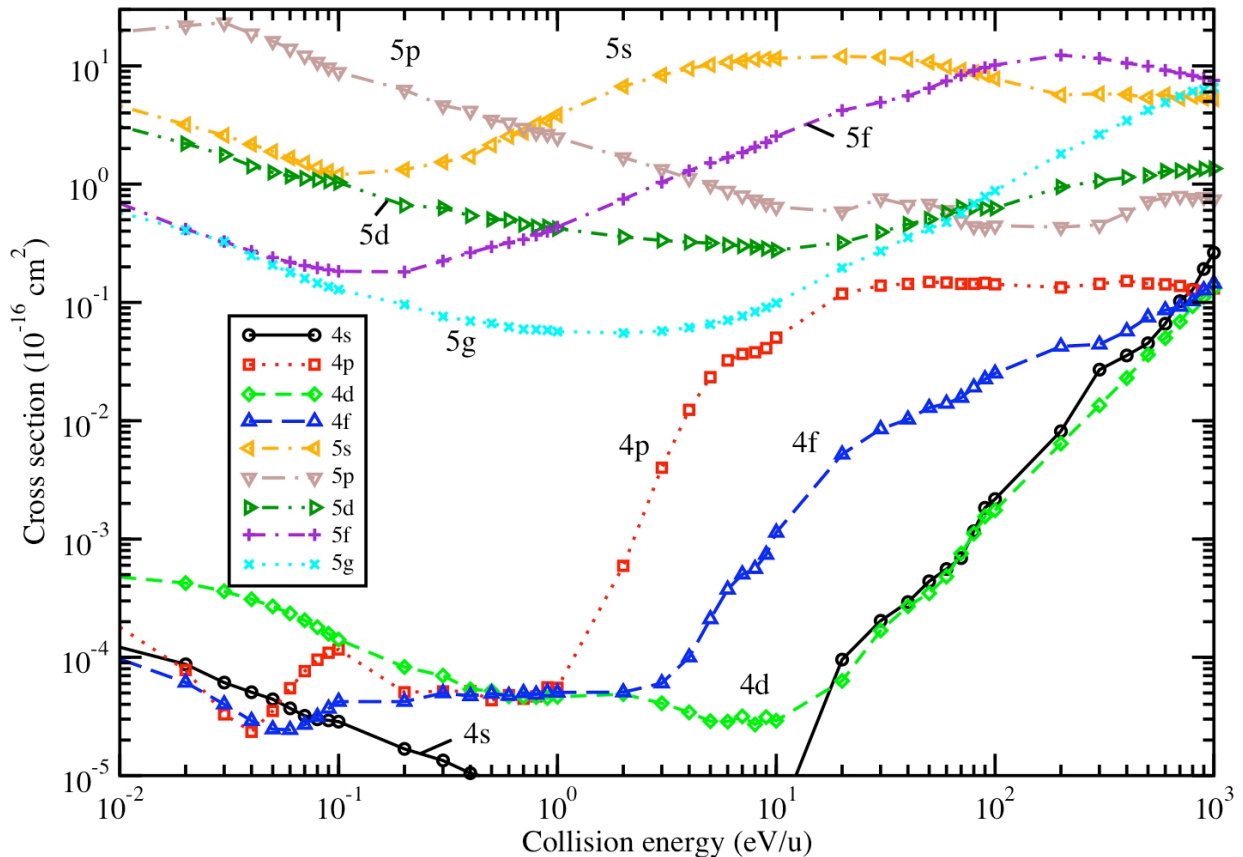


Figure 4.10: Singlet  $n, l$ -resolved MOCC cross sections for  $O^{7+}+H$ .

manifold the  $4p$  state does not appear to share any significant avoided crossing with its adjacent  $n = 4$  states.

In Figure 4.13 we plot total MOCC cross sections as well as those obtained by the AOCC and CTMC methods (supplied by D. R. Schultz and Y. Hui in a private communication [123]), along with previous fits and experimental results [124, 125, 22, 23, 24]. For the MOCC calculations, cross sections computed with and without states of  $\Pi$  symmetry are shown, the latter neglecting rotational coupling. Below about 1 eV/u, the two calculations are in close agreement, illustrating the negligible effect of rotational couplings at low energies. At about

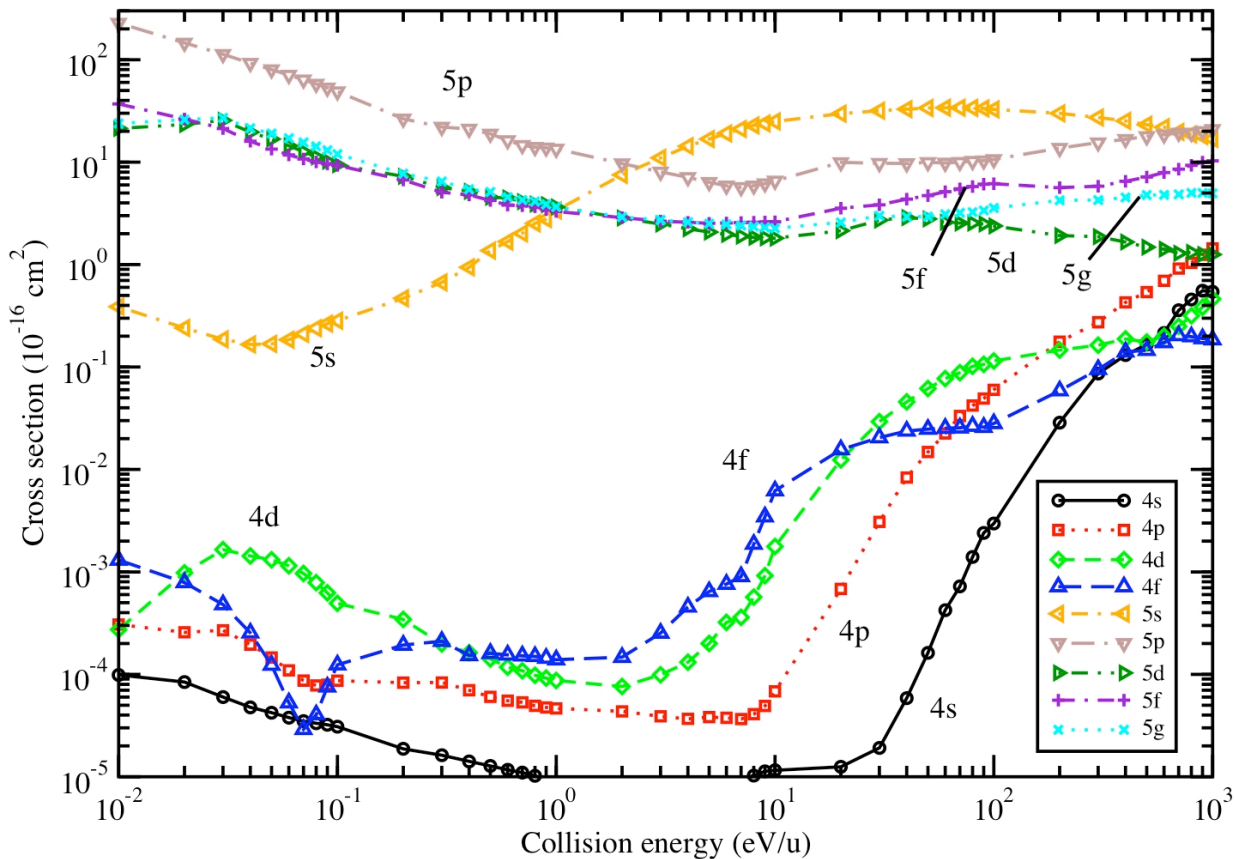


Figure 4.11: Triplet  $n, l$ -resolved MOCC cross sections for  $O^{7+}+H$ .

1 eV/u the cross sections begin to diverge, with the all-states calculation exceeding AOCC and experimental values by a factor of  $\sim 1.5$  at the highest energies while the  $\Sigma$ -states (radial coupling only) calculations appear to follow the trends of the other available data, although there is some overlap between the MOCC all-states and AOCC calculations at around 100 eV/u. As the inclusion of  $\Pi$  states entails roughly a doubling of the number of couplings included in the calculation, this indicates that discrepancies at energies greater than  $\sim 10$  eV/u may be partly due to uncertainties in the MRDCI couplings. For instance, it is a shortcoming of the MRDCI computational method that the absolute phases of the couplings

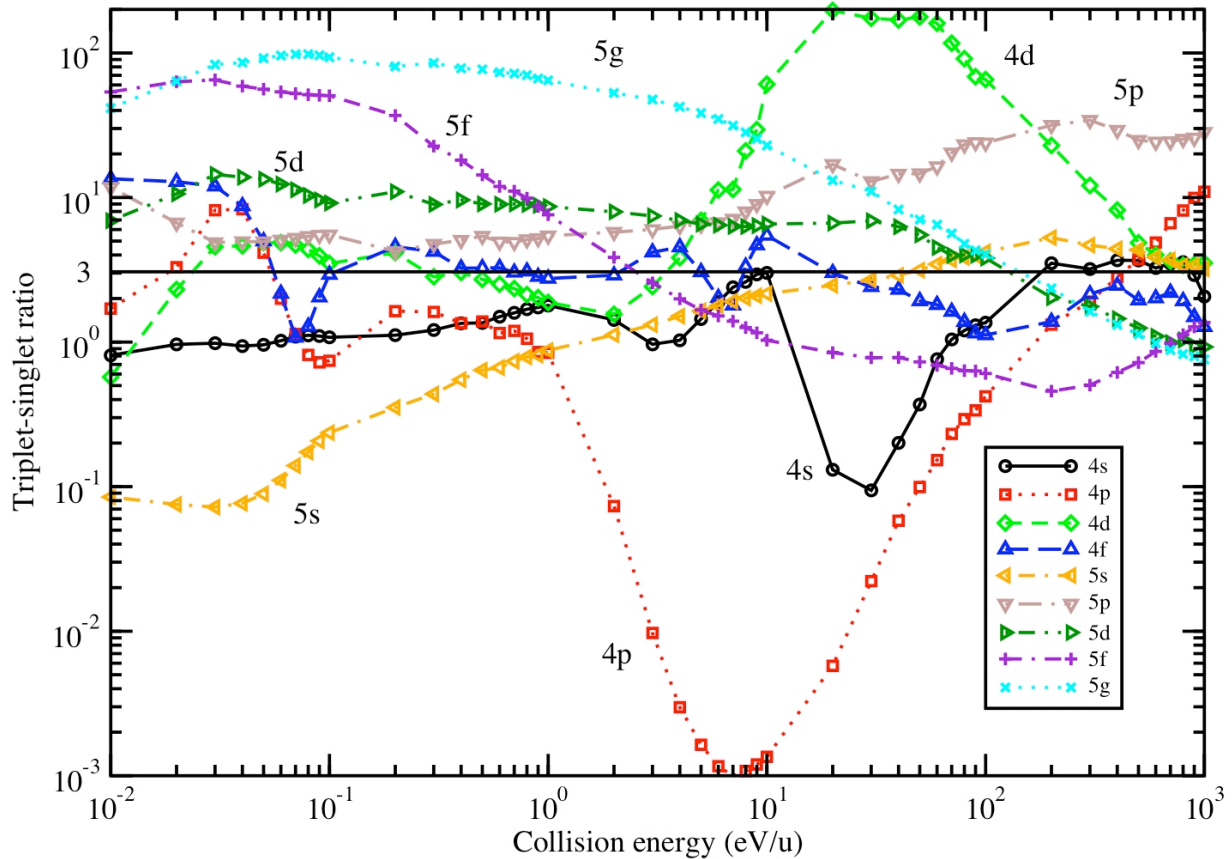


Figure 4.12: Triplet-singlet ratios for  $n, l$ -resolved cross sections for  $O^{7+} + H$ .

for each value of  $R$  are determined arbitrarily, so that relative phases must be determined by comparison with other couplings, a process which allows for many uncertainties. We suspect, however, that the main source of error may lie in the size of our basis set, particularly in our neglect of capture into the  $n \geq 6$  manifolds (see below). For energies below 100 eV/u, both sets of MOCC results exceed the recent experimental results of Havener et al. [22] by up to a factor of  $\sim 2.5$ . Similar discrepancies at low energy between MOCC and experiment have been found for  $Cl^{7+} + H$  [126],  $N^{6+} + H$  [116], and other systems. Other sources of error in the MOCC calculations may be due to the neglect of electron translation factors and ionization, but these are expected to only be important for energies greater than 1

keV/u. (See Wu et al. [116] for further discussion on possible theoretical and experimental uncertainty.) The CTMC method, which is valid only for higher energies, not unexpectedly underestimates the total cross section at energies below  $10^5$  eV/u.

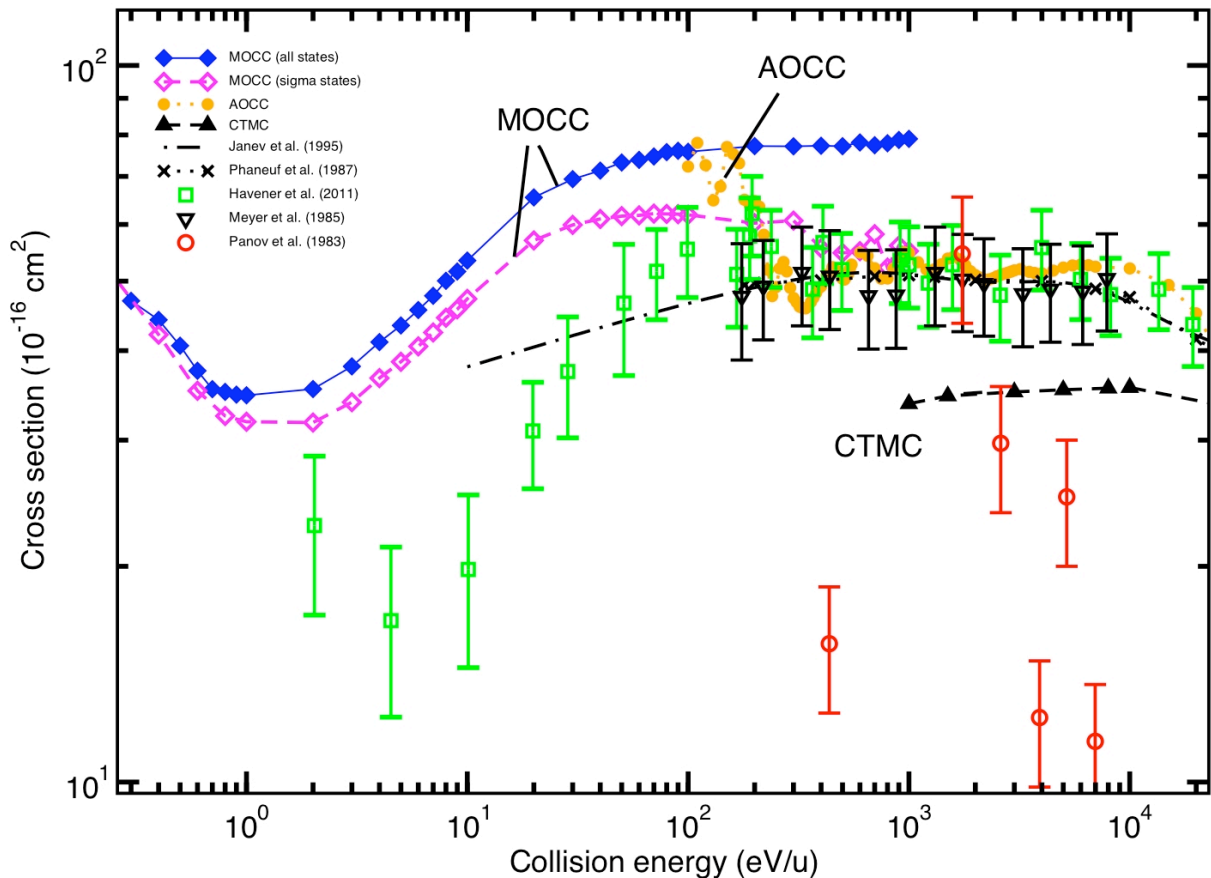


Figure 4.13: Comparison of total cross sections for  $O^{7+}+H$  using MOCC, as well as AOCC and CTMC [123] methods. Also included are fits by Janev et al. (1995) [124] and Phaneuf et al. (1987) [125], as well as experimental results of Havener et al. (2011) [22], Meyer et al. (1985) [23], and Panov et al. (1983)[24].

Referring to the plot of  $n$ -resolved cross sections in Figure 4.14, we again find fair agreement between AOCC and MOCC calculations in the overlapping energy range of  $10^2$  to  $10^3$  eV/u, and good agreement between AOCC and CTMC for most  $n$  levels for energies greater than about  $5 \times 10^4$  eV/u. The only state-resolved experimental information for this collision system are the relative translation energy spectroscopy (TES) measurements of Kearns et

al. [25]. The TES measurements, MOCC and AOCC are all in agreement that the dominant channel is  $n = 5$ , followed by  $n = 4$ . However, we also find the data from AOCC and Kearns et al. showing  $n = 6$  capture comparable to that of  $n = 4$  for MOCC, suggesting that this and possibly other  $n$  channels may make important contributions to the total cross section at high energies. Normalizing the TES results to the absolute magnitude of Meyer et al. [23], the AOCC results are in slightly better agreement for  $n = 5$  and 4, but overestimate  $n = 6$  for  $E \leq 500$  eV/u. On the other hand, CTMC finds the  $n = 4$  cross section to be slightly larger than  $n = 5$  at 10 keV/u.

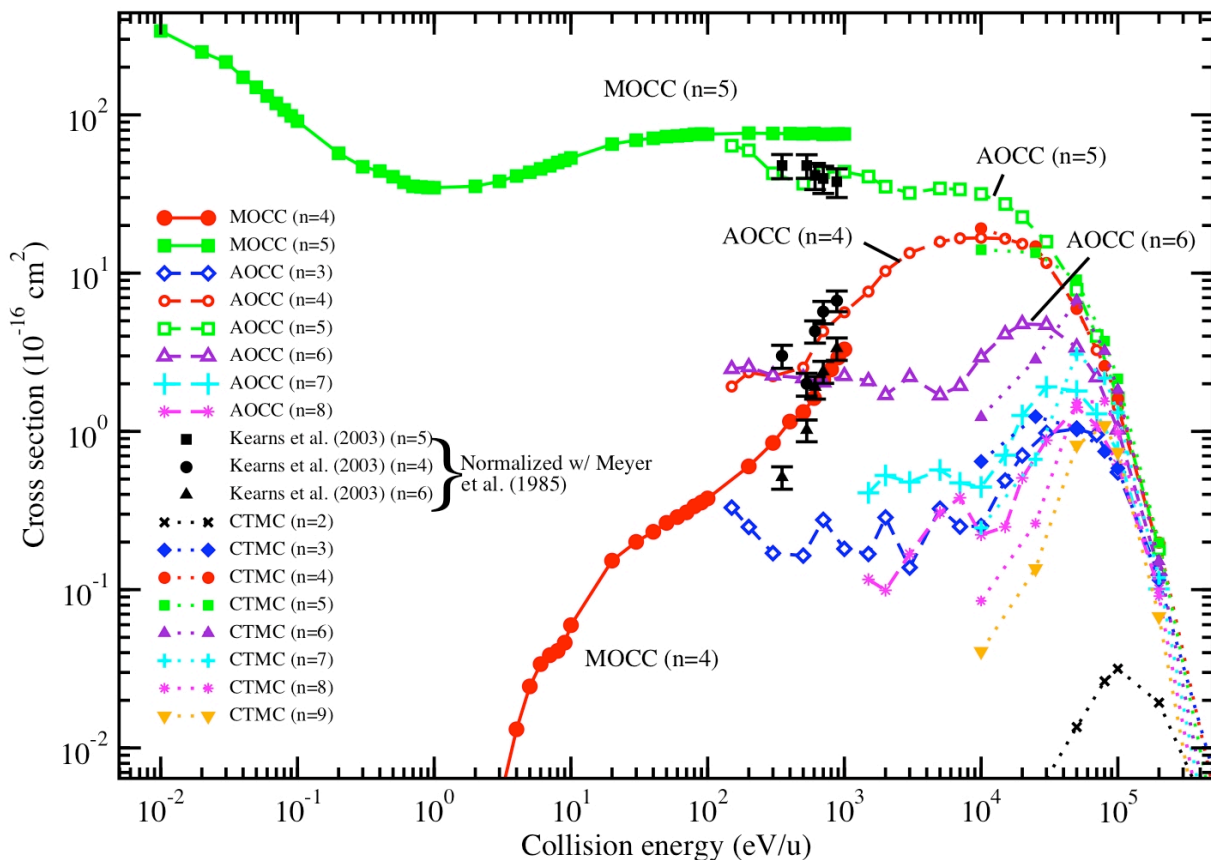


Figure 4.14: Comparison of  $n$ -resolved cross sections for  $O^{7+}+H$  for MOCC, AOCC, CTMC calculations and experimental results of Kearns et al. (2003) [25].

In Figures 4.15 and 4.16, we show comparisons of the  $l$ -distribution of capture states for  $n = 5$  for each of the theoretical methods, along with the statistical and low-energy

distributions, for  $E = 300$  and  $1000$  eV/u. It is well known that for energies greater than about  $10$  keV/u the  $l$ -distribution should approach the statistical distribution

$$W_{nl}^{st} = (2l + 1)/n^2, \quad (4.21)$$

while for low energies a plausible distribution function is given by [127]

$$W_{nl}^{le} = (2l + 1) \frac{[(n - 1)!]^2}{(n + 1)!(n - 1 - l)!}. \quad (4.22)$$

For increasing energy we find the AOCC and CTMC results in increasing agreement with the statistical distribution, as we would expect. In Figure 4.17, we have plotted a comparison of MOCC  $l$ -distributions at lower energies with the low-energy distribution of Equation (4.22). While the MOCC distributions show a rough similarity to the trend of the low-energy distribution for  $E = 0.01$  and  $1$  eV/u, at  $10$  eV/u and higher the distributions are quite different. See Appendix A for detailed comparisons of the MOCC, AOCC, and CTMC cross sections as a function of energy at the  $n, l$ -level.

A recommended fit to the  $n, l$ -resolved cross sections for the  $O^{7+} + H$  collision system would follow the current MOCC results up to energies between  $10^2$  and  $10^3$  eV/u, with AOCC results representing the intermediate regime up to about  $10^5$  eV/u, and CTMC results being used for all higher energies. Triplet-singlet ratios for each  $n, l$  state should follow MOCC values up to  $1$  keV/u, with linear extrapolations beyond this point to approach a value of 3:1 at around  $10$  keV/u.

#### 4.4 CONCLUSIONS

We have reported  $l$ - and  $S$ -resolved cross sections for single electron capture into the dominant  $n = 4$  and  $5$  manifolds over the energy range  $10^{-2}$  to  $10^3$  eV/u, using the fully quantal MOCC method. For higher energies the semiclassical AOCC and quasi-classical CTMC methods were used. Agreement between MOCC and AOCC results in the overlapping energy range is fair, and MOCC results may be recommended for energies below  $10^2$  to  $10^3$  eV/u, with AOCC and CTMC results serving as the basis for fits to cross sections at

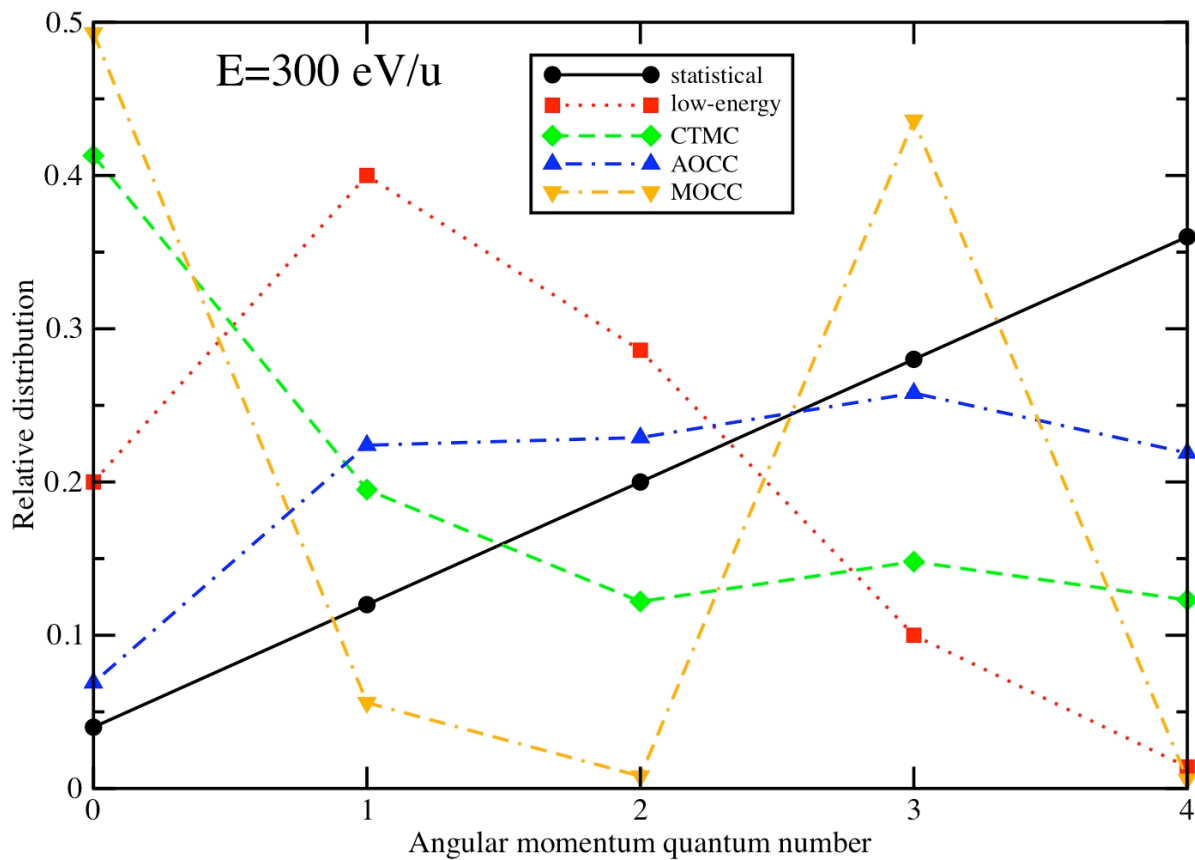


Figure 4.15: Comparison of  $n = 5$   $l$ -distributions for  $O^{7+} + H$  for MOCC, AOCC and CTMC, along with statistical and low-energy distributions at  $E = 300$  eV/u.

higher energies. Triplet-singlet ratios, which are only available for the MOCC data, may be extrapolated to approach a 3:1 ratio at higher energies.

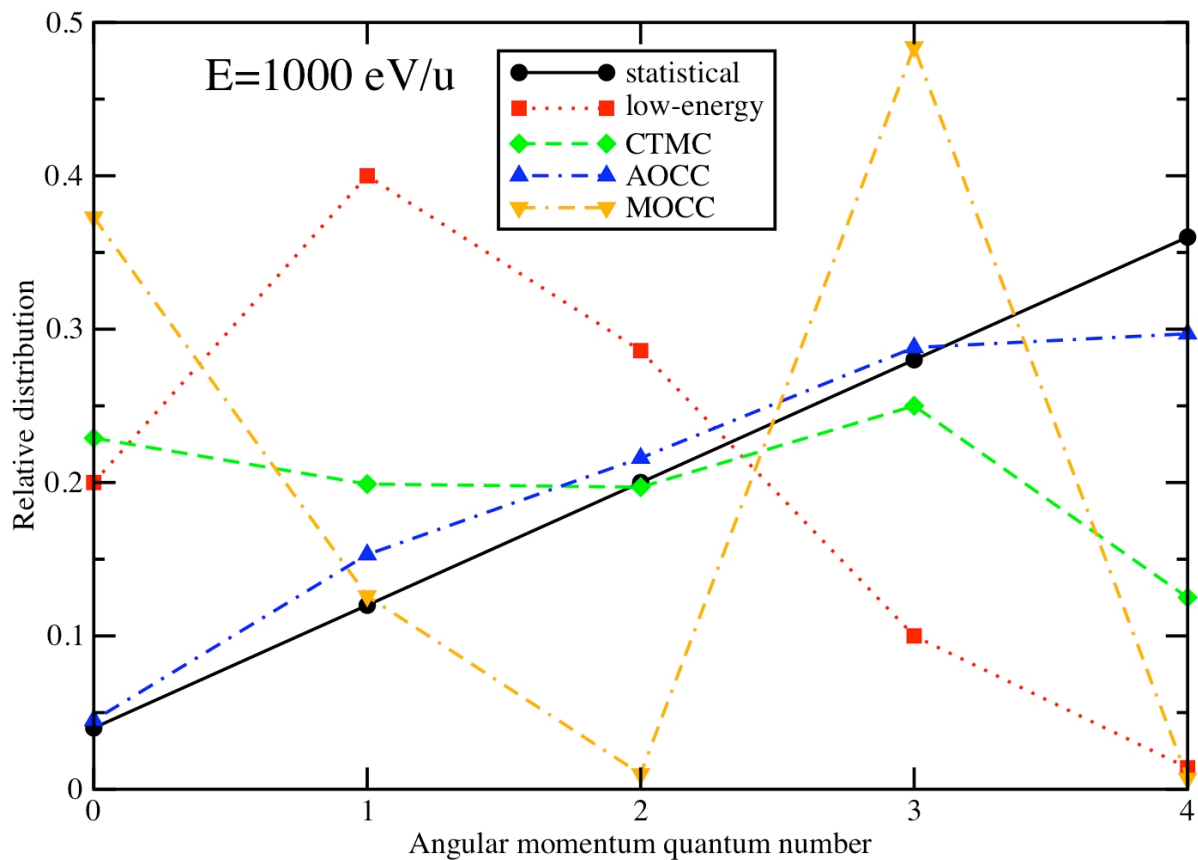


Figure 4.16: Comparison of  $n = 5$   $l$ -distributions for  $O^{7+} + H$  for MOCC, AOCC and CTMC, along with statistical and low-energy distributions at  $E = 1000$  eV/u.

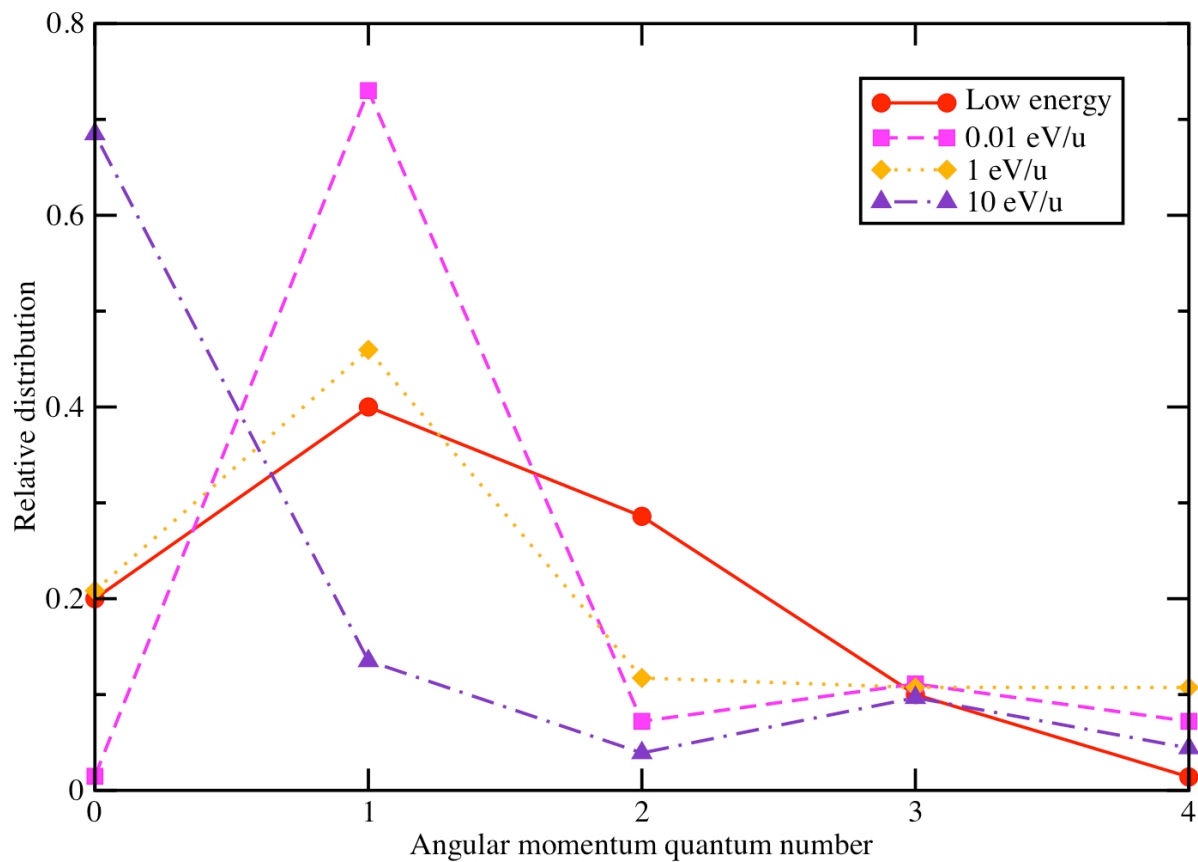


Figure 4.17: Comparison of MOCC  $n = 5$   $l$ -distributions for  $O^{7+} + H$  to low-energy distribution at different energies.

## CHAPTER 5

### FINAL-STATE RESOLVED CHARGE EXCHANGE BETWEEN $C^{5+}$ AND $H^1$

---

<sup>1</sup>Based on J. L. Nolte, P. C. Stancil, H.-P. Liebermann, R. J. Buenker, D. R. Schultz, Y. Hui, I. N. Draganić, and C. C. Havener. To be submitted to Phys. Rev. A.

## ABSTRACT

Charge exchange cross sections are calculated for the collision system  $C^{5+} + H$  using the quantal molecular orbital close-coupling method. Calculations are performed over a range of collision energies from 0.01 eV/u to 1 keV/u for all important  $n$ ,  $l$ , and  $S$ -resolved states. In particular, we focus on the distribution of electron capture into the  $n=3$ , 4 and 5 manifolds, for both singlet and triplet states. We compare our results to new atomic orbital close-coupling, classical trajectory Monte Carlo, and experimental merged-beams results.

### 5.1 INTRODUCTION

We here extend the MOCC method of charge exchange calculations to another collision system of relevance to x-ray emission in the Solar System, namely  $C^{5+} + H$ . As stated in the previous chapter, highly charged C and O are the dominant solar wind contributors to x-ray emission in the solar system, due to their high abundance. While the contribution of these species to diffuse soft x-ray emission is dominated by O VII, O VIII, and C VI emission lines [11, 12, 13, 14, 15, 100, 128], C V emission from the  $K\alpha$  complex consisting of the forbidden, intercombination, and resonance lines is a prominent feature around 300 eV, and was even found to be a dominant presence in recent *Chandra* observations of Comet 8P/Tuttle [129]. As with the  $O^{7+} + H$  system, experimental  $l$ - and  $S$ -resolved charge exchange cross sections for  $C^{5+} + H$  are completely lacking, with the only  $n$ -resolved measurement to our knowledge being that of the relative cross sections for  $n = 3, 4$ , and 5 at a single collision energy by Kearns et al. [25].

In this work, we again calculate charge exchange cross sections over a range of low to intermediate collision energies and compare to available theoretical and experimental data.

### 5.2 COMPUTATIONAL DETAILS

Adiabatic potentials and nonadiabatic couplings were again obtained with the MRDCI approach, in calculations by Liebermann and Buenker [130]. In our scattering calculations

we utilize nine  $^1\Sigma^+$  and nine  $^3\Sigma^+$  electronic states in  $A_1$  symmetry, and five  $^1\Pi$  and five  $^3\Pi$  states in  $B_1$  symmetry calculated for internuclear distances between 2.1 and 20 a.u. These states comprise all  $n = 3$  and 4 states as well as the lowest  $n = 5$  state ( $5s$  for both singlets and triplets), which we have included to represent capture into the  $n = 5$  manifold. In Table 5.2 we show absolute and relative asymptotic energies with respect to the  $C^{5+}(1s) + H(1s)$  entrance channel, for both this calculation and experimental atomic spectroscopic data [118], and find generally good agreement, the largest error in relative asymptotic energies being about 0.015 a.u.

In Figures 5.1 - 5.4 we show adiabatic potential energy curves for all channels used in the calculation, and representative families of nonadiabatic radial and rotational couplings are shown in Figures 5.5 and 5.6. Figures 5.7 and 5.8 illustrate nonadiabatic radial couplings for adjacent  $n = 4$  and entrance channels, characterized by sharp peaks at the avoided crossings.

Cross sections are calculated over a collision energy range of  $10^{-2}$  to  $10^3$  eV/u, where convergence with respect to calculation parameters such as number of partial waves and asymptotic matching distance has been ensured.

### 5.3 RESULTS

Total  $n, l$ -resolved cross sections are shown in Figure 5.9. The  $n = 4$  channels, which together with the entrance channel exhibit a series of avoided crossings in the 12-15 a.u. separation range, form the dominant manifold for charge exchange as expected. The  $4s$  channel in particular is seen to dominate across the entire energy range up to 1 keV/u. For low energies,  $n = 3$  channels receive the next largest share of flux, but at 7 eV/u electron capture into the  $n = 5$  manifold, represented here by the inclusion of the single  $5s$  state, increases sharply and at the highest energies even surpasses capture to  $4f$ .

Similar trends may be seen in the  $S$ -resolved cross sections shown in Figures 5.10 and 5.11. The  $4s$  channel is dominant for both singlets and triplets across the entire energy range, as in both cases it has the widest avoided crossing with its adjacent  $n = 4$  state, and an

Table 5.1: Comparison of asymptotic separated-atom energies (in a.u., where 1 a.u. = 1 hartree) between MRDCI calculations and experimental NIST data [118] for  $C^{5+} + H$ .  $\Delta E_{calc}$  is the energy separation of the asymptotic atomic state from the initial state  $C^{5+}(1s) + H(1s)$  in the MRDCI calculations.  $\Delta E_{exp}$  is the same quantity for the experimental values.  $\Delta E = |\Delta E_{exp} - \Delta E_{calc}|$ .

Asymptotic atomic state	Mol. state	This work	Expt. [118]	$\Delta E_{calc}$	$\Delta E_{exp}$	$\Delta E$
Singlets						
$C^{4+}(1s3s \ ^1S) + H^+$	$1 \ ^1\Sigma^+$	-19.41786	-19.42497	0.91806	0.91833	0.00027
$C^{4+}(1s3d \ ^1D) + H^+$	$2 \ ^1\Sigma^+$	-19.38903	-19.39603	0.88923	0.88939	0.00016
	$1 \ ^1\Pi$	-19.38876	-19.39603	0.88896	0.88939	0.00043
$C^{4+}(1s3p \ ^1P^o) + H^+$	$3 \ ^1\Sigma^+$	-19.37933	-19.38766	0.87953	0.88102	0.00149
	$2 \ ^1\Pi$	-19.37933	-19.38766	0.87953	0.88102	0.00149
$C^{4+}(1s4s \ ^1S) + H^+$	$4 \ ^1\Sigma^+$	-18.79662	-18.80045	0.29682	0.29381	0.00301
$C^{4+}(1s4d \ ^1D) + H^+$	$3 \ ^1\Pi$	-18.78641	-18.78822	0.28661	0.28158	0.00503
	$5 \ ^1\Sigma^+$	-18.78639	-18.78822	0.28659	0.28158	0.00501
$C^{4+}(1s4f \ ^1F^o) + H^+$	$4 \ ^1\Pi$	-18.77899	-18.78825	0.27919	0.28161	0.00242
	$6 \ ^1\Sigma^+$	-18.77879	-18.78825	0.27899	0.28161	0.00262
$C^{4+}(1s4p \ ^1P^o) + H^+$	$5 \ ^1\Pi$	-18.77337	-18.78488	0.27357	0.27824	0.00467
	$7 \ ^1\Sigma^+$	-18.77261	-18.78488	0.27281	0.27824	0.00543
$C^{4+}(1s5s \ ^1S) + H^+$	$8 \ ^1\Sigma^+$	-18.52159	-18.51324	0.02179	0.00660	0.01519
$C^{5+}(1s) + H(1s)$	$9 \ ^1\Sigma^+$	-18.49980	-18.50664	0	0	0
Triplets						
$C^{4+}(1s3s \ ^3S) + H^+$	$1 \ ^3\Sigma^+$	-19.47045	-19.47785	0.97065	0.97121	0.00056
$C^{4+}(1s3p \ ^3P^o) + H^+$	$2 \ ^3\Sigma^+$	-19.41691	-19.42384	0.91711	0.91720	0.00009
	$1 \ ^3\Pi$	-19.41656	-19.42384	0.91676	0.91720	0.00044
$C^{4+}(1s3d \ ^3D) + H^+$	$3 \ ^3\Sigma^+$	-19.38912	-19.39703	0.88932	0.89039	0.00107
	$2 \ ^3\Pi$	-19.38909	-19.39703	0.88929	0.89039	0.00110
$C^{4+}(1s4s \ ^3S) + H^+$	$4 \ ^3\Sigma^+$	-18.81670	-18.82187	0.31690	0.31523	0.00167
$C^{4+}(1s4p \ ^3P^o) + H^+$	$5 \ ^3\Sigma^+$	-18.79425	-18.79989	0.29445	0.29325	0.00120
	$3 \ ^3\Pi$	-18.79385	-18.79989	0.29405	0.29325	0.00080
$C^{4+}(1s4d \ ^3D) + H^+$	$6 \ ^3\Sigma^+$	-18.78389	-18.78886	0.28409	0.28222	0.00187
	$4 \ ^3\Pi$	-18.78383	-18.78886	0.28403	0.28222	0.00181
$C^{4+}(1s4f \ ^3F^o) + H^+$	$5 \ ^3\Pi^+$	-18.77706	-18.78822	0.27726	0.28158	0.00432
	$7 \ ^3\Sigma^+$	-18.77684	-18.78822	0.27704	0.28158	0.00454
$C^{4+}(1s5s \ ^3S) + H^+$	$8 \ ^3\Sigma^+$	-18.52711	-18.52394	0.02731	0.01730	0.01001
$C^{5+}(1s) + H(1s)$	$9 \ ^3\Sigma^+$	-18.49980	-18.50664	0	0	0

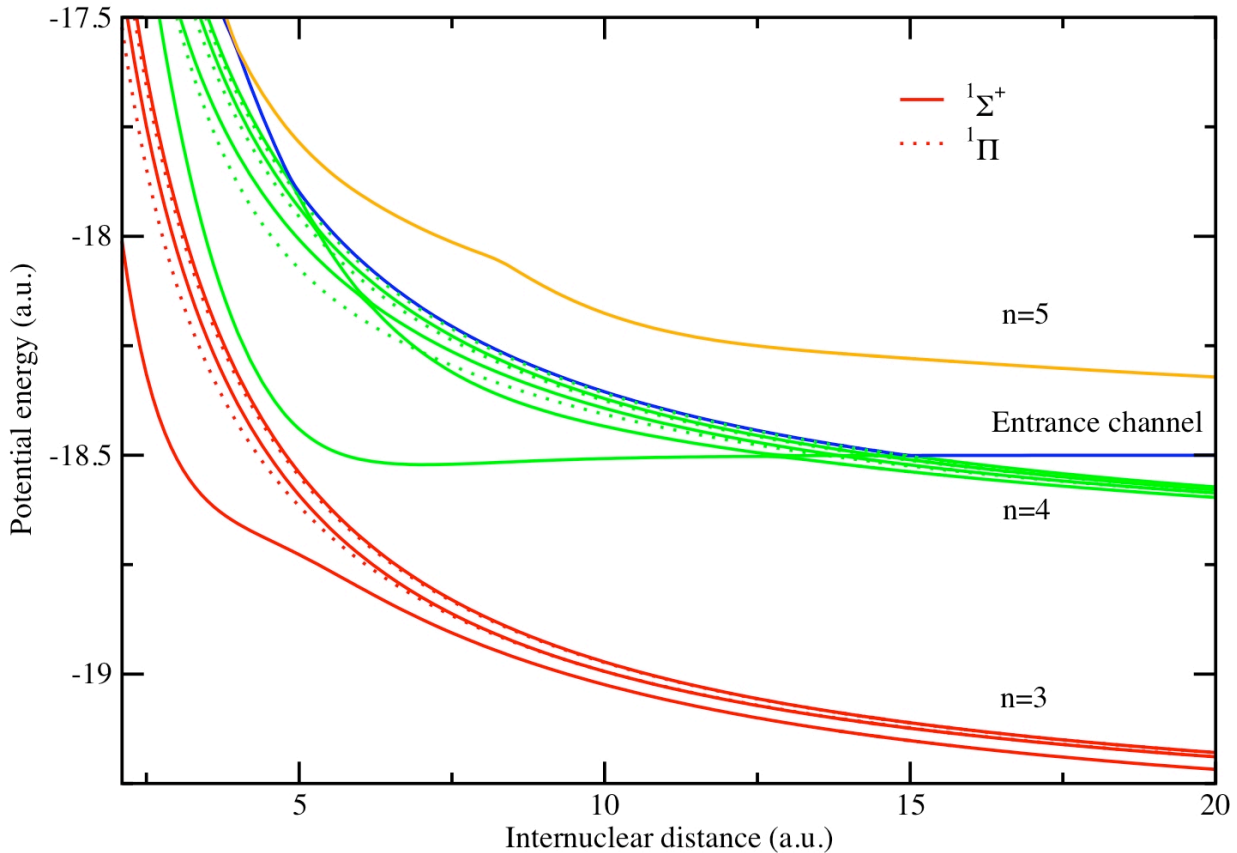


Figure 5.1: Singlet adiabatic potentials for  $C^{5+} + H$ .

avoided crossing with the adjacent  $n = 3$  state only at  $R < 5$  (See Figures 5.1 - 5.4). In both cases the  $n = 3$  channels exhibit a gradual increase for energies greater than  $\sim 10$  eV/u as the avoided crossing between the  $4s$  channel and the  $n = 3$  manifold becomes more energetically accessible. The sharp increase in both cases of the  $5s$  channel around 7-10 eV/u is somewhat surprising. This may, however, be largely due to the very broad approach of the  $5s$  to the entrance channel which may be seen to occur in the neighborhood of 10 a.u. The fact that we find  $5s$  capture making contributions comparable to  $n = 4$  channels at the highest energies reinforces our suggestion in the previous chapter that neglect of higher  $n$  states may not be justified. Shimakura et al. [26] calculated  $n, l, S$ -resolved cross sections

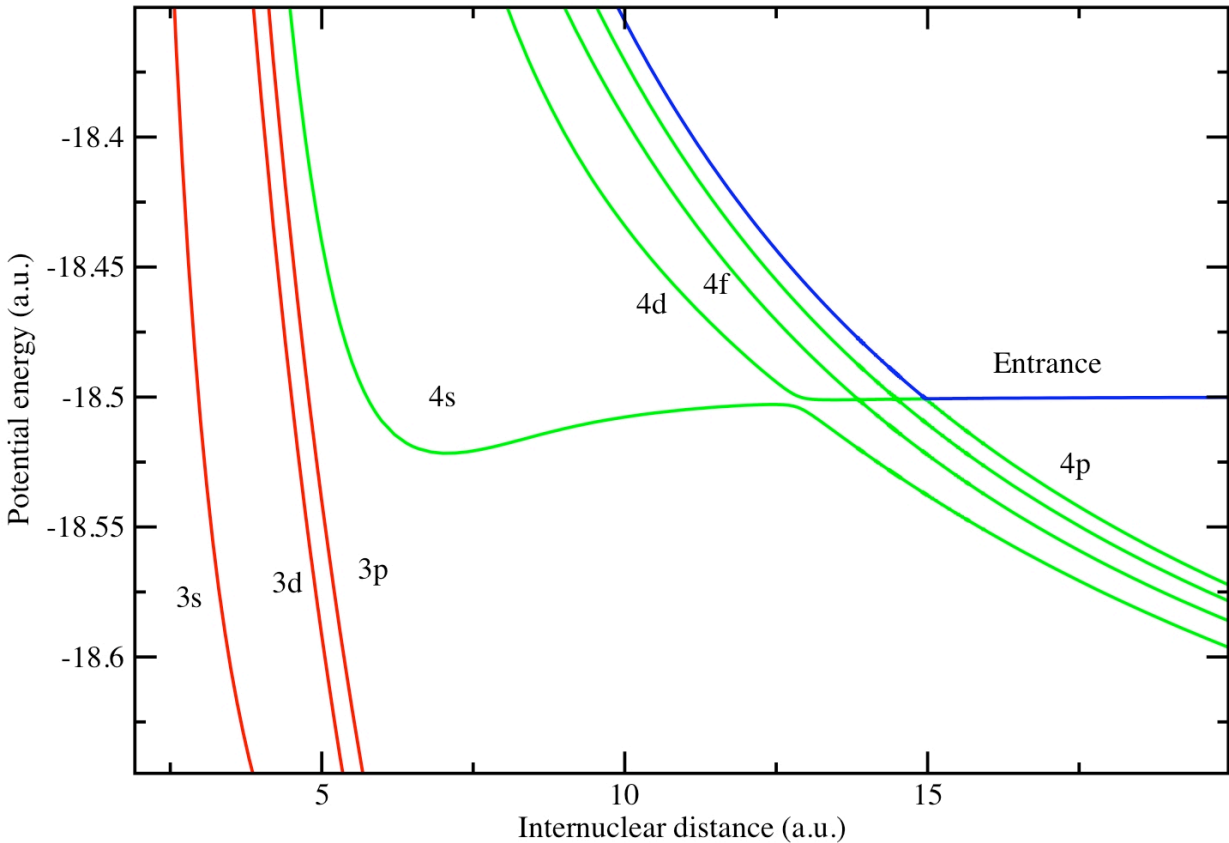


Figure 5.2: Singlet adiabatic potentials for  $C^{5+}+H$  (detail;  $^1\Sigma^+$  states only).

for this system using a semiclassical MOCC treatment for energies above 15 eV/u and a two-channel (entrance and 4s) quantum MOCC treatment for both singlets and triplets for lower energies. Comparison with their  $n, l, S$ -resolved cross sections (see their Figure 8) shows agreement that the  $n = 4$  manifold dominates singlets and triplets at low energies, with the 4s channel dominating up to energies between 0.1 to 1 keV/u. In this energy range, however, the ordering of the magnitude of capture into different  $n = 4$  states between the two calculations begins to disagree, while they show  $n = 3$  channels making roughly equal contributions as the  $n = 4$  to the total cross section around 1 keV/u. Total cross sections at this energy, however, seem to be in rough agreement to within a factor of less than two.

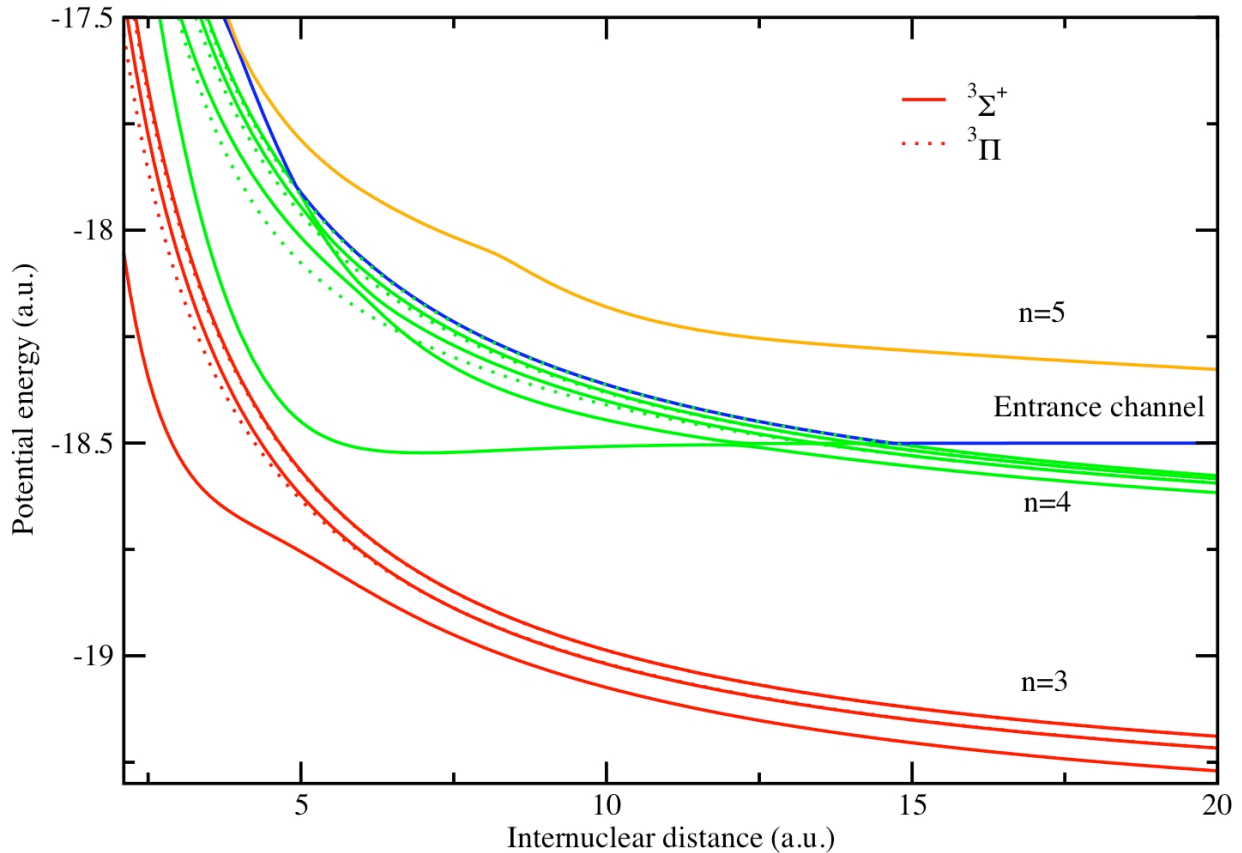


Figure 5.3: Triplet adiabatic potentials for  $C^{5+} + H$ .

The triplet-singlet ratios for all  $n, l$ -states are plotted in Figure 5.12. As with  $O^{7+} + H$ , we observe a wide spread in triplet-singlet ratios across the range of collision energies and capture states, with only a few appearing to converge to 3:1 at higher energies. The dip in  $3p$  between 10 and 100 eV/u comes as the avoided crossing between the singlet  $3p$  and  $4s$  states becomes energetically accessible, while the triplet  $3p$  shares no avoided crossings with its adjacent  $n = 3$  states; a similar effect was observed for  $O^{7+} + H$ . The dominance of the  $4p$  ratio is likely due to the slightly wider avoided crossing between the triplet  $4s$  and  $4p$

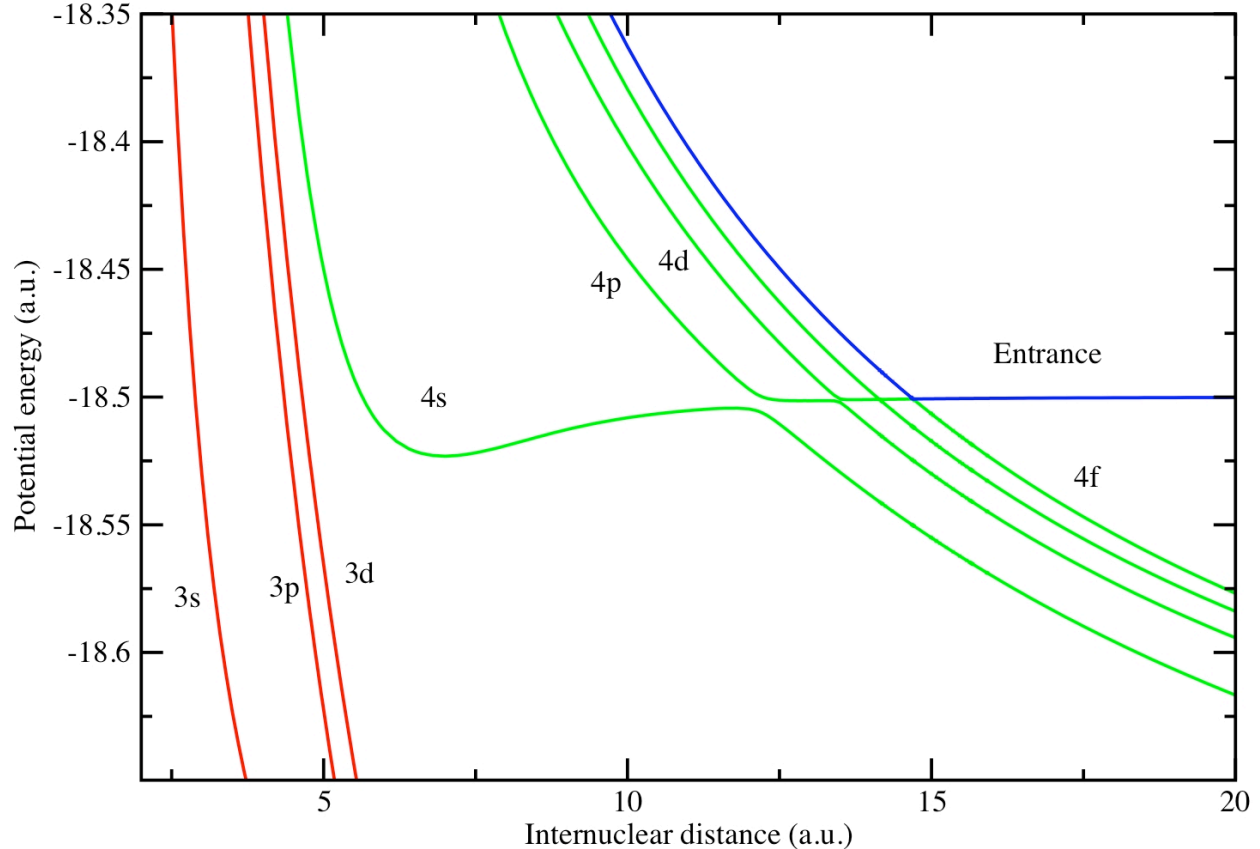


Figure 5.4: Triplet adiabatic potentials for  $C^{5+}+H$  (detail;  $^3\Sigma^+$  states only).

states, while the extremely narrow avoided crossings between the singlet  $4p$  channel and its adjacent channels ensure that there will be a much smaller portion of flux into this channel.

A comparison of total MOCC cross sections with those obtained by CTMC and AOCC methods (from Schultz and Hui, private communication [123]), as well as previous MOCC results by Bottcher and Heil (1982) [131], a proposed fit by Suno and Kato (2005) [132], and experimental results [27, 24, 28, 29, 30] is shown in Figure 5.13. Agreement between the present MOCC results and available data below about 100 eV/u is generally good. The fit by Suno and Kato is based on MOCC calculations by Shimakura et al. [26] and CTMC calculations by Shipsey et al. [133], as well as experimental results [24, 28, 30], for all of

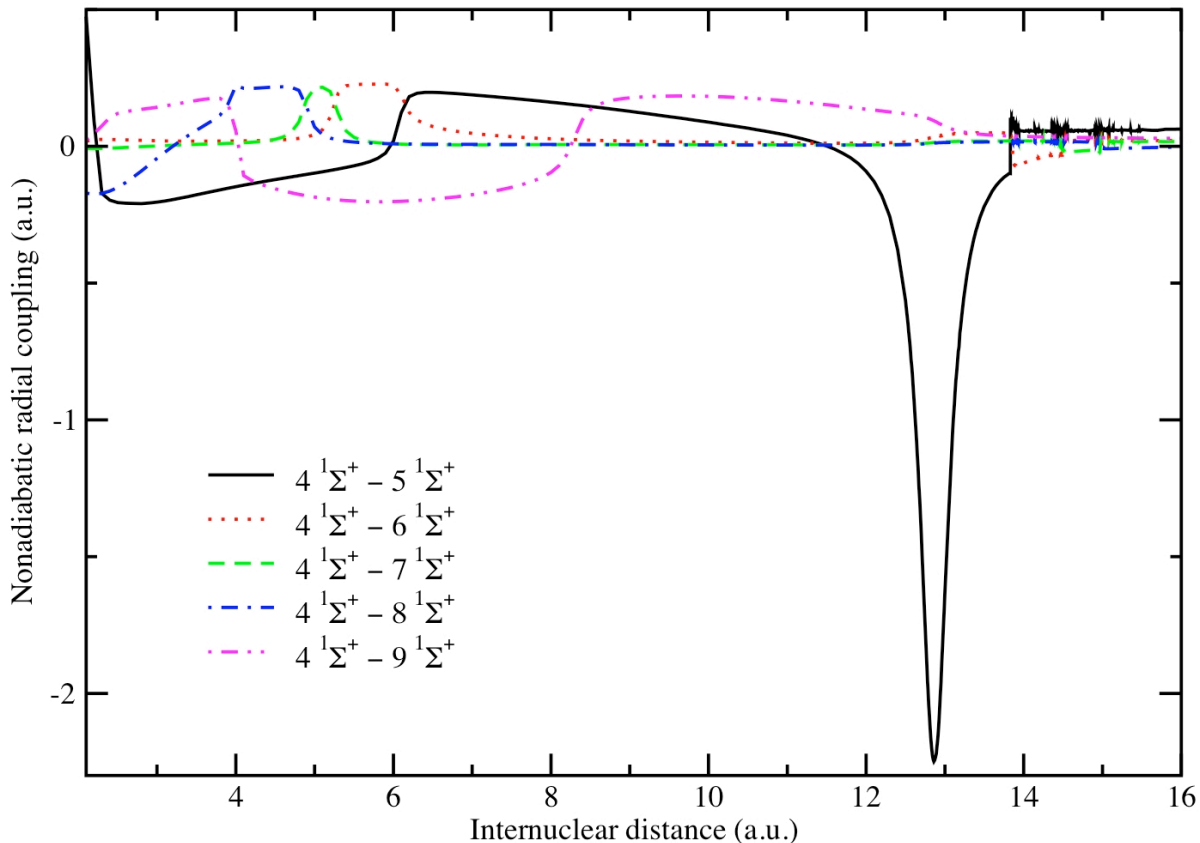


Figure 5.5: Family of ( $4 \ ^1\Sigma^+ - N \ ^1\Sigma^+$ ) nonadiabatic radial couplings for  $\text{C}^{5+} + \text{H}$ .

which the lowest represented energy is about 10 eV/u, and in the range 10-100 eV/u we find generally good agreement with the present calculations. The MOCC calculations by Bottcher and Heil, meanwhile, only included three  $\Sigma$  states, and are unlikely to be accurate for the higher energies reported. Considering also the good agreement with the most recent experimental results by Draganić et al. [27] at lower energies, our results below about 100 eV/u appear to be reasonable. As with  $\text{O}^{7+} + \text{H}$ , our results are seen to diverge from the available data above this energy, and we expect the sources of this discrepancy to be similar to those already discussed in the last chapter, namely, insufficient basis set size, uncertainty

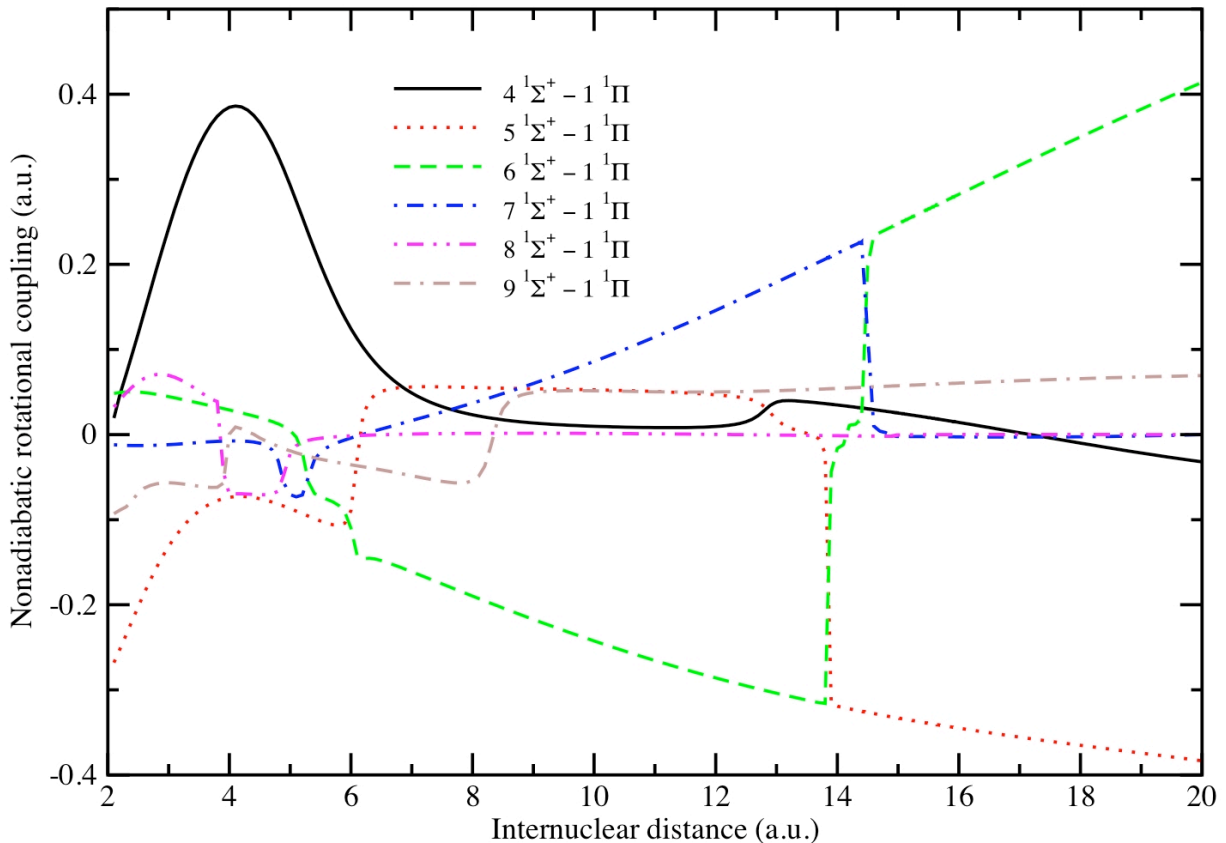


Figure 5.6: Family of ( $N$   $^1\Sigma^+$  -  $1$   $^1\Pi$ ) nonadiabatic rotational couplings for  $C^{5+}+H$ .

in the relative phases of nonadiabatic couplings and, perhaps to a lesser extent, neglect of electron translation factors and ionization. The AOCC results, on the other hand, appear to slightly underestimate the total cross section between about  $10^2$  and  $10^3$  eV/u, but agree well with the fit by Suno and Kato above 5 keV/u. Data for CTMC, however, is not available for higher energies and is almost certainly not applicable at the energies represented here.

In Figure 5.14, we show  $n$ -resolved cross sections for MOCC, AOCC, and CTMC calculations as well as translation energy spectroscopy (TES) measurements by Kearns et al. [25] for one collision energy. For the dominant  $n = 4$  channel, we find a factor of roughly 2-3 discrepancy between MOCC and AOCC calculations in the overlap region, and larger

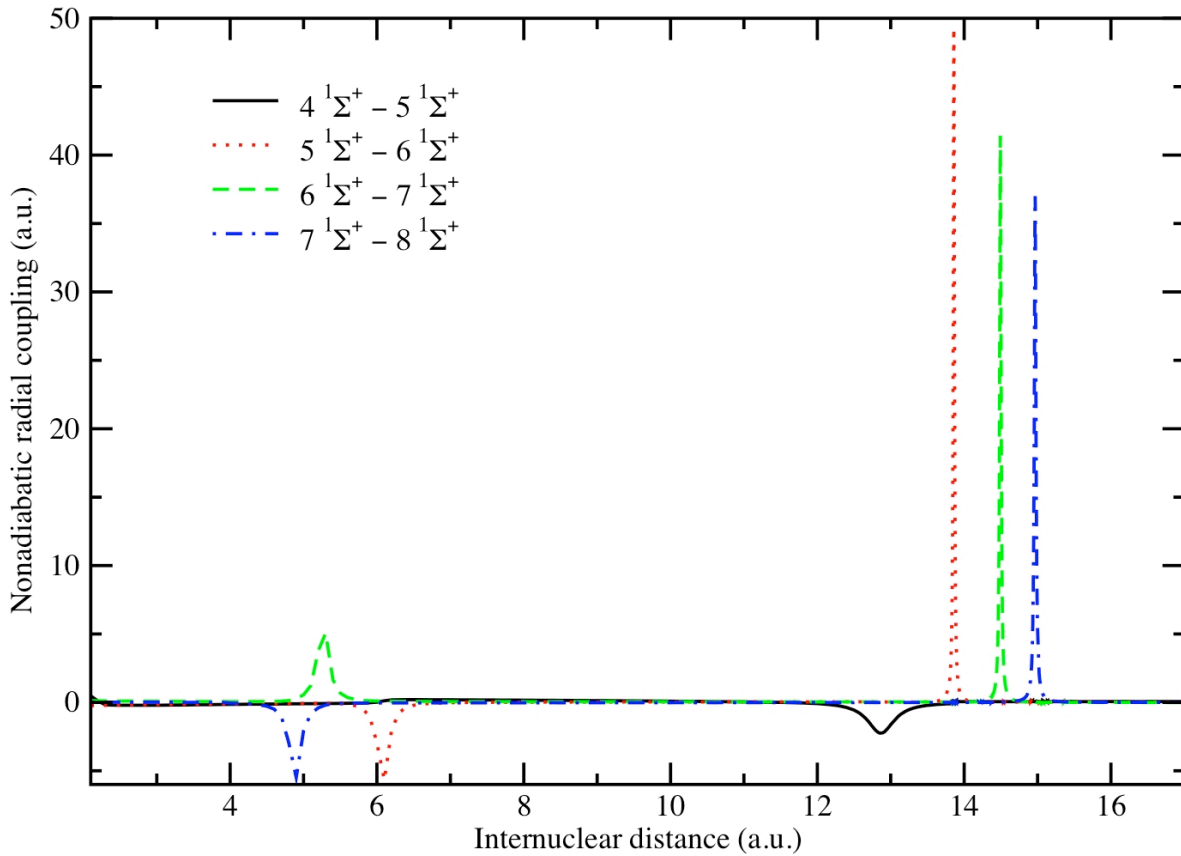


Figure 5.7: Nonadiabatic radial couplings with avoided crossings for adjacent  $n = 4$  singlet channels for  $C^{5+} + H$ .

discrepancies for the  $n = 3$  and  $n = 5$  channels, although with good agreement between 600 and  $10^3$  eV/u for  $n = 3$ . Interestingly, we also find  $n = 5$  and  $n = 3$  making comparable contributions around 100-400 eV/u in the AOCC data, suggesting that capture into  $n = 5$  may in fact be significant relative to  $n = 3$  at these and lower energies. Kearns et al., MOCC, and AOCC results agree that  $n = 4$  is the dominant channel, but the MOCC results are alone in asserting the dominance of the  $n = 5$  over the  $n = 3$  channel above 300 eV/u. Again, CTMC results are only given at energies too low to make a meaningful comparison with the AOCC data.

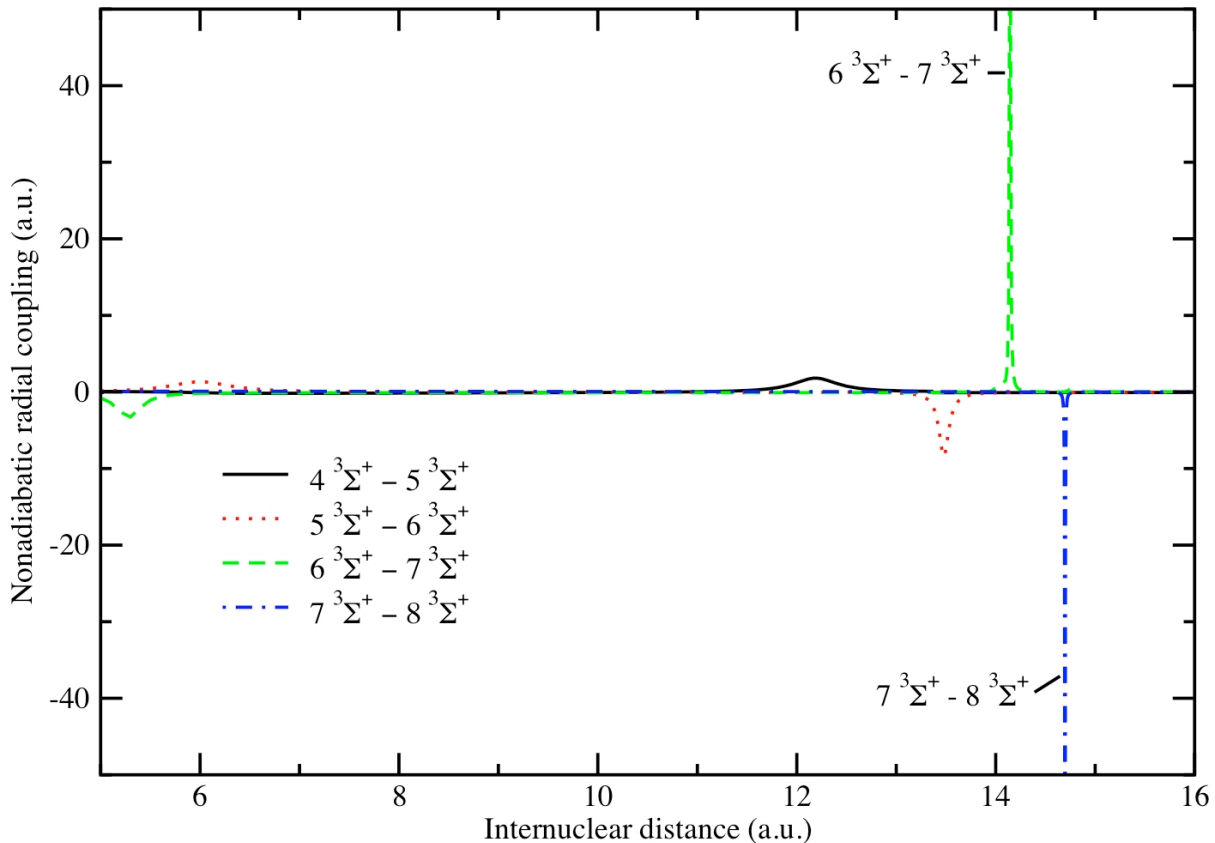


Figure 5.8: Nonadiabatic radial couplings with avoided crossings for adjacent  $n = 4$  triplet channels for  $C^{5+} + H$ .

Figures 5.15 and 5.16 show comparisons of the  $l$ -distribution of capture states for  $n = 5$  for each of the theoretical methods as well as the statistical and low-energy distributions for  $E = 300$  and  $1000$  eV/u (see Equations (4.21) and (4.22)). As with  $O^{7+} + H$ , we again find AOCC results approaching a statistical distribution at all energies, more so with increasing energy. Conversely, the MOCC  $l$ -distribution is similar to the low-energy distribution function, except that the former is dominated by  $l = 0$ . Surprisingly, the CTMC distributions are very close to the MOCC results. This reinforces our previous suggestion for the case of  $O^{7+} + H$ , that simple analytical models for  $l$ -distribution may be unreliable at solar wind

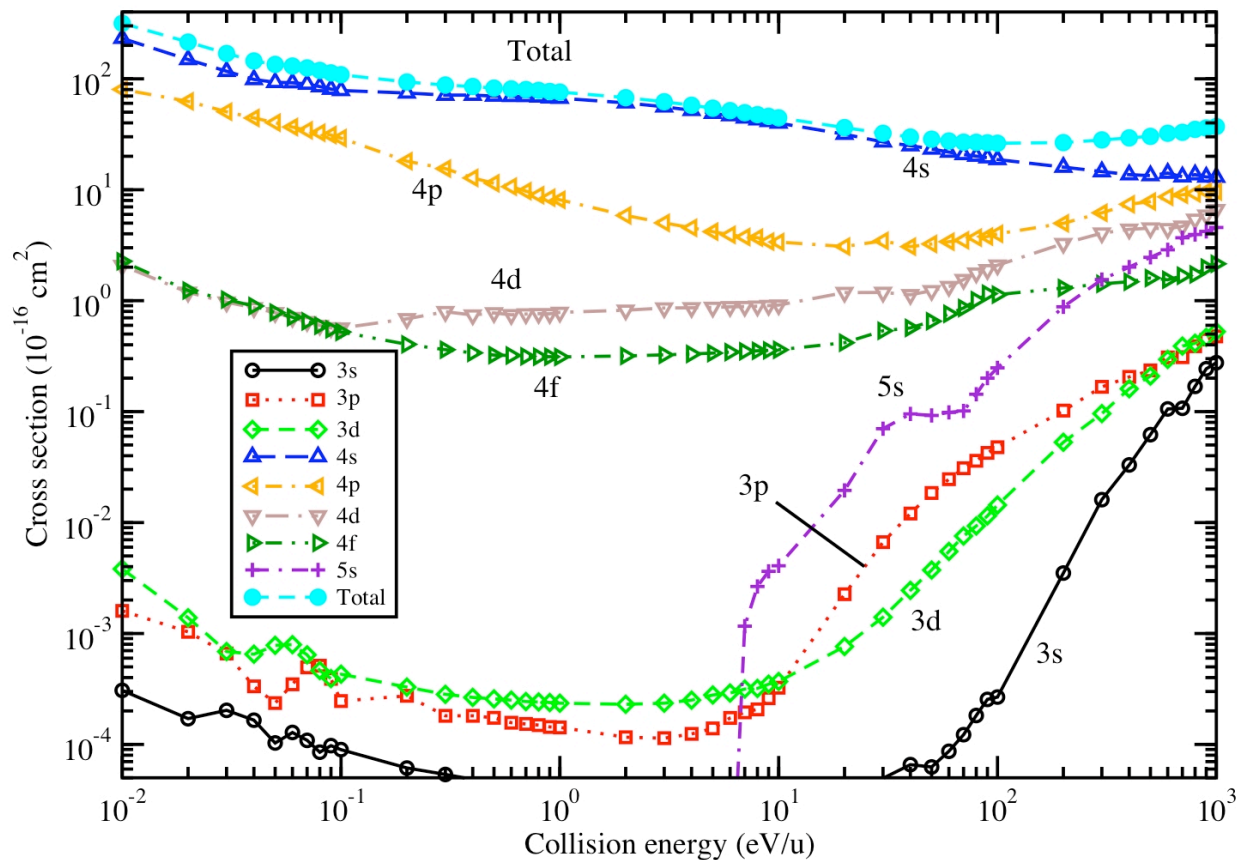


Figure 5.9: Total  $n, l$ -resolved MOCC cross sections for  $\text{C}^{5+} + \text{H}$ .

energies. See Appendix B for detailed comparisons of the MOCC, AOCC, and CTMC cross sections as a function of energy at the  $n, l$ -level.

As for x-ray modeling, our recommended fits to  $n, l$ -resolved cross sections follow the same guidelines as those laid out for  $\text{O}^{7+} + \text{H}$ , namely, the use of MOCC results for low energies up to between  $10^2$  and  $10^3$  eV/u, AOCC for the intermediate range up to about  $10^5$  eV/u, and CTMC, if available, for all higher energies. Again, triplet-singlet ratios may be obtained from the present MOCC results and extrapolated to approach a statistical distribution at higher energies.

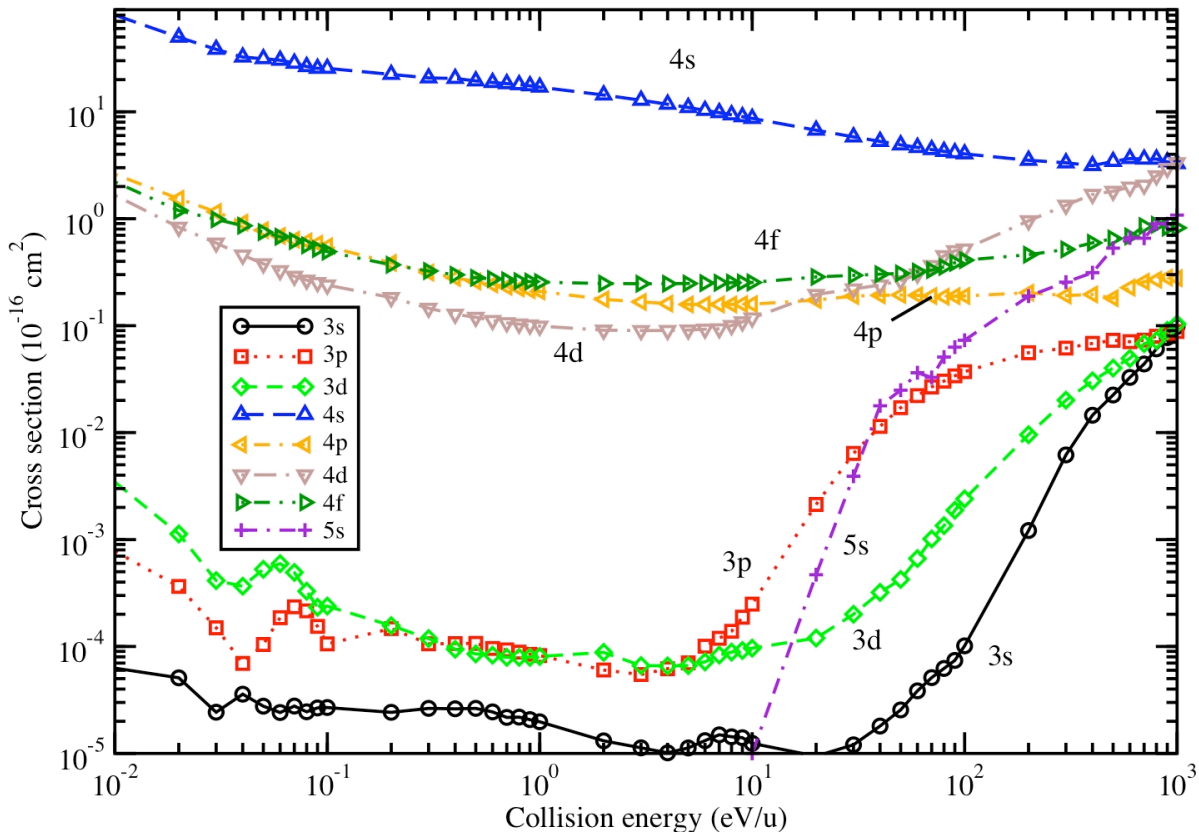


Figure 5.10: Singlet  $n, l$ -resolved MOCC cross sections for  $C^{5+}+H$ .

#### 5.4 CONCLUSIONS

We have performed MOCC calculations of  $l$ - and  $S$ -resolved cross section for single electron capture into the  $n = 3, 4$ , and  $5$  manifolds for the system  $C^5+H$ . We find generally good agreement between the present results and available theoretical and experimental data below  $100$  eV/u. We also find considerable contributions from  $n = 5$  to the total cross section at energies greater than  $\sim 7$  eV/u, and comparison with AOCC results at  $100$ - $500$  eV/u confirms this. As with  $O^{7+}+H$ , we recommend fits to cross sections based on the present

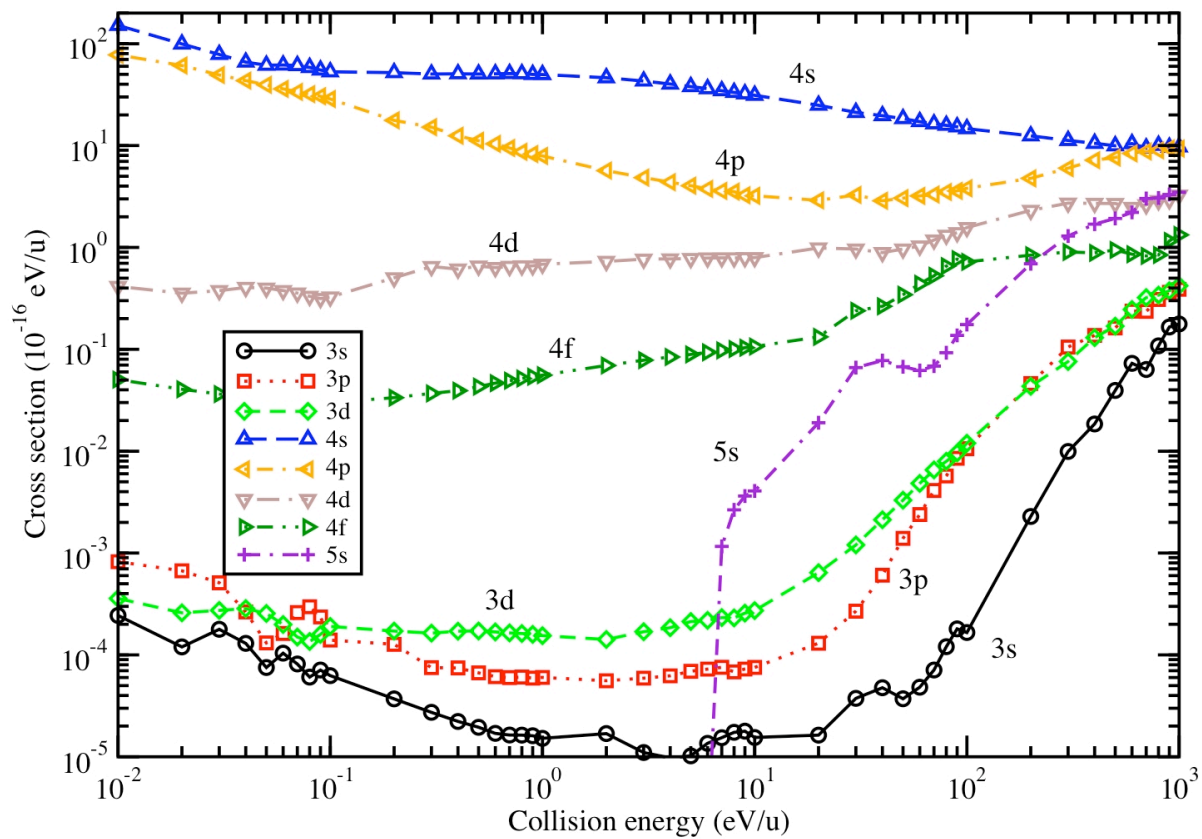


Figure 5.11: Triplet  $n, l$ -resolved MOCC cross sections for  $C^{5+} + H$ .

MOCC results for energies below  $10^2$  to  $10^3$  eV/u, with AOCC and CTMC results to be used for modeling at higher energies.

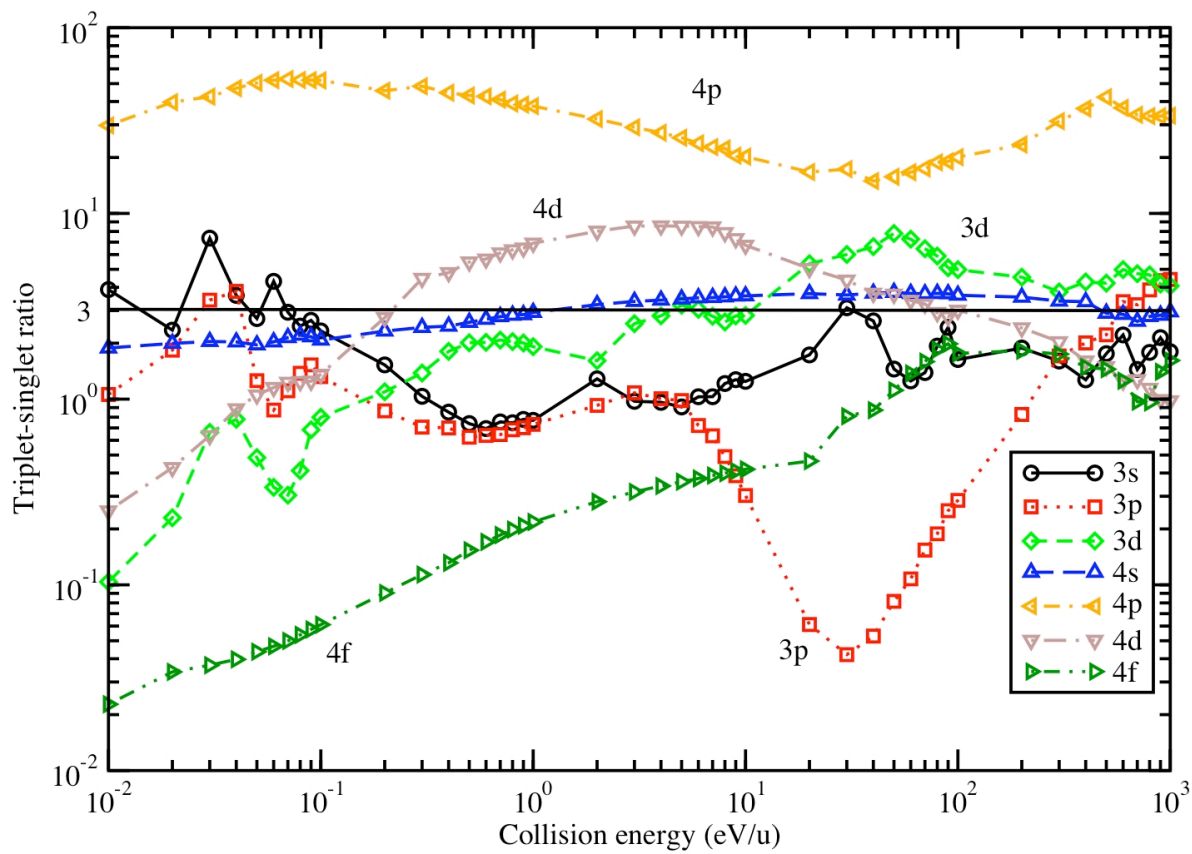


Figure 5.12: Triplet-singlet ratios for  $n, l$ -resolved cross sections for  $C^{5+} + H$ .

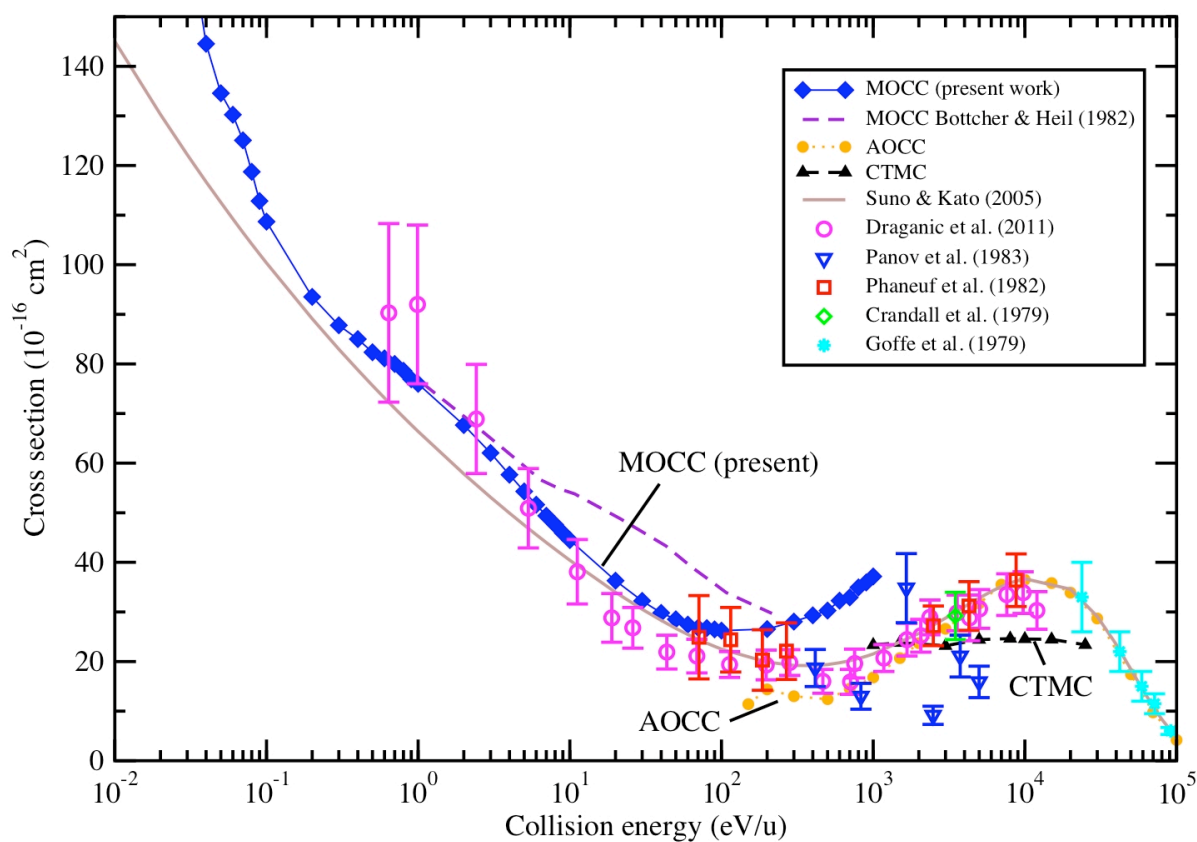


Figure 5.13: Comparison of total cross sections for  $C^{5+}+H$  using MOCC, as well as AOC and CTMC [123] methods. Also included are previous MOCC results by Bottcher and Heil (1982) [131], a fit by Suno and Kato (2005) based on previous theoretical and experimental results [132], and experimental results of Draganić et al. (2011) [27], Panov et al. (1983) [24], Phaneuf et al. (1982) [28], Crandall et al. (1979) [29], and Goffe et al. (1979) [30].

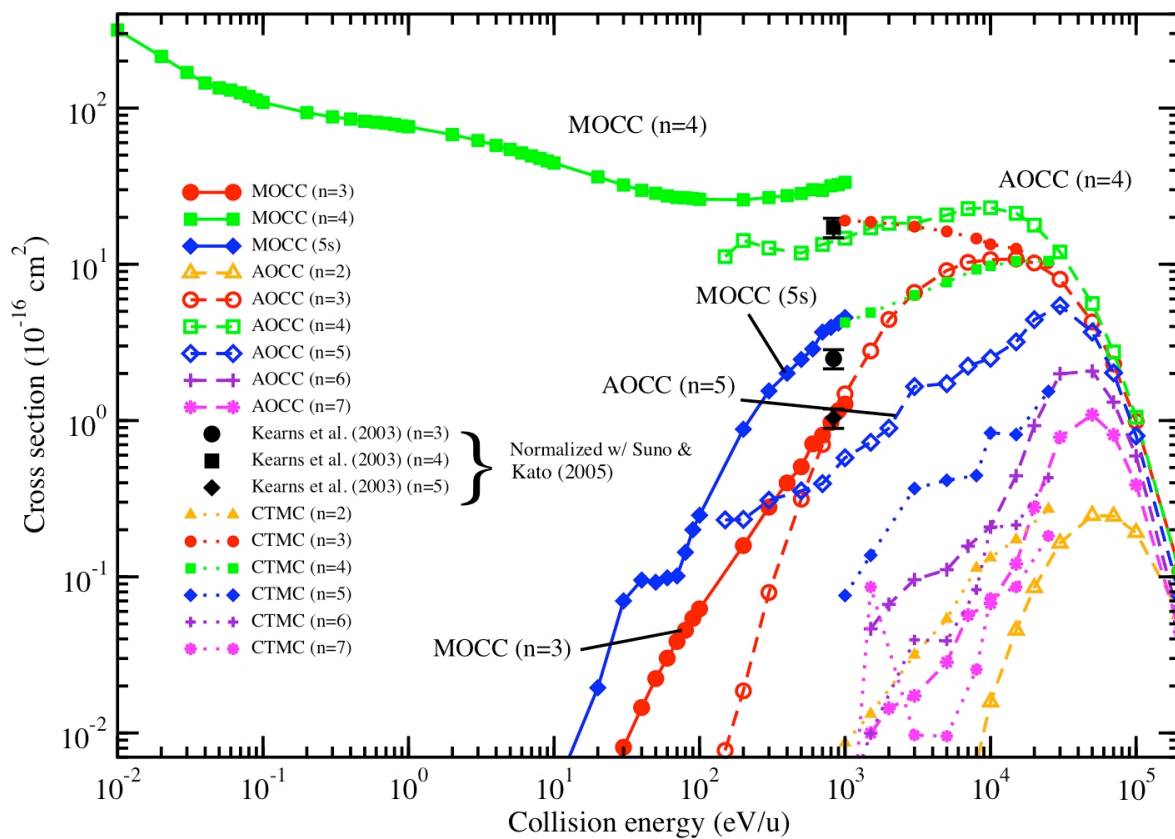


Figure 5.14: Comparison of  $n$ -resolved cross sections for  $C^{5+} + H$  for MOCC, AOCC, CTMC calculations and experimental results of Kearns et al. [25]. (Error bars estimated from their  $O^{7+} + H$  data).

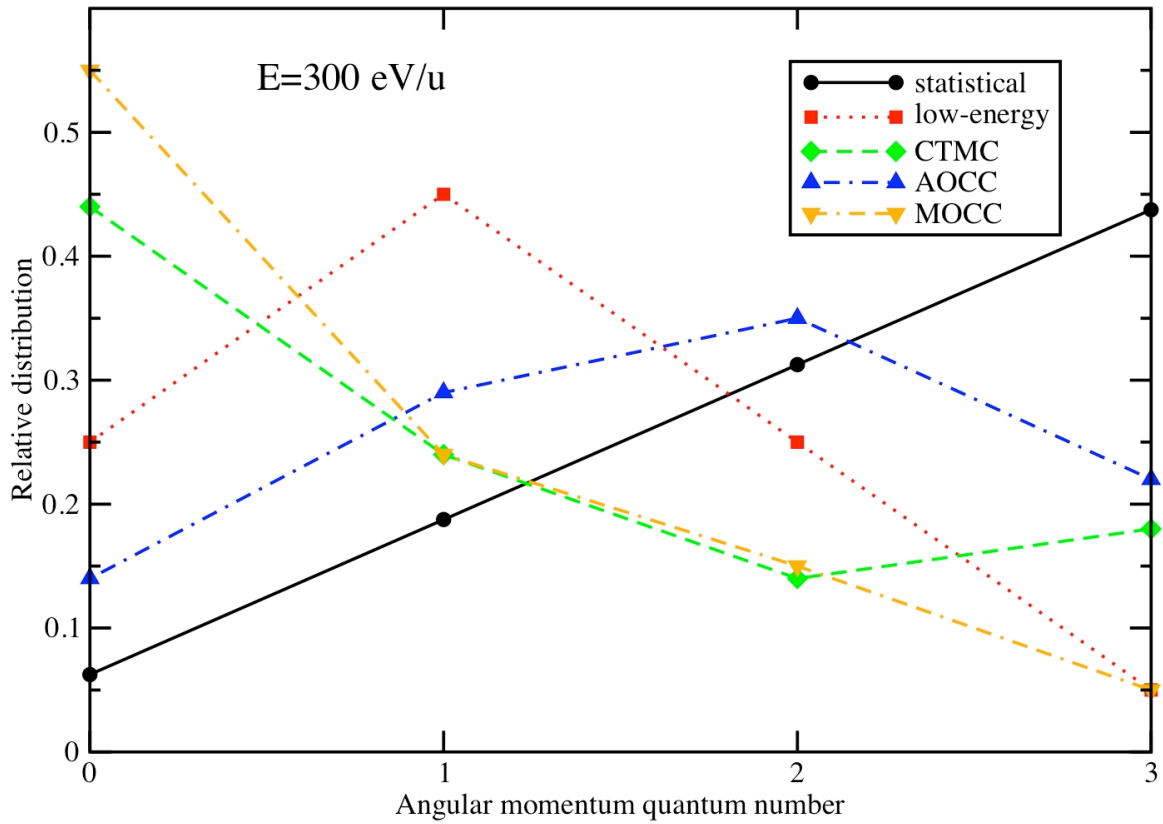


Figure 5.15: Comparison of  $n = 4$   $l$ -distributions  $C^{5+}+H$  for MOCC, AOCC and CTMC, along with statistical and low-energy distributions at  $E = 300$  eV/u.

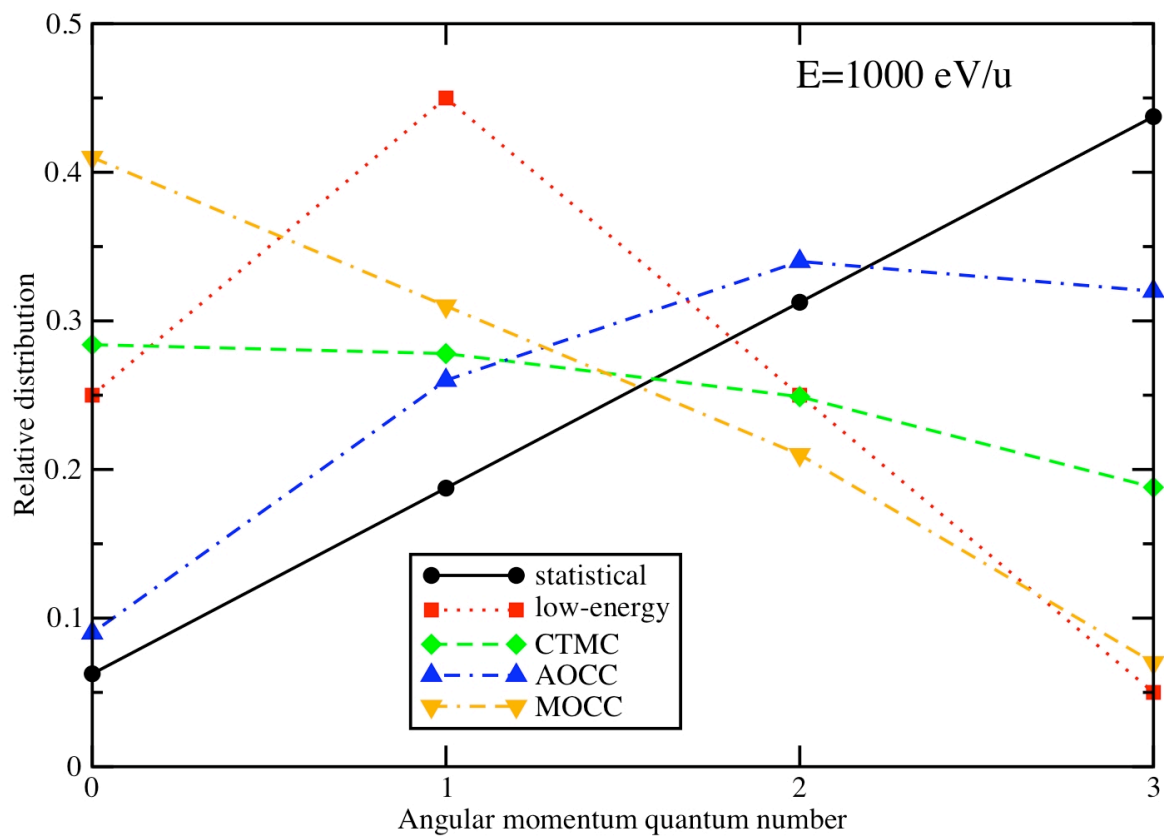


Figure 5.16: Comparison of  $n = 5$   $l$ -distributions for  $C^{5+}+H$  for MOCC, AOCC and CTMC, along with statistical and low-energy distributions at  $E = 1000$  eV/u.

## CHAPTER 6

### CONCLUSIONS

In this work we have focused on several atomic, ionic, and molecular scattering systems of astrophysical importance. Due to the limited availability, reliability, and scope of experimental data for many collision systems of interest, we must often turn to theoretical methods to supplement our knowledge of the relevant collision systems. The primary aim of this work has therefore been the investigation of various scattering processes and reporting of the relevant cross sections and rate coefficients using fully quantum mechanical close-coupling methods.

In Chapter 2 we calculated cross sections and rate coefficients for the He-HD system, which plays an important cooling role in the collapse of primordial clouds in early star formation. By adopting a large basis set and by using accurate HD numerical wavefunctions to determine the potential matrix elements, as opposed to a harmonic oscillator approximation for the HD vibrational wavefunctions, we believe we have improved upon the available theoretical results, represented mainly by those of Roueff and Zeppen [4], in addition to extending the range of vibrational states considered and energy range of the calculations. The new He-HD rate coefficients will allow for improvements in the HD cooling function for low and high temperatures. In future work, we plan to perform similar calculations for rotational excitation of HD by H<sub>2</sub>.

We have explored in Chapter 3 how changes in the collision system reduced mass affected the complex scattering length for collisions of H<sub>2</sub> with <sup>3</sup>He and <sup>4</sup>He at low energies. By changing the reduced mass, we effectively altered the interaction potential of the system, thereby revealing zero-energy resonances corresponding to bound states of He-H<sub>2</sub> with  $v = 1$ ,

$j = 0$  lying below the dissociation limit. We also find a  $p$ -wave resonance appearing in the range  $0.1 - 1 \text{ cm}^{-1}$  for  ${}^4\text{He-H}_2$  and its isotopomers, the experimental detection of which would provide a critical test of the spherical component of the He-H<sub>2</sub> interaction potential.

Finally, in Chapters 4 and 5 we have reported  $n, l, S$ -resolved cross sections for the charge exchange systems  $\text{O}^{7+}+\text{H}$  and  $\text{C}^{5+}+\text{H}$ , which are dominant contributors to x-ray emission within the Solar System. No experimental  $l, S$ -resolved cross sections for these systems that we know of exist in the literature, nor do any  $l, S$ -resolved fully quantum calculations containing more than a couple capture channels. To fill this lacuna, we have used a fully quantum mechanical molecular orbital close-coupling treatment to obtain cross sections for these systems at energies below  $1 \text{ keV/u}$ . Supplemented with AOCC and CTMC data at higher energies, these calculations will provide the basis for a recommended set of cross sections for the scattering systems, with triplet-singlet ratios extrapolated from the MOCC data at higher energies.

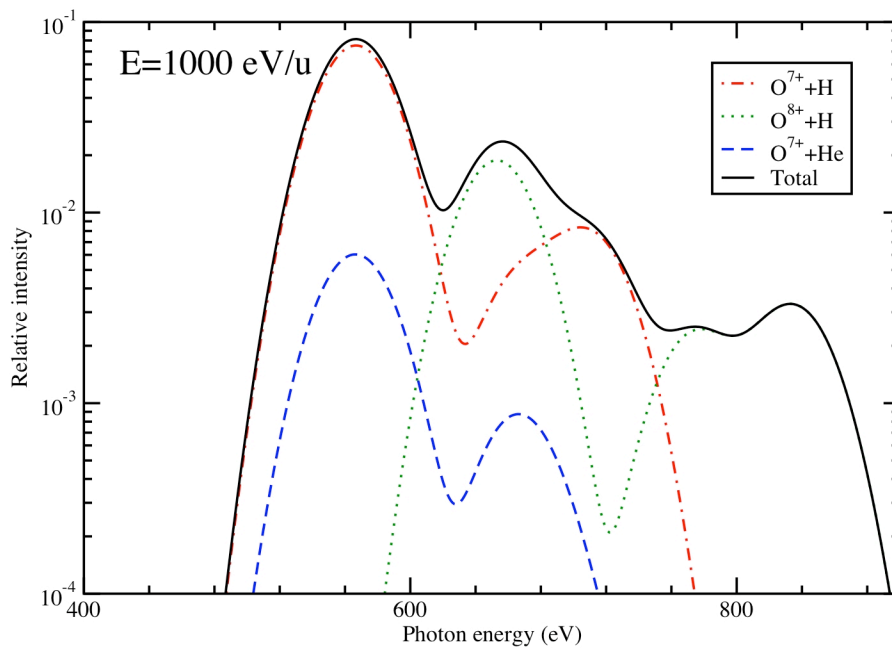


Figure 6.1: Combined spectra of  $\text{O}^{7+}+\text{H}$ ,  $\text{O}^{8+}+\text{H}$ ,  $\text{O}^{7+}+\text{He}$ .

As a preview of further research in this area, we show in Figure 6.1 a preliminary calculation of the x-ray spectrum of O VII and O VIII emission from charge exchange with H and He at 1 keV/u. We see clearly in the case of O<sup>7+</sup> the dominant peak at  $\sim 570$  eV arising from the K $\alpha$  complex and the smaller K $\beta$  peak at  $\sim 670$  eV, with the O<sup>8+</sup> Ly $\alpha$  line at  $\sim 650$  eV and all higher Lyman transitions dominating for photon energies  $\geq 775$  eV. Emission spectra such as this will prove a vital ingredient in the modeling of heliospheric x-ray emission, as well as perhaps that of other astrophysical environments such as forward shocks of supernova remnants, as exciting recent observations of the Cygnus Loop by *Suzaku* suggest [107]. Given the wealth of relevant scattering systems for which we lack sufficient data, the demand for further research in this area remains great.

## BIBLIOGRAPHY

- [1] D. R. Flower, *Mon. Not. R. Astron. Soc.*, **318**, 875 (2000).
- [2] J. Schaefer, *Astron. Astrophys. Sup.*, **85**, 1101 (1990).
- [3] E. Roueff and C. J. Zeippen, *Astron. Astrophys.*, **343**, 1005 (1999).
- [4] E. Roueff and C. J. Zeippen, *Astron. Astrophys. Sup.*, **142**, 475 (2000).
- [5] M. J. Jamieson and B. Zygelman, *Phys. Rev. A* **64**, 032703 (2001).
- [6] T. G. Kreutz, L. Eno, and H. Rabitz, *J. Chem. Phys.* **88**, 6322 (1988).
- [7] E. Bodo, F. A. Gianturco, N. Balakrishnan, and A. Dalgarno, *J. Phys. B* **37**, 3641 (2004).
- [8] N. Balakrishnan, V. Kharchenko, R. C. Forrey, and A. Dalgarno, *Chem. Phys. Lett.* **280**, 5 (1997).
- [9] D. McCammon and W. T. Sanders, *Ann. Rev. Astron. Astrophys.* **28**, 657 (1990).
- [10] S. L. Snowden, et al., *Astrophys. J.* **493**, 715 (1998).
- [11] D. McCammon, et al., *Astrophys. J.* **576**, 188 (2002).
- [12] M. Markevitch, et al., *Astrophys. J.* **583**, 70 (2003).
- [13] S. L. Snowden, M. R. Collier, and K. D. Kuntz, *Astrophys. J.* **610**, 1182 (2004).
- [14] R. Fujimoto, et al., *Prog. Theor. Phys. Supp.* **169**, 71 (2007).
- [15] R. K. Smith, et al., *Publ. Astron. Soc. Jpn.* **59**, S141 (2007).

- [16] D. P. Cox in *The Local Bubble and Beyond*, eds. D. Breitschwerdt, M. J. Freybert, and J. Trümper (Berlin: Springer, 1998).
- [17] T. E. Cravens, *Geophys. Res. Lett.* **24**, 105 (1997).
- [18] T. E. Cravens, *Science* **296**, 1042 (2002).
- [19] T. E. Cravens, *Astrophys. J.* **532**, L153 (2000).
- [20] I. P. Robertson and T. E. Cravens, *J. Geophys. Res.* **08**, 8031
- [21] D. Koutroumpa, F. Acero, R. Lallement, J. Ballet, and V. Kharchenko, *Astron. Astrophys.* **475**, 901 (2007).
- [22] C. C. Havener, I. N. Draganic, D. R. Schultz, Y. Wu, and P. C. Stancil, *Phys. Rev. A*, submitted (2011).
- [23] F. W. Meyer, et al., *Phys. Rev. A* **32**, 3310 (1985).
- [24] M. N. Panov, A. A. Basalaev, and K. O. Lozhkin, *Phys. Scripta* **T3**, 124 (1983).
- [25] D. M. Kearns, R. W. McCullough, R. Trassl, and H. B. Gilbody, *J. Phys. B - At. Mol. Opt.* **36**, 3653 (2003).
- [26] N. Shimakura, S. Koizumi, S. Suzuki, and M. Kimura, *Phys. Rev. A* **45**, 7876 (1992).
- [27] I. N. Draganić, D. G. Seely, and C. C. Havener, *Phys. Rev. A* **83**, 054701 (2011).
- [28] R. A. Phaneuf, I. Alvarez, F. W. Meyer, and D. H. Crandall, *Phys. Rev. A* **26**, 1892 (1982).
- [29] D. H. Crandall, R. A. Phaneuf, and F. W. Meyer, *Phys. Rev. A* **19**, 504 (1979).
- [30] T. V. Goffe, M. B. Shah, and H. B. Gilbody, *J. Phys. B* **12**, 3763 (1979).
- [31] D. Puy, G. Alecian, J. Le Bourlot, J. Léorat, and G. Pineau des Forêts, *Astron. Astrophys.*, **267**, 337 (1993).

- [32] D. Galli and F. Palla, *Astron. Astrophys.*, **335**, 403 (1998).
- [33] P. C. Stancil, S. Lepp, and A. Dalgarno, *Astrophys. J.*, **509**, 1 (1998).
- [34] D. Puy and M. Signore, *New Astron.*, **2**, 299 (1997).
- [35] D. Flower and G. Pineau des Fôrets, *Mon. Not. R. Astron. Soc.*, **323**, 672 (2001).
- [36] A. Lipovka, R. Núñez-López, and V. Avila-Reese, *Mon. Not. R. Astron. Soc.*, **361**, 850 (2005).
- [37] F. Nakamura and M. Umemura, *Astrophys. J.*, **569**, 549 (2002).
- [38] F. Nakamura and M. Umemura, *Prog. Theor. Phys. Supp.*, **147**, 99 (2002).
- [39] D. Galli and F. Palla, *Planet. Space Sci.*, **50**, 1197 (2002).
- [40] H. Uehara and S.-I. Inutsuka, *Astrophys. J.*, **531**, L91 (2000).
- [41] T. Nagakura and K. Omukai, *Mon. Not. R. Astron. Soc.*, **364**, 1378 (2005).
- [42] M. N. Machida, K. Tomisaka, F. Nakamura, and M. Y. Fujimoto, *Astrophys. J.*, **622**, 39 (2005).
- [43] I. D. McGreer and G. L. Bryan, *Astrophys. J.*, **685**, 8 (2008).
- [44] P. Muchnick and A. Russek, *J. Chem. Phys.*, **100**, 4336 (1994).
- [45] J. M. Hutson and S. Green, MOLSCAT ver. 14, distributed by Collaborative Computational Project 6; Daresbury Laboratory: UK Eng. Phys. Sci. Res. Council (1994).
- [46] T.-G. Lee, C. Rochow, R. Martin, T. K. Clark, R. C. Forrey, N. Balakrishnan, P. C. Stancil, D. R. Schultz, A. Dalgarno, and G. J. Ferland, *J. Chem. Phys.*, **122**, 024307 (2005).
- [47] A. I. Boothroyd, P. G. Martin, and M. R. Peterson, *J. Chem. Phys.*, **119**, 3187 (2003).

- [48] D. R. Flower, *Molecular Collisions in the Interstellar Medium*, 2nd ed., University Press, Cambridge (2007).
- [49] D. W. Schwenke, *J. Chem. Phys.*, **80**, 2076 (1988).
- [50] R. C. Forrey, N. Balakrishnan, A. Dalgarno, and S. Lepp, *Astrophys. J.*, **489** 1000 (1997).
- [51] N. Balakrishnan, M. Vieira, J. F. Babb, A. Dalgarno, R. C. Forrey, and S. Lepp, *Astrophys. J.*, **524**, 1122 (1999).
- [52] A. Mack, T. K. Clark, R. C. Forrey, N. Balakrishnan, T.-G. Lee, and P. C. Stancil, *Phys. Rev. A* **74**, 052718 (2006).
- [53] S. Paolini, L. Ohlinger, and R. C. Forrey, *Phys. Rev. A* **83**, 042713 (2011).
- [54] D. R. Flower, J. Le Boulot, G. Pineau des Fôrets, and E. Roueff, *Mon. Not. R. Astron. Soc.*, **314**, 753 (2000).
- [55] S. C. O. Glover and T. Abel, *Mon. Not. R. Astron. Soc.*, **388**, 1627 (2008).
- [56] D. A. Varshalovich and V. K. Khersonskii, *Sov. Astron. Lett.*, **2**, 227 (1977).
- [57] J. Wolcott-Green and Z. Haiman, *Mon. Not. R. Astron. Soc.*, **412**, 2603 (2011).
- [58] A. Dalgarno and E. L. Wright, *Astrophys. J.*, **174**, L49 (1972).
- [59] F. Bertoldi, R. Timmerman, D. Rosenthal, S. Drapatz, and C. M. Wright, *Astron. Astrophys.*, **346**, 267 (1999).
- [60] C. M. Wright, E. F. van Dishoeck, P. Cox, S. D. Sidher, and M. F. Kessler, *Astrophys. J.*, **515**, L29 (1999).
- [61] D. A. Neufeld, J. D. Green, D. J. Hollenbach, P. Sonnentrucker, G. J. Melnick, E. A. Bergin, R. L. Snell, W. J. Forrest, D. M. Watson, and M. J. Kaufman, *Astrophys. J.*, **647**, L33 (2006).

- [62] E. T. Polehampton, J.-P. Baluteau, C. Ceccarelli, B. M. Swinyard, and E. Caux, *Astron. Astrophys.*, **388**, L44 (2002).
- [63] E. Caux, C. Ceccarelli, L. Pagani, S. Maret, A. Castets, and J. R. Pardo, *Astron. Astrophys.*, **383**, L9 (2002).
- [64] S. K. Ramsay Howat, R. Timmerman, T. R. Geballe, F. Bertoldi, and C. M. Mountain, *Astrophys. J.*, **566**, 905 (2002).
- [65] F. Le Petit, E. Roueff, and J. Le Bourlot, *Astron. Astrophys.*, **390**, 369 (2002).
- [66] F. Le Petit, C. Nehmé, J. Le Bourlot, and E. Roueff, *Astrophys. J. Suppl. S.*, **164**, 506 (2006).
- [67] J. Doyle, B. Friedrich, R. V. Krems, and F. Masnou-Seeuws, *Eur. Phys. J. D* **31**, 149 (2004).
- [68] R. V. Krems, *Int. Rev. Phys. Chem.* **24**, 99 (2005).
- [69] P. F. Weck and N. Balakrishnan, *Int. Rev. Phys. Chem.* **25**, 283 (2006).
- [70] G. Quémener, N. Balakrishnan, and A. Dalgarno, in *Cold Molecules: Theory, Experiment and Applications*, eds. R. V. Krems, J. M. Doyle, G. Meijer, and B. Friedrich (CRC press, 2009, in press).
- [71] R. V. Krems, *Phys. Rev. Lett.* **93**, 013201 (2004).
- [72] H. R. Mayne, *J. Chem. Phys.* **73**, 217 (1980). (1988).
- [73] N. Balakrishnan, *J. Chem. Phys.* **121**, 5563 (2004).
- [74] E. A. Donley, N. R. Claussen, S. T. Thompson, and C. E. Wieman, *Nature (London)* **417**, 529 (2002).
- [75] M. Greiner, C. A. Regal, and D. S. Jin, *Nature (London)* **426**, 537 (2003).

- [76] C. A. Regal, C. Ticknor, J. L. Bohn, and D. S. Jin, *Nature (London)* **424**, 47 (2003).
- [77] E. Wille, *et al.* *Phys. Rev. Lett.* **100**, 053201 (2008).
- [78] Z. Li, S. Singh, T. V. Tscherbul, and K. W. Madison, *Phys. Rev. A* **78**, 022710 (2008).
- [79] A. J. Moerdijk, B. J. Verhaar, and A. Axelsson, *Phys. Rev. A* **51**, 4852 (1995).
- [80] J. L. Nolte, B. H. Yang, P. C. Stancil, T.-G. Lee, N. Balakrishnan, R. C. Forrey, and A. Dalgarno, *Phys. Rev. A* **81**, 014701 (2010).
- [81] C. J. Joachain, *Quantum Collision Theory, Volume 1* (North-Holland Publishing Company, 1975).
- [82] H. B. Dwight, *Tables of Integrals and Other Mathematical Data*, Fourth Edition (The Macmillan Company, 1965).
- [83] E. P. Wigner, *Phys. Rev.* **73**, 1002 (1948).
- [84] N. Balakrishnan, R. C. Forrey, and A. Dalgarno, *Phys. Rev. Lett.* **80**, 3224 (1998).
- [85] R. C. Forrey, N. Balakrishnan, V. Kharchenko, and A. Dalgarno, *Phys. Rev. A* **58**, R2645 (1998).
- [86] R. C. Forrey, *Phys. Rev. A* **63**, 051403(R) (2001).
- [87] J. M. Hutson and S. Green, MOLSCAT computer code, version 14 (1994), distributed by Collab. Comput. Proj. No. 6, Engin. and Phys. Sci. Res. Coun. (UK).
- [88] P. Muchnick and A. Russek, *J. Chem. Phys.* **100**, 4336 (1994).
- [89] A. I. Boothroyd, P. G. Martin and M. R. Peterson, *J. Chem. Phys.* **119**, 3187 (2003).
- [90] T.-G. Lee, *et al.*, *J. Chem. Phys.* **122**, 24307 (2005).
- [91] P. Froelich, S. Jonsell, V. Kharchenko, H. R. Sadeghpour, and A. Dalgarno, *J. Phys. B* **39**, 3889 (2006).

- [92] J. C. Flasher and R. C. Forrey, Phys. Rev. A **65**, 032710 (2002).
- [93] P. Barletta, J. Tennyson, and P. F. Barker, Phys. Rev. A **78** 052707 (2008).
- [94] R. Fulton, A. I. Bishop, and P. F. Barker, Phys. Rev. Lett. **93** 243004 (2004).
- [95] V. A. Krasnopolsky, J. B. Greenwood, and P. C. Stancil, Space Sci. Rev. **113**, 271 (2004).
- [96] I. P. Robertson, K. D. Kuntz, M. R. Collier, T. E. Cravens, and S. L. Snowden, in *The Local Bubble and Beyond II*, eds. K. D. Kuntz, R. K. Smith, and S. L. Snowden (Melville, NY: AIP, 2009).
- [97] V. Kharchenko, AIP Conf. Proc. **774**, 271 (2005).
- [98] D. Koutroumpa, M. R. Collier, K. D. Kuntz, R. Lallement, and S. L. Snowden, Astrophys. J. **697** 1214 (2009).
- [99] D. B. Henley and R. L. Shelton, Astrophys. J. Suppl. S. **187**, 388 (2010).
- [100] B. J. Wargelin, et al., Astrophys. J. **607**, 596 (2004).
- [101] V. Kharchenko, Matt Rigazio, A. Dalgarno, and V. A. Krasnopolsky, Astrophys. J. **585**, L73 (2003).
- [102] T. E. Cravens, et al., J. Geophys. Res. **100**, 17153 (1995).
- [103] V. Kharchenko, A. Dalgarno, D. R. Schultz, and P. C. Stancil, Geophys. Res. Lett. **33**, L11105 (2006).
- [104] Y. Hui, D. R. Schultz, V. A. Kharchenko, P. C. Stancil, T. E. Cravens, C. M. Lisse, and A. Dalgarno, Astrophys. J. **702**, L158 (2009).
- [105] Y. Hui, et al., J. Geophys. Res. **115**, A07102 (2010).
- [106] K. Dennerl, et al., Astron. Astrophys. **451**, 709 (2006).

- [107] S. Katsuda, et al., *Astrophys. J.* **730**, 24 (2011).
- [108] J. B. Greenwood, I. D. Williams, S. J. Smith, and A. Chutjian, *Phys. Rev. A* **63**, 062707 (2001).
- [109] F. W. Blik, G. R. Woestenenk, R. Hoekstra, and R. Morgenstern, *Phys. Rev. A* **57**, 221 (1998).
- [110] H. Ryufuku, K. Sasaki, and T. Watanabe, *Phys. Rev. A* **21**, 745 (1980).
- [111] R. K. Janev, D. S. Belic, and B. H. Bransden, *Phys. Rev. A* **28**, 1293 (1983).
- [112] R. E. Olson and A. Salop, *Phys. Rev. A* **16**, 531 (1977).
- [113] A. A. Hasan, F. Eissa, R. Ali, D. R. Schultz, and P. C. Stancil, *Astrophys. J.* **560**, L201 (2001).
- [114] R. J. Buenker and S. D. Peyerimhoff, *Theoret. Chim. Acta* **35**, 33 (1974); R. J. Buenker, *Int. J. Quantum Chem.* **29**, 435 (1986); R. J. Buenker, in *Proceedings of the Workshop on Quantum Chemistry and Molecular Physics*, ed. P. G. Burton (University of Wollongong Press, Wollongong, Australia, 1980); R. J. Buenker, *Studies in Physical and Theoretical Chemistry*, ed. R. Carbo, *Current Aspects of Quantum Chemistry* 1981 Vol. 21 (Elsevier, Amsterdam, 1982).
- [115] R. J. Buenker and R. A. Phillips, *J. Mol. Struct-Theochem.* **123**, 291 (1985); S. Krebs, and R. J. Buenker, *J. Chem. Phys.* **103**, 5613 (1995); R. J. Buenker and S. Krebs, in *Recent Advances in Multireference Methods*, ed. K. Hirao (World Scientific, Singapore, 1999).
- [116] Y. Wu, P. C. Stancil, H.-P. Liebermann, P. Funke, S. N. Rai, R. J. Buenker, D. R. Schultz, Y. Hui, I. N. Draganić, and C. C. Havener, *Phys. Rev. A*, in press (2011).
- [117] T. H. Dunning, Jr., *J. Chem. Phys.* **90**, 1007 (1989).

- [118] Y. Ralchenko, A. E. Kramida, J. Reader, and NIST ASD Team (2011). *NIST Atomic Spectra Database* (ver. 4.1.0), [Online]. Available: <http://physics.nist.gov/asd3>. National Institute of Standards and Technology, Gaithersburg, MD.
- [119] W. R. Johnson, I. M. Savukov, U. I. Safronova and A. Dalgarno, *Astrophys. J. Suppl.* **141**, 543 (2002).
- [120] T. G. Heil and A. Dalgarno, *J. Phys. B* **12**, L557 (1979).
- [121] B. R. Johnson, *J. Comput. Phys.* **13**, 445 (1973).
- [122] R. Mann, F. Folkmann, and H. F. Beyer, *J. Phys. B* **14**, 1161 (1981).
- [123] D. R. Schultz and Y. Hui, private communication (2010).
- [124] R. K. Janev, H. P. Winter, and W. Fritsch, in *Atomic and Molecular Processes in Fusion Edge Plasma*, ed. R. K. Janev (New York: Plenum Press, 1995).
- [125] R. A. Phaneuf, R. K. Janev, and M. S. Pindzola, in *Atomic Data for Fusion, Vol. 5*, ORNL-6090 (1987).
- [126] L. B. Zhao, A. Watanabe, P. C. Stancil, and M. Kimura, *Phys. Rev. A* **76**, 022701 (2007).
- [127] V. A. Abramov, F. F. Baryshnikov, and V. S. Lisitsa, *J. Exp. Theor. Phys.* **27**, 464 (1978).
- [128] D. B. Henley and R. L. Shelton, *Astrophys. J.* **676**, 335 (2008).
- [129] D. J. Christian, et al., *Astrophys. J. Suppl. S.* **187**, 447 (2010).
- [130] H.-P. Liebermann and R. J. Buenker, private communication (2011).
- [131] C. Bottcher and T. G. Heil, *Chem. Phys. Lett.* **86**, 506 (1982).

[132] H. Suno and T. Kato, NIFS-DATA-91 (2005).

[133] E. J. Shipsey, J. C. Browne, and R. E. Olson, *J. Phys. B* **14**, 869 (1981).

## APPENDIX A

### $n, l$ -RESOLVED CROSS SECTIONS FOR $O^{7+}+H$

In this appendix, we show  $n, l$ -resolved cross sections for  $O^{7+}+H$  using MOCC, AOCC, and CTMC results, for principal quantum numbers  $n = 4$  and  $5$ . In future work, recommended fits for cross sections between  $10^{-2}$  and  $5 \times 10^5$  eV/u will be produced from these results.

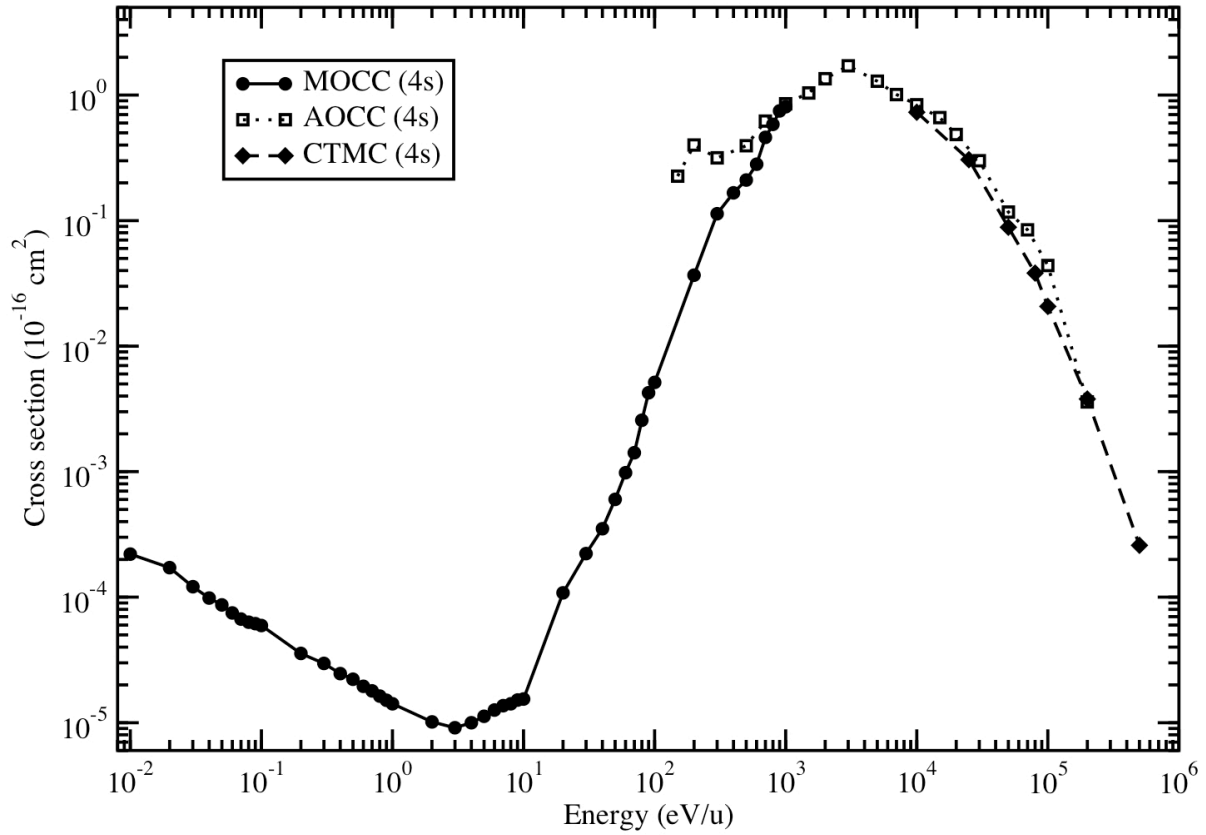


Figure A.1: Cross sections for capture into 4s for  $O^{7+} + H$ ; MOCC, AOCC, CTMC results.

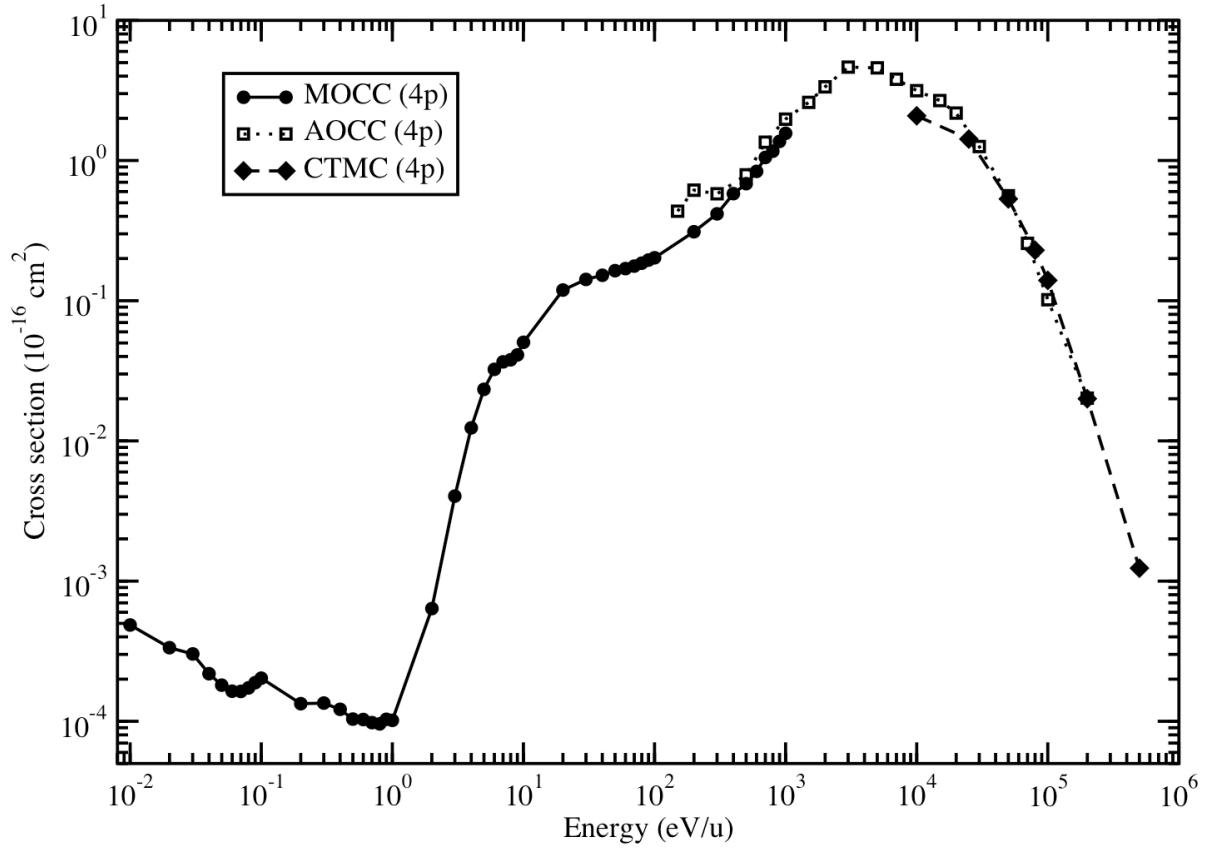


Figure A.2: Cross sections for capture into 4p for O<sup>7+</sup>+H; MOCC, AOCC, CTMC results.

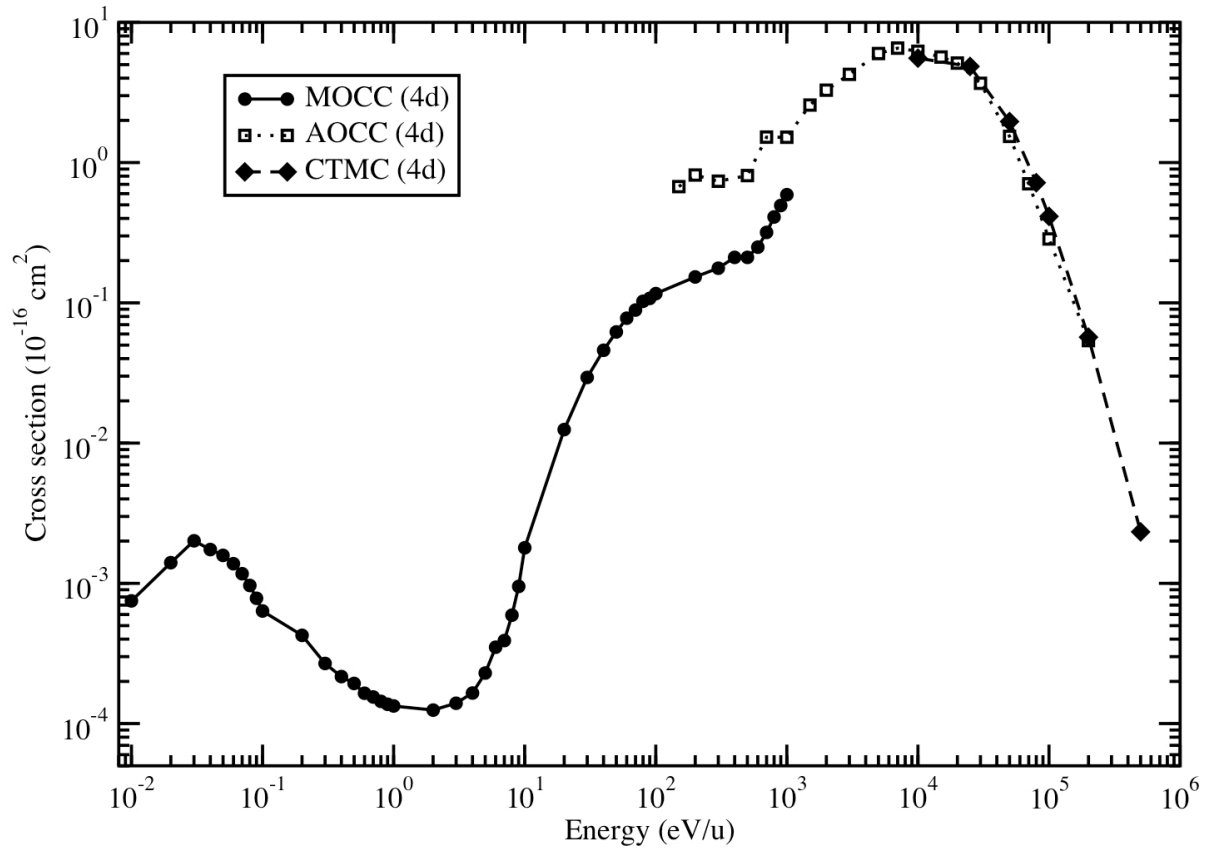


Figure A.3: Cross sections for capture into 4d for O<sup>7+</sup>+H; MOCC, AOCC, CTMC results.

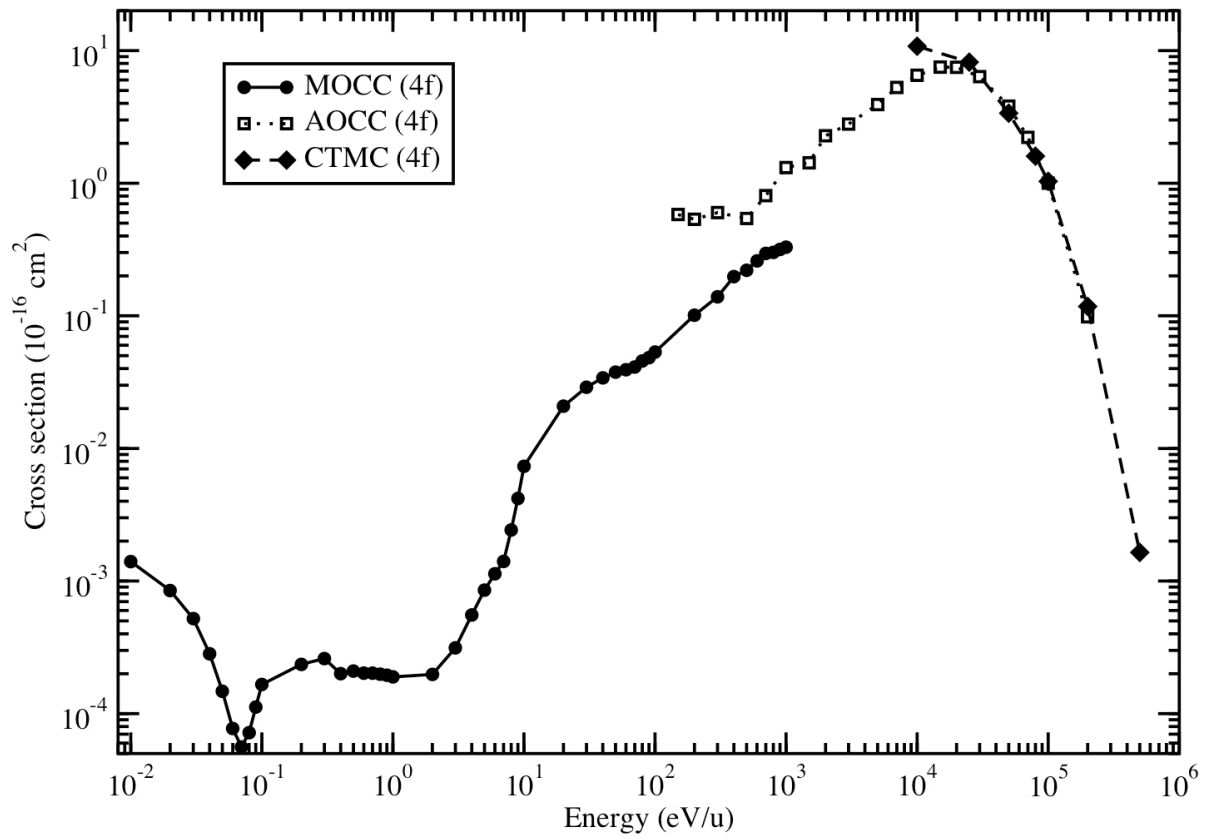


Figure A.4: Cross sections for capture into  $4f$  for  $O^{7+} + H$ ; MOCC, AOCC, CTMC results.

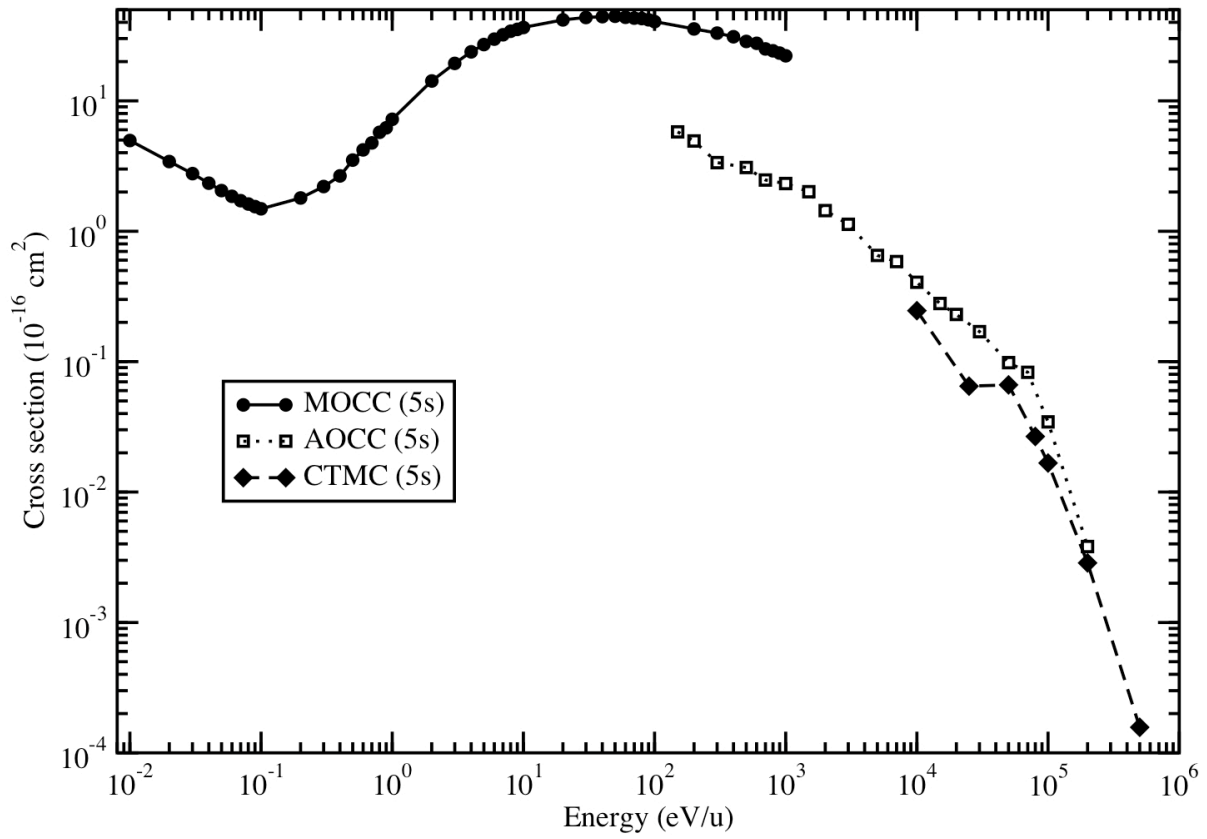


Figure A.5: Cross sections for capture into 5s for  $O^{7+}+H$ ; MOCC, AOCC, CTMC results.

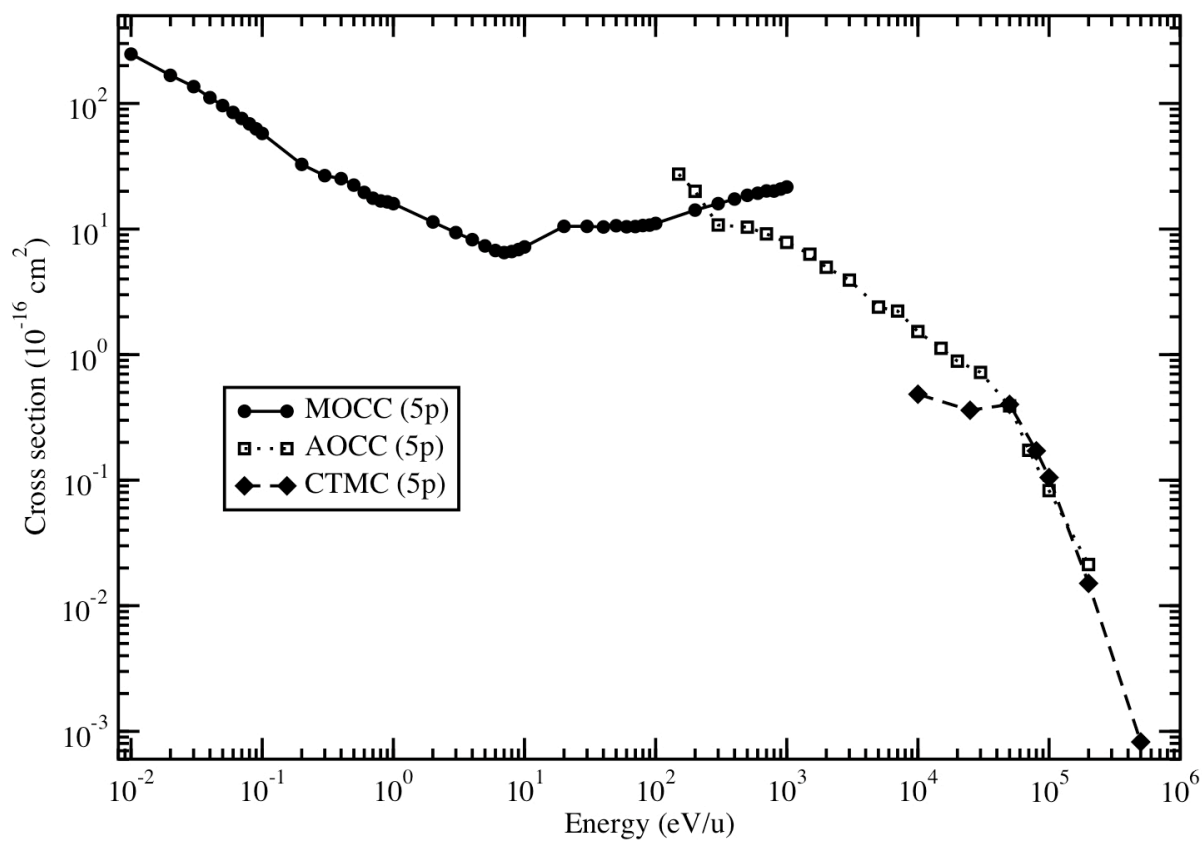


Figure A.6: Cross sections for capture into 5p for O<sup>7+</sup>+H; MOCC, AOCC, CTMC results.

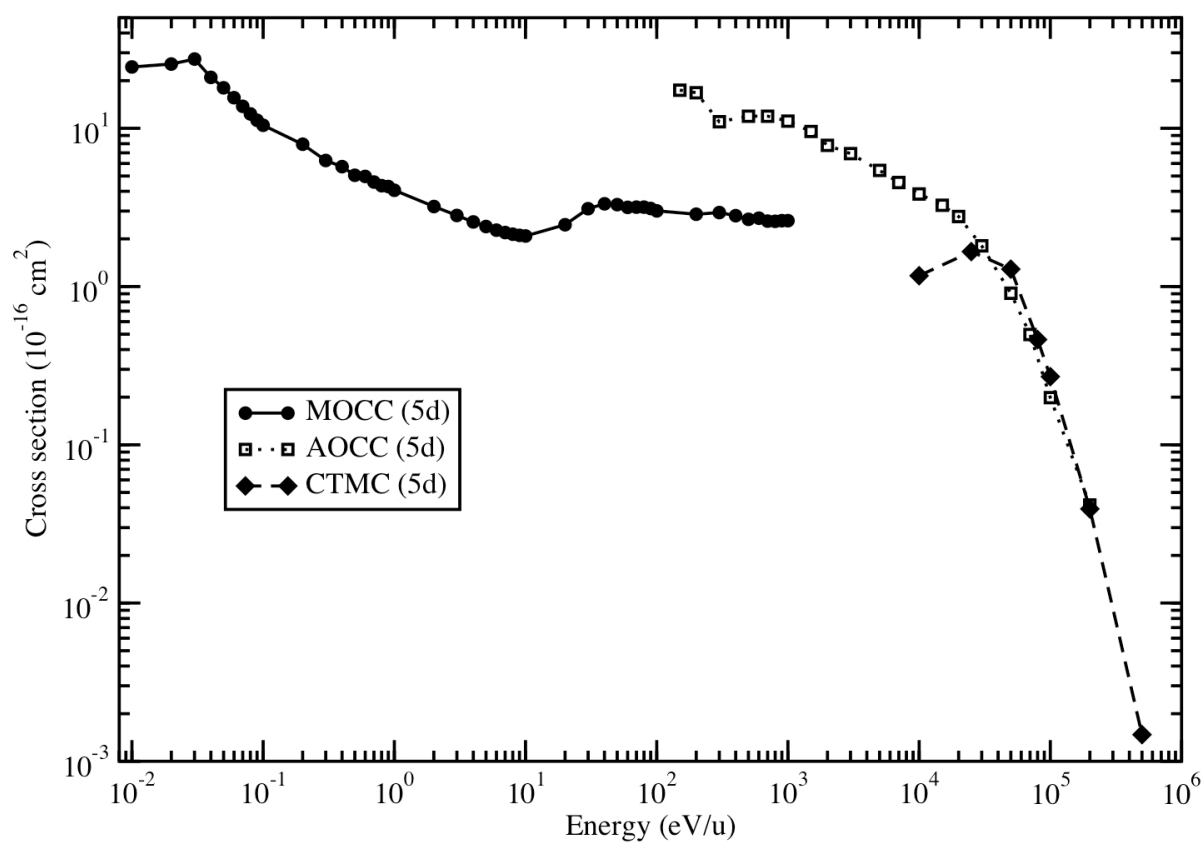


Figure A.7: Cross sections for capture into 5d for O<sup>7+</sup>+H; MOCC, AOCC, CTMC results.

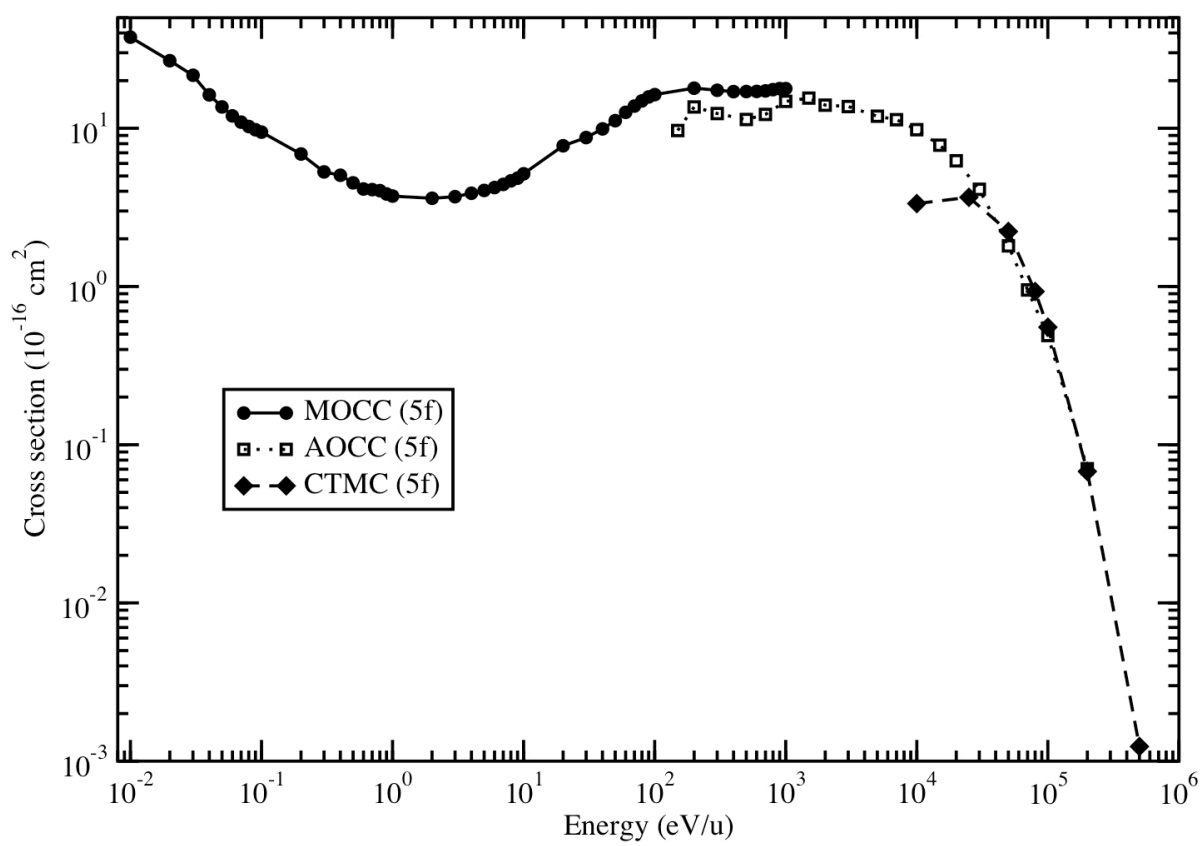


Figure A.8: Cross sections for capture into  $5f$  for  $O^{7+}+H$ ; MOCC, AOCC, CTMC results.

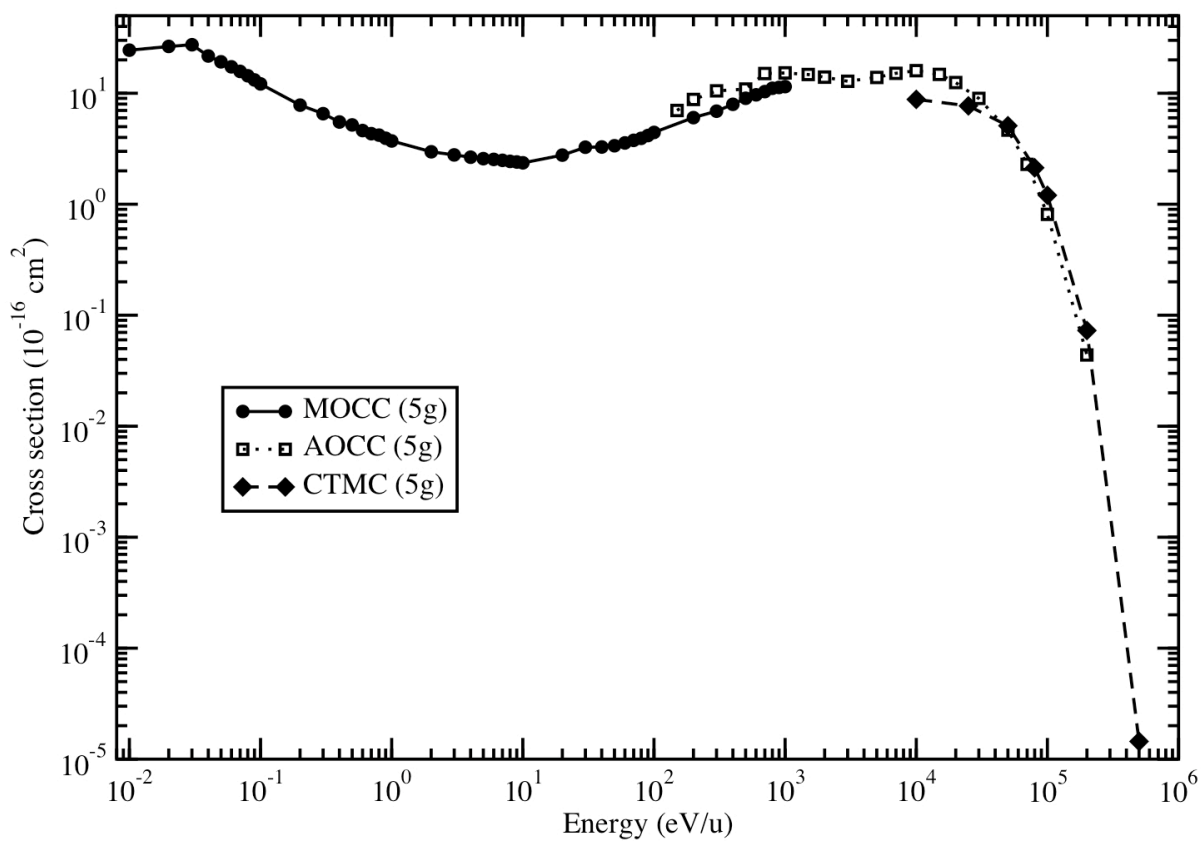


Figure A.9: Cross sections for capture into  $5g$  for  $\text{O}^{7+} + \text{H}$ ; MOCC, AOCC, CTMC results.

## APPENDIX B

### $n, l$ -RESOLVED CROSS SECTIONS FOR $C^{5+}+H$

In this appendix, we show  $n, l$ -resolved cross sections for  $C^{5+}+H$  using MOCC, AOCC, and CTMC results, for principal quantum numbers  $n = 3, 4$  and  $5$ . In future work, recommended fits for cross sections between  $10^{-2}$  and  $5 \times 10^5$  eV/u will be produced from these results.

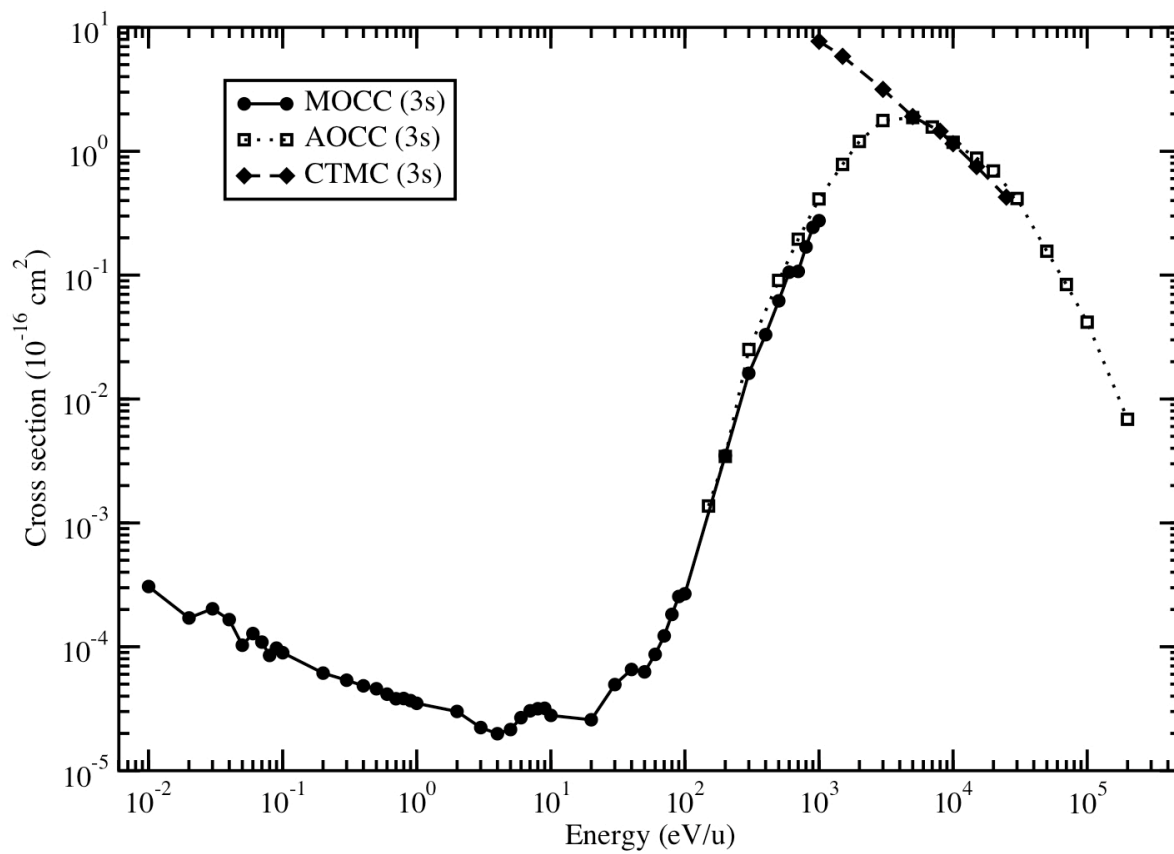


Figure B.1: Cross sections for capture into 3s for C<sup>5+</sup>+H; MOCC, AOCC, CTMC results.

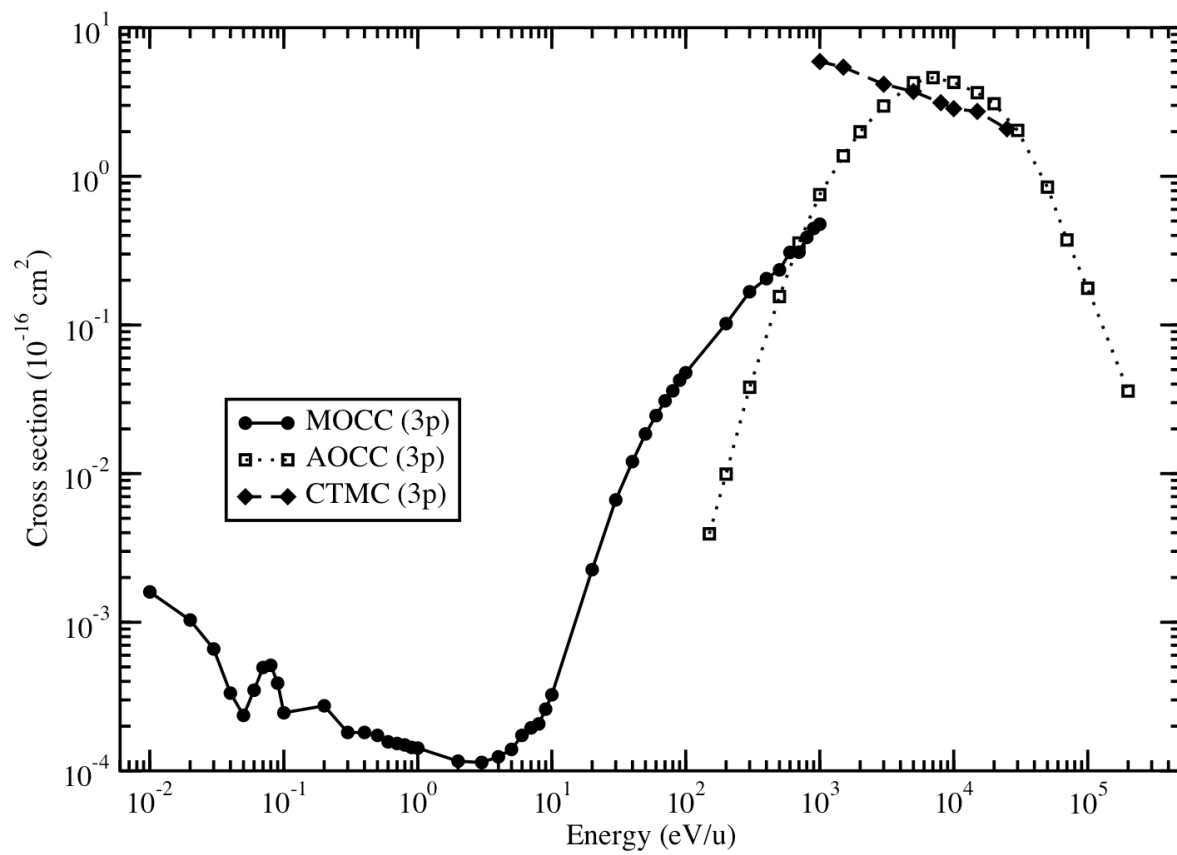


Figure B.2: Cross sections for capture into 3p for C<sup>5+</sup>+H; MOCC, AOCC, CTMC results.

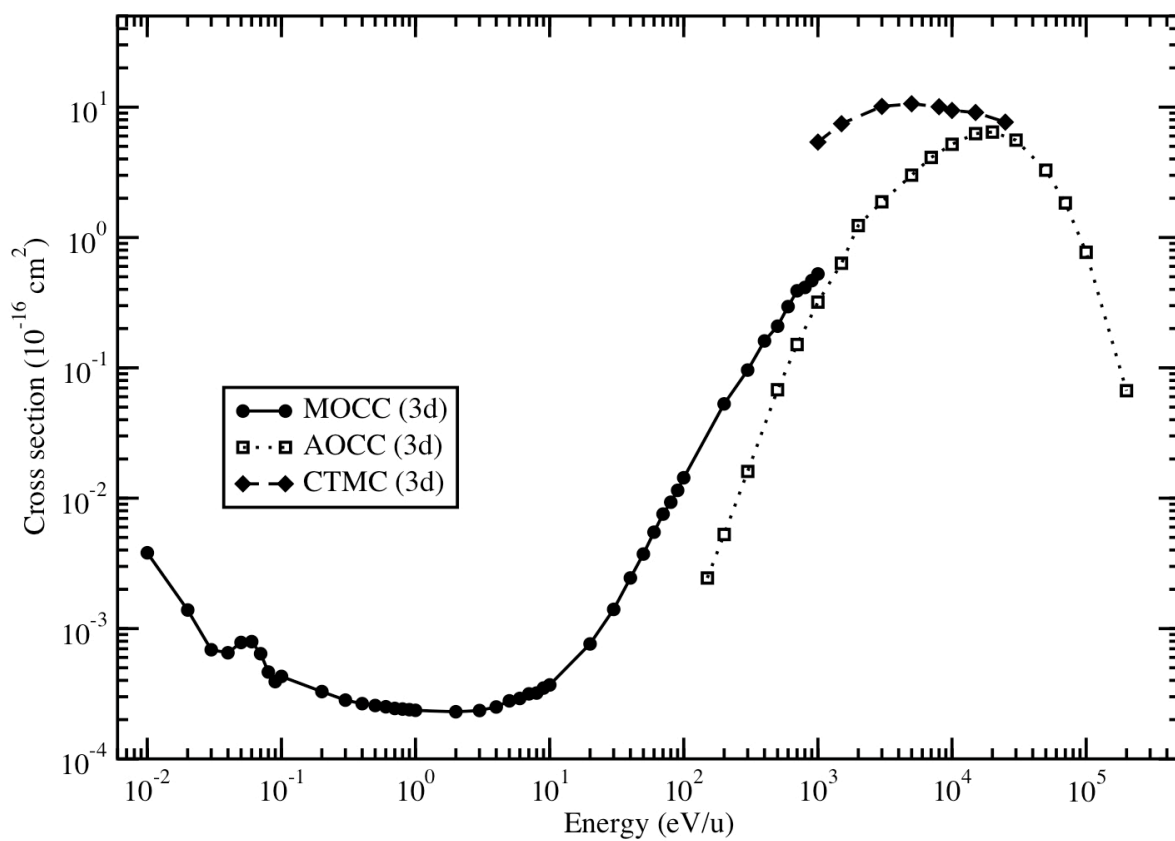


Figure B.3: Cross sections for capture into 3d for C<sup>5+</sup>+H; MOCC, AOCC, CTMC results.

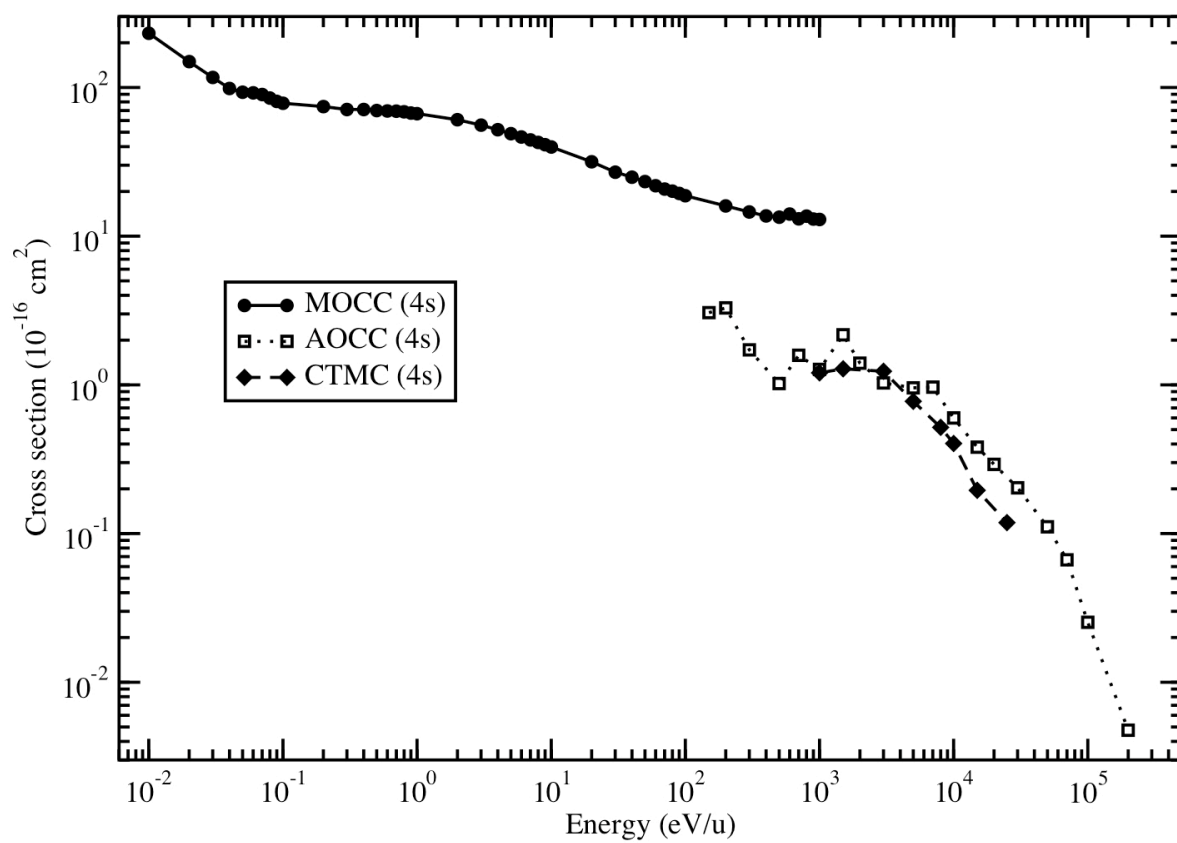


Figure B.4: Cross sections for capture into 4s for  $C^{5+} + H$ ; MOCC, AOCC, CTMC results.

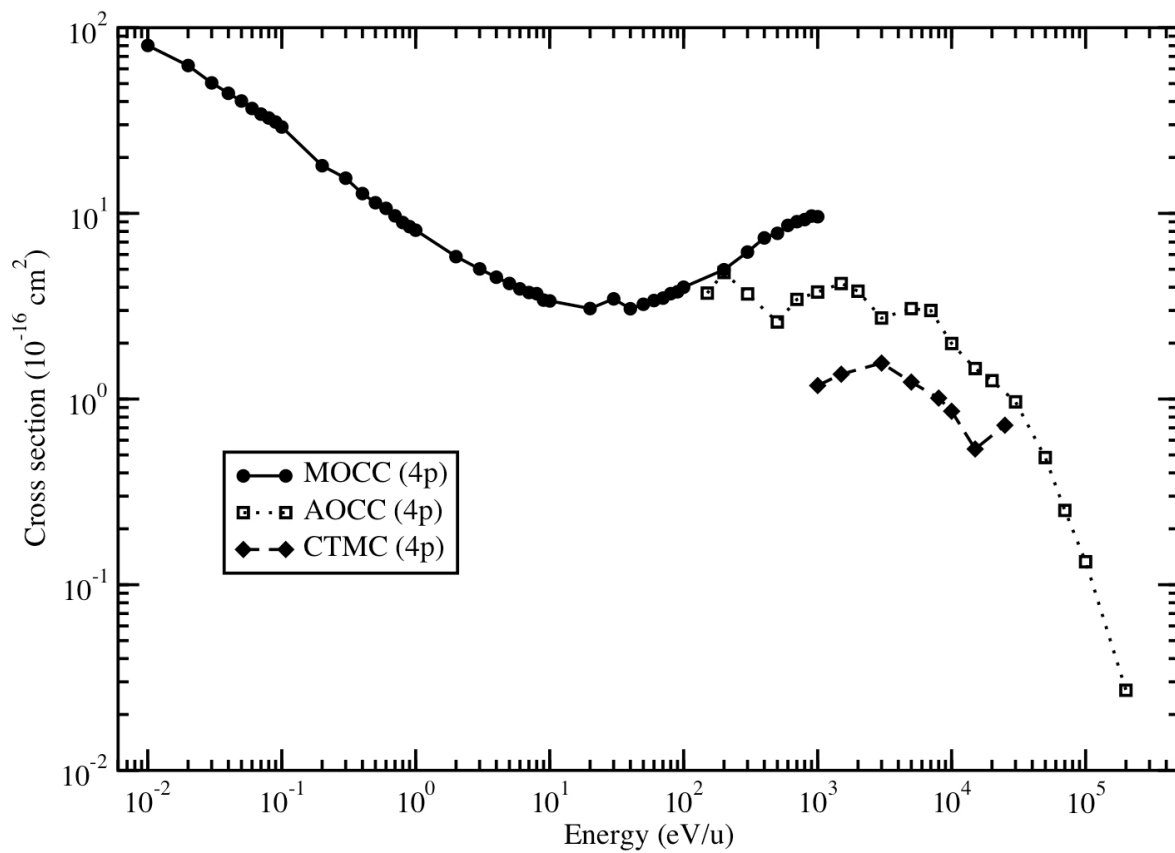


Figure B.5: Cross sections for capture into 4p for C<sup>5+</sup>+H; MOCC, AOCC, CTMC results.

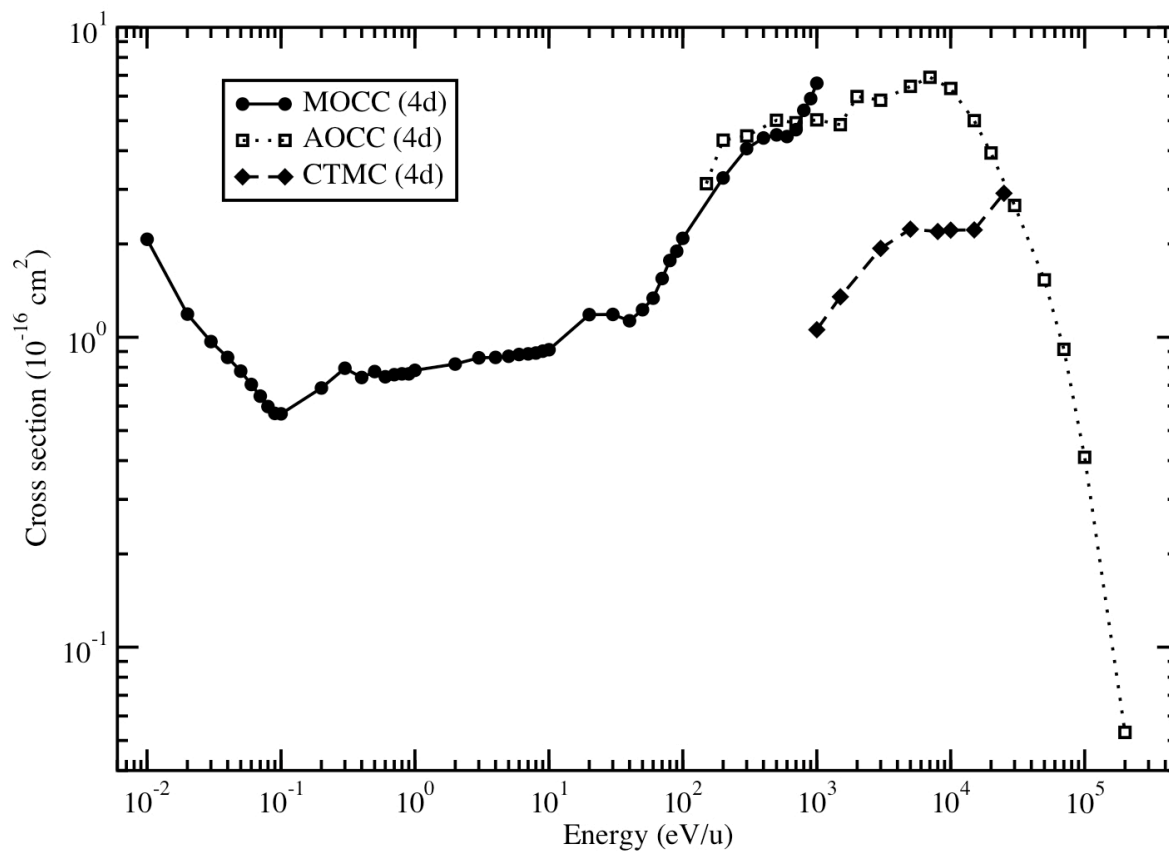


Figure B.6: Cross sections for capture into 4d for C<sup>5+</sup>+H; MOCC, AOCC, CTMC results.

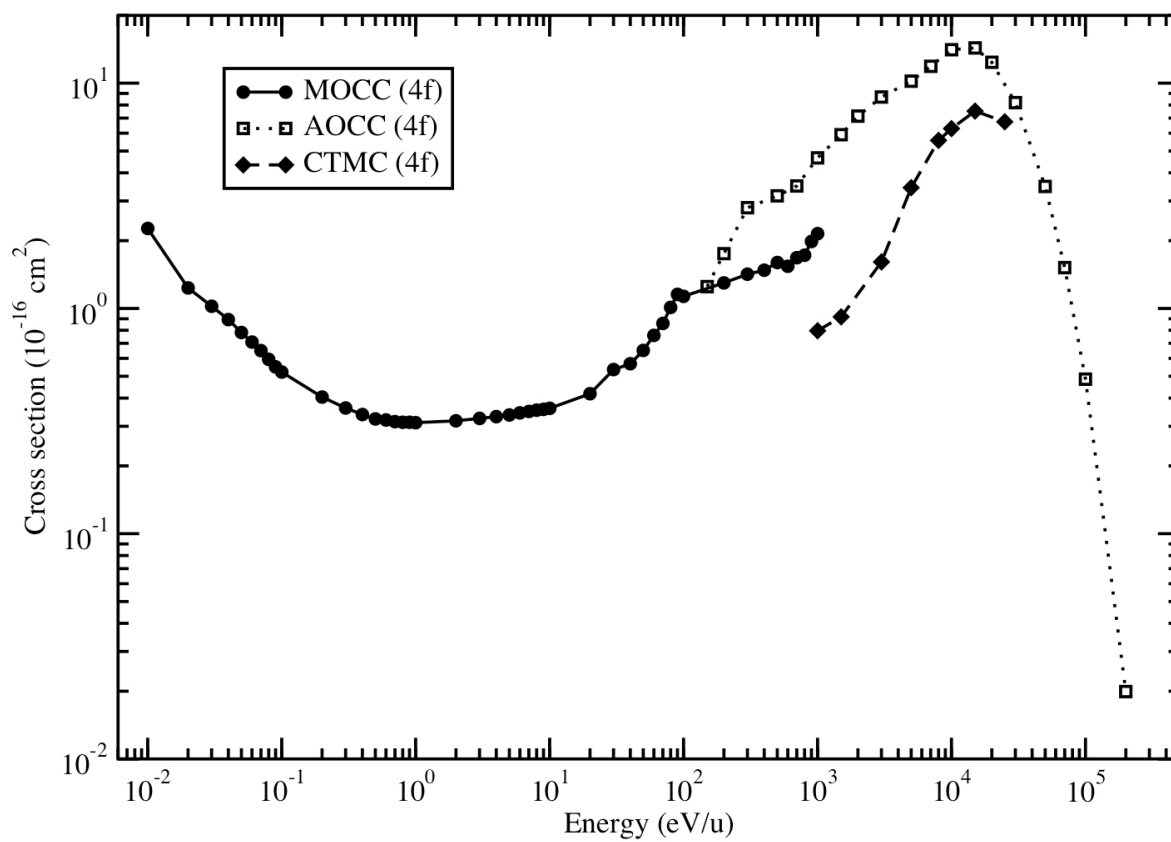


Figure B.7: Cross sections for capture into 4f for C<sup>5+</sup>+H; MOCC, AOCC, CTMC results.

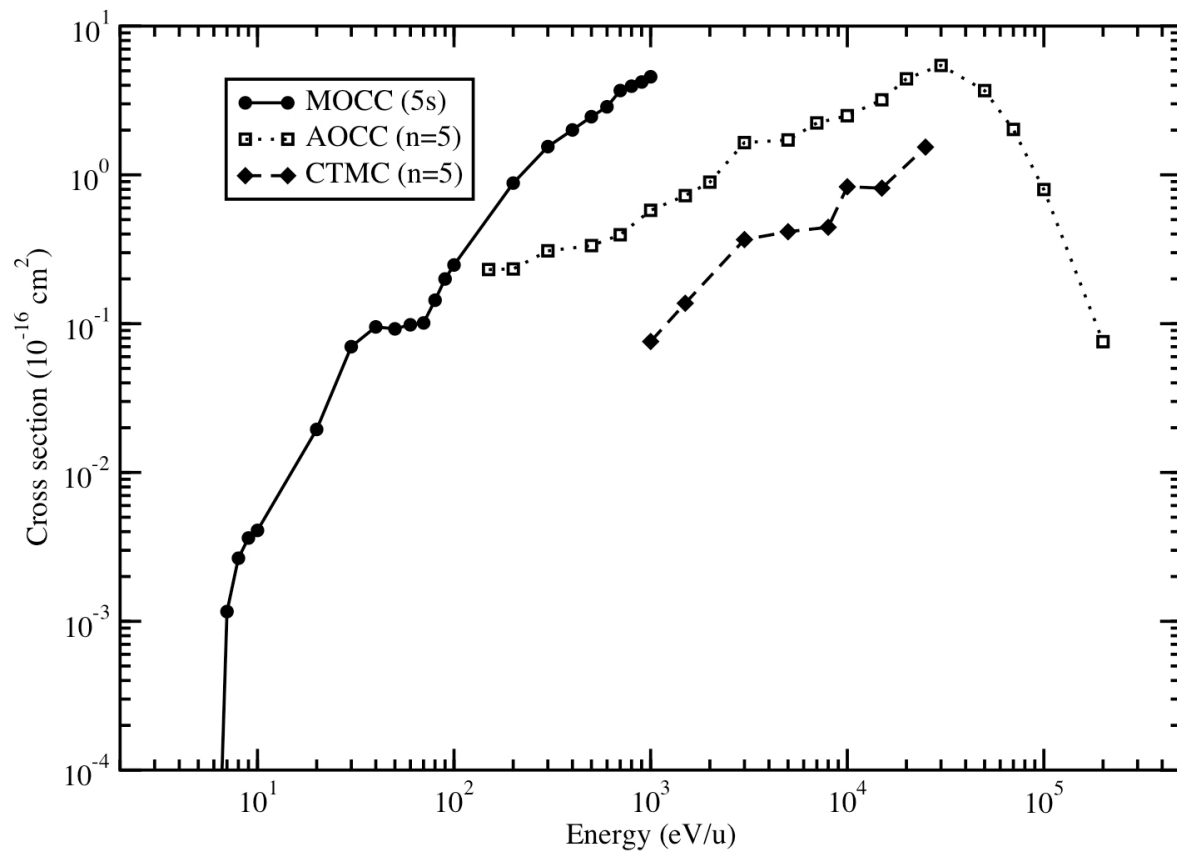


Figure B.8: Cross sections for capture into  $n = 5$  for  $C^{5+} + H$ ; MOCC (5s only), AOCC, CTMC results.